**Title**
Advanced Learning, Estimation and Control in High-Precision Systems



**Author**
Zheng, Minghui

**Publication Date**
2017

Peer reviewed|Thesis/dissertation

**Advanced Learning, Estimation and Control in High-Precision Systems**

by

Minghui Zheng

A dissertation submitted in partial satisfaction of the
requirements for the degree of
Doctor of Philosophy

in

Engineering - Mechanical Engineering

in the

Graduate Division

of the

University of California, Berkeley

Committee in charge:

Professor Masayoshi Tomizuka, Chair
Professor Kameshwar Poolla
Professor Laurent El Ghaoui

Spring 2017

**Advanced Learning, Estimation and Control in High-Precision Systems**

## Abstract

Advanced Learning, Estimation and Control in High-Precision Systems

by

Minghui Zheng

Doctor of Philosophy in Engineering - Mechanical Engineering

University of California, Berkeley

Professor Masayoshi Tomizuka, Chair

Systems with fast self-learning ability, high precision, and effective vibration attenuation play key roles in many areas including advanced manufacturing, data-storage systems, micro-electronic systems, and medical robotics. This dissertation focuses on three topics to achieve greater autonomy and accuracy in high-precision systems: (1) iterative learning control (ILC), (2) vibration estimation and (3) vibration control.

ILC is an effective technique that improves the tracking performance of systems that operate repetitively by updating the feedforward control signal iteratively from one trail to the next. The key in the design of ILC is the selection of learning filters with guaranteed convergence and robustness, which usually involves lots of tuning effort especially in high-order ILC. To facilitate this procedure, this dissertation presents a systematic approach to design learning filters for arbitrary-order ILC with guaranteed convergence, robustness and ease of tuning. The filter design problem is transformed into an H-infinity optimal control problem for a constructed feedback system. The proposed algorithm is further advanced to the one that explicitly considers system variations based on $\mu$ synthesis. High-order ILC enables the system to improve the performance through learning from more memory data with higher efficiency and guaranteed robustness. The proposed ILC design method is applied to a laboratory testbed of the Nikon wafer scanning system, and holds the potential for other applications such as intelligent manufacturing and rehabilitation systems that need considerable iterations of learning.

High-precision systems are usually subjected to high-frequency vibrations. Vibration estimation and suppression play key roles in high-precision systems. This dissertation explores two techniques of vibration estimation: disturbance observer (DOB) and extended state observer (ESO). A generalized DOB design procedure is proposed for a multi-input-multi-output (MIMO) system based on H-infinity synthesis. The proposed technique releases the DOB design from the plant inverse, assures the stability and minimizes the weighted H-infinity norm of the dynamics from the disturbance to its estimation error. A phase compensator is proposed for the ESO to push its estimation bandwidth from low frequency to

high frequency; the ESO's bandwidth is further pushed beyond the Nyquist frequency by including the nominal model of the disturbance dynamics.

Based on the frequency-domain characteristics of the vibrations which can be obtained either from vibration sensors or vibration estimators, this dissertation presents a systematic frequency-domain design methodology for sliding mode control (SMC) to effectively suppress vibrations as well as keep excellent transient performance. Specifically, a frequency-shaped sliding mode control is proposed by introducing the loop-shaping technique into the design of the sliding surface. The sliding surface is optimized based on H-infinity synthesis with guaranteed stability and desired frequency characteristics. This work extends SMC's applications to high-precision control systems which have demanding requirements in both time and frequency domains, and hold the potential to break some limitations of linear controls. The proposed vibration estimation and suppression techniques are applied to high-precision high-speed data storage systems, and significantly enhance vibration attenuation while maintaining excellent transient performance.

To my family

# Contents

# List of Figures

# List of Tables

# List of Abbreviations

| | |
|---|---|
| **AFSSMC** | Adaptive frequency-shaped sliding mode control |
| **DOB** | Disturbance observer |
| **DISO** | Dual-input-single-output |
| **ESO** | Extended state observer |
| **FIR** | Finite impulse response |
| **FSSMC** | Frequency-shaped sliding mode control |
| **HDD** | Hard disk drive |
| **IIR** | Infinite impulse response |
| **ILC** | Iterative learning control |
| **LFT** | Linear fractional transformation |
| **LMI** | Linear matrix inequality |
| **LQR** | Linear quadratic regulator |
| **LTI** | Linear time-invariant |
| **MIMO** | Multi-input-multi-output |
| **MSE** | Mean square error |
| **PES** | Position error signal |
| **PFMP** | Peak filter with multi-peaks |
| **PFSP** | Peak filter with single peak |
| **PZT** | Piezoelectric actuator made from Pb[Zr(x)Ti(1-x)]O3 |
| **SISO** | Single-input-single-output |
| **SMC** | Sliding mode control |
| **VCM** | Voice coil motor |

# Acknowledgments

First I would like to express my greatest gratitude to my supervisor and the chair of my dissertation committee Prof. Masayoshi Tomizuka. It is him who introduced me into the area of high-precision motion control, and guided me during my doctoral training including projects, papers, presentations and proposals. He is attentive and supportive along my Ph.D. journey. His profound knowledge, helpful suggestions, stimulating discussions and insightful vision have been fundamental in my academic development and growth as an independent researcher. More importantly, he led me a way of thinking, solving problems, summarizing and rethinking, which comes along my whole Ph.D. life and which is invaluable for my future academia life. I consider myself extremely fortunate to have been his student.

My grateful thanks are extended to Prof. Kameshwar Poolla for sitting on my dissertation committee, and Prof. Laurent El Ghaoui for sitting on my dissertation committee as well as my qualifying exam committee. I appreciate their insightful and invaluable discussions and suggestions along this journey. I would like to thank the late Prof. Karl Hedrick, who served the committee chair of my qualifying exam. He guided me with his professional knowledge and experience. His class on nonlinear control and his insights on sliding mode control motivated my doctoral research on nonlinear vibration suppression. I would also like to thank Prof. Robert Horowitz and Prof. Cari Kaufman for their participation in my qualifying exam and the suggestions they gave me for both my course work and doctoral research. I am thankful to Prof. Andrew Packard for the valuable knowledge and expertise I gained from his class on multivariable control systems. I feel fortunate that I have been the graduate student instructor for the class on feedback systems and control by Prof. Kameshwar Poolla, and the class on multivariable control systems by Prof. Andrew Packard. Their passion for instructions and teaching philosophy significantly impressed me and influenced my career. I am thankful to all my professors at UC Berkeley for their helpful suggestions and informative classes, from which I learned a lot, found interesting ideas for my research, and established the cornerstone of my knowledge.

I would like to thank Western Digital's support for my doctoral research on hard disk drives, and thank the people I have worked with. I would like to thank Guoxiao Guo, who is regarded as my 'external advisor' from the industry and provided me invaluable suggestions. I would also like to thank Edward Tu, my manager during my intern at Western Digital. Furthermore, I would like to thank Jie Yu, Wei Xi, Jianguo Zhou, Jake Kim, Min Chen, Li Yi, Shang-Chen Wu, Haiming Wang, and Yuanyuan Zhao. All of them gave me lots of advices and help on industrial projects.

I feel so fortunate that I am one of the Mechanical Systems Control (MSC) lab members. I would like to thank Dr. Xu Chen, Shiying Zhou, Liting Sun, for the discussions on hard disk drive and high-precision motion controls. I would like to thank Dr. Wenjie Chen, Dr. Cong Wang, and Dr. Wenlong Zhang for their help and suggestions for my PhD study and academia careers. I would like to thank Dr. Junkai Lu, Dr. Chung-yen Lin, and Chen-yu Chan, for sharing all the times in the preliminary exams, qualifying exams and other tough and challenging times during my study life at Berkeley. I would like to thank other

members of MSC lab: Dr. Yizhou Wang, Dr. Chi-Shen Tsai, Dr. Kan Kanjanapas, Dr. Mike Chan, Dr. Raechel Tan, Dr. Kevin Haninger, Xiaoyu Wen, Yu Zhao, Changliu Liu, Te Chang, Hsien-Chung Lin, Shuyang Li, Yongxiang Fan, Wei Zhan, Cheng Peng, Zining Wang, Daisuke Kaneishi, Yu-Chu Huang, Jiachen Li, Kiwoo Shin, Chen Tang, Zhuo Xu, Jianyu Chen, Yujiao Cheng, and Yeping Hu. I would also like to thank all my friends I met at Berkeley who made my life more meaningful and colorful.

Last but not least, I wish to express my utmost gratitude and deepest love to my parents, my sister, and my husband, Xiao Liang, for their unconditional love and support.

# Chapter 1

# Introduction

## 1.1 High-Precision Systems

High-precision systems play essential roles in current industries including manufacturing and information storage. This dissertation focuses on two kinds of high-precision systems: hard disk drives (HDDs) and wafer scanners.

### Hard Disk Drive

Data cloud and mobile media are opening a new market for data storage systems. HDD is one of the major data storage systems nowadays because of its high capacity and low cost. Figure 1.1 illustrates a single-stage HDD system including a platter, a spindle, a voice coil motor (VCM), an actuator arm, and a read/write motion head. There are many data tracks with high density on the platter. The head is driven by the VCM to read the data from the platter. HDD is a high-speed high-precision system that has demanding requirement for both the accuracy and robustness of the servo controller for the recording head. Figure 1.2 shows a famous analogy among the disk and other systems such as the human hair, dust particles and smoke particles to help understand the precision level of the disk space.

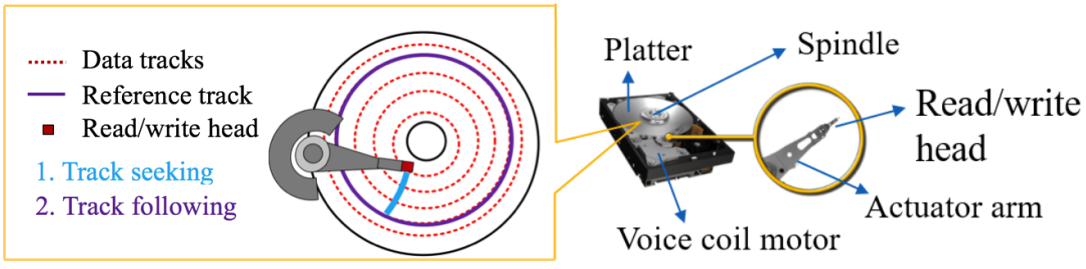


Figure 1.1: Illustration of hard disk drives

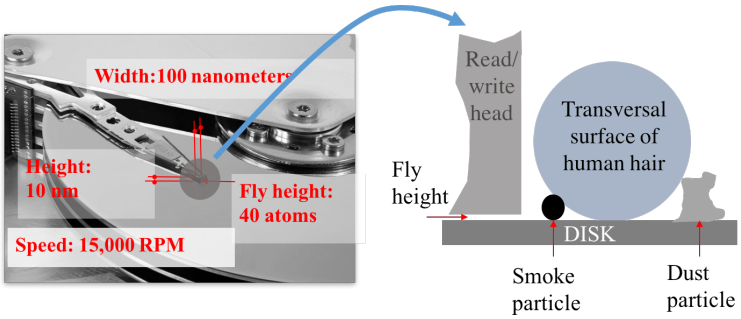


Figure 1.2: Hard disk space

A full-order HDD plant can be described by the following transfer function

$$P(p) = \frac{k_y k_v}{p^2} + \sum_{i=1}^{4} \left( \frac{{\omega_i}^2}{p^2 + 2\xi\omega_i p + {\omega_i}^2} \right) \tag{1.1}$$

where $p$ is the Laplace variable. It is known as the Benchmark model for the single-stage HDDs [1]. It is from the identification of an actual experimental HDD setup (rotation speed: 7200 rpm; number of servo sector: 220; sampling time: $T_s$=3.7879×$10^{-5}$ s; acceleration constant: $k_v$=951.2 m/(s$^2$A); position measurement gain: $k_y$=3.937×$10^6$ track/m). The four resonance frequencies $\omega_i$'s are 4100 Hz, 8200 Hz, 12300 Hz, and 16400 Hz; and the corresponding damping factor $\xi$ is 0.02. More details are provided in [1]. The bode plot of the HDD model is provided in Figure 1.3. High frequency resonances are usually attenuated by notch filters.

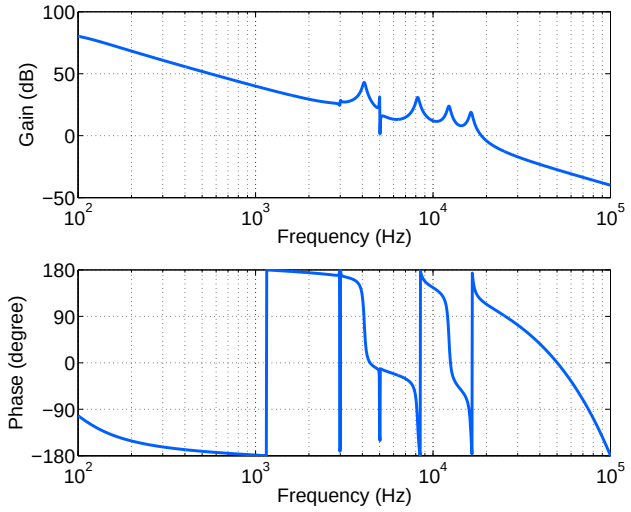


Figure 1.3: Full-order model of HDD [1]

There are two control tasks in HDDs: track seeking and track following, as shown in Figure 1.1. The track-seeking task is to make the head fast and smoothly switch from one data track to the target data track with small overshoot. The track-following task is to make the head precisely follow the target data track with good robustness to vibrations. During both the track-seeking and track-following processes, the head is subject to large external high-frequency disturbances. These disturbances may excite the resonances of HDDs and seriously affect the servo performance. Therefore, it is of fundamental importance to attenuate the influence of such high-frequency disturbances.

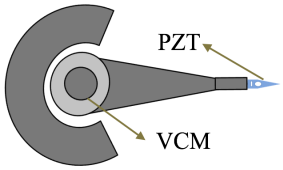


Figure 1.4: Dual-stage hard disk drives

To increase the servo bandwidth of HDDs and enhance vibration suppression, recently a piezoelectric actuator made from lead zirconate titanate (Pb[Zr(x)Ti(1-x)]O3, or PZT) has been added to the end of the VCM stage in dual-stage HDDs, as shown in Figure 1.4. With the PZT actuator, the HDD plant becomes a dual-input-single-output (DISO) system. Furthermore, the PZT actuator has a limited stroke and can be easily saturated in presence of large vibrations. Therefore, although such an additional actuator allows higher precision and accuracy of HDDs, it brings more challenging and interesting control topics as well. These topics include the identification of varying resonances without disabling the PZT loop [2], the optimal allocation of the vibration compensation between the VCM and PZT loops [3, 4], and the anti-windup schemes to reduce the saturation in the PZT loop [5–7].

## Wafer Scanner

Wafter scanner plays a key role in high-precision semiconductor manufacturing. It is for the photography that copying the circuit pattern from a mask to a wafer. The position accuracy can be less than 1 nm. Figure 1.5 shows a laboratory testbed for the wafter scanner in the Mechanical Systems and Control (MSC) laboratory, University of California, Berkeley. The main components include the reticle stage, the wafter stage, the counter mass, and the laser interferometer. The positions of the stages are measured by the laster interferometers. The controller is realized by a LabVIEW real-time system with field programmable gate array (FPGA) with a sampling frequency of 2500 Hz. More detailed descriptions of the testbed can be found in [8]. Figure 1.6 shows one standard scanning trajectory which is repetitive over iterations.

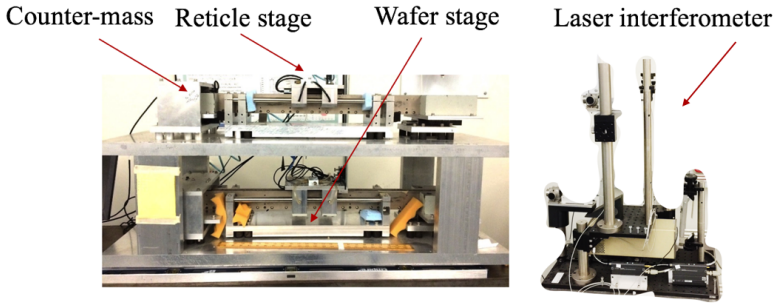


Figure 1.5: Laboratory testbed for wafer scanning systems

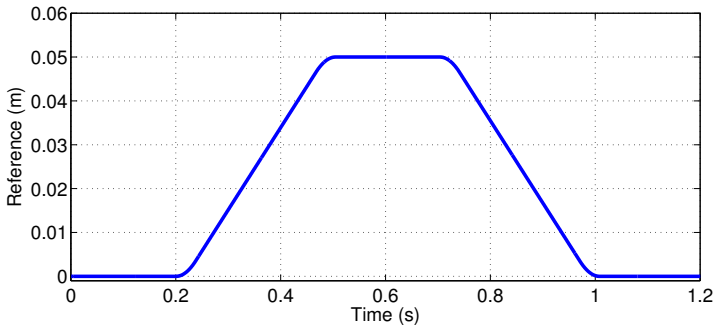


Figure 1.6: One scanning trajectory

## 1.2 Motivation and Contributions

### Iterative Learning Control

Many high-precision mechanical systems in manufacturing operate repetitively. The repetitive nature motivates a powerful learning algorithm: iterative learning control (ILC). It updates the feed-forward control signal iteratively based on the memory data from previous iterations, aiming to suppress repetitive disturbances and improve the tracking performance of the systems.

ILC has been applied to a variety of industrial systems including manipulators [9–12], positioning stages [13, 14], HDDs [15, 16] and wafer scanning systems [8, 17, 18]. Reference [19] provided detailed ILC analysis with applications to various industrial areas. The key and main challenge in ILC lies in the design of learning filters with guaranteed convergence and robustness, which usually involves lots of tuning especially in the design of high-order ILC that utilizes more memory data.

To facilitate the design procedure, this dissertation presents a systematic framework to synthesize arbitrary-order ILC with guaranteed convergence and ease of tuning. The learning filter (matrix) design problem in ILC is transformed into an H-infinity optimal control problem for a constructed feedback system. This methodology is proposed directly

in iteration-frequency domain based on the infinite impulse response (IIR) systems instead of the finite impulse response (FIR) systems to incorporate more general dynamic systems into learning filters and gain more efficient computation. Detailed design procedure and convergence analysis are provided. This framework is further improved through $\mu$ synthesis to explicitly incorporate system variations. The proposed framework has produced promising results in the design of ILC with arbitrary order and is readily to be extended to multi-input-multi-output (MIMO) systems.

## Vibration Estimation

High-precision systems including HDDs and wafer scanners are very sensitive to vibrations. These vibrations usually have large peaks and may significantly degrade the precision and accuracy. Therefore, it is of fundamental importance to attenuate the influence of such vibrations in high-precision systems. Various approaches have been proposed for vibration estimation and suppression in the existing literature. These approaches can be categorized into two groups: feedforward approach and feedback approach. The former one is generally dependent on known disturbance dynamics or measurements by sensors [20–22]. The later one generally combines observers and control algorithms [23–25] to estimate, compensate and suppress disturbances. Some reviews on these algorithms are provided in [26–28]. This dissertation explores two feedback approaches to estimate vibrations without vibration sensors: disturbance observer (DOB) and extended state observer (ESO).

### (a) Disturbance observer

DOB is a powerful technique to estimate and compensate disturbances in high-precision systems. It is a plant-inverse based technique and has many industrial applications such as HDDs [29, 30], power-assist electric bicycles [31], wafer scanning systems [32], manipulators [33], and autonomous vehicles [34]. The general DOB design procedure includes two steps: (a) design a stable inverse of the plant; and (b) design a Q-filter to maintain the causality and robustness. However, designing a stable inverse of the plant is usually difficult for MIMO and non-minimum phase systems. It is rather challenging to design a suitable plant inverse and apply DOB technique to the systems with the inputs of higher dimension than the outputs.

To unnecessitate plant inverse, this dissertation presents a DOB design procedure for a general MIMO system. The proposed DOB minimizes the weighted H-infinity norm of the dynamics from the disturbances to its estimation error, and assures the stability. This DOB design procedure is applicable not only to the square systems, but also to the systems with the inputs of higher dimension than the outputs. Furthermore, being relaxed from the restrictions of the conventional DOB structure, the proposed approach has more design flexibilities and is promising to achieve better performance than the conventional DOB. It is also worth mentioning that the proposed DOB is still an add-on algorithm aiming to estimate and compensate the disturbances without redesigning the baseline feedback

controller. Detailed evaluation has been performed on a dual-stage HDD plant that has dual inputs and single output.

**(b) Extended state observer**

ESO is an alternative promising method to estimate the disturbances by treating them as state variables. ESO was proposed in [35], generalized and implemented in discrete time in [36]. The effectiveness of ESO for a large class of disturbances was demonstrated by simulations and experiments [37–40]. ESO has several advantageous properties. It can be incorporated into linear and nonlinear systems. It does not require an accurate plant model or its inverse. ESO can estimate a large class of disturbances without changing the observer's structure and parameters. Because of such properties, ESO has been combined with both linear and nonlinear controllers and applied to various systems [41–43]. The existing ESO works well for slowly time-varying or low-frequency disturbances; however, such good performance is not inherited to fast time-varying or high-frequency vibrations. The challenge that limits its performance bandwidth comes into two: (1) phase loss caused by both the plant and the ESO itself; (2) sensor's sampling frequency.

This dissertation presents two approaches to extend ESO's performance range from low frequencies to high frequencies, and even beyond the Nyquist frequency when the vibration dynamics is available. Firstly, a phase compensator is proposed to recover the phase loss in standard ESO within certain frequency range; such compensated ESO provides accurate estimates for both the states and the vibrations; secondly, a multi-rate observer is proposed to incorporate the nominal dynamics of the vibrations and is able to estimate both the state and the vibrations beyond the Nyquist frequency.

## Nonlinear Vibration Control

In HDDs and other modern high-precision motion control systems, high-frequency vibration suppression is always a challenging topic. It becomes even worse when there exist multiple large peaks in the vibration spectrum. Besides the estimation of vibrations and system behaviors, feedback control algorithms have to be designed properly for vibration suppression. Traditional linear control algorithms, such as loop shaping, linear quadratic regulator (LQR), and $H_2/H_\infty$ robust control, still dominate high-precision systems because of the comprehensive and intuitive design methodology in frequency domain. Loop-shaping technique aims to design certain filter which is shaped to mitigate the performance degradation at specific frequencies [44]. The LQR algorithm minimizes certain weighted cost function which includes the terms of the tracking error and the control effort [45, 46]. The H-infinity algorithm minimizes the effect of the vibrations to the tracking error, and has good robustness to external vibrations [47, 48].

One limitation of linear time-invariant (LTI) feedback control is the 'waterbed' effect as described in [49]. Another problem of linear control in HDDs is the switch of control algorithms between track seeking and track following. To unify different tasks into one

control scheme and reduce the 'waterbed' effect, nonlinear control has become popular in HDD industry [50]. Specifically, sliding mode control (SMC) has been modified and applied to HDD systems for its fast convergence and robustness to external disturbances [51–54]. Most of the existing literature utilizes SMC to improve the transient performance when the track seeking is switched to the track following. These SMC algorithms are designed and analyzed in time domain without considering the frequency-response characteristics of the closed-loop systems, which are critically important for high-precision systems that are subject to high-frequency vibrations. Therefore, it makes significant sense to explicitly consider frequency-domain performances of the closed-loop systems when designing SMC, which is rather challenging due to the nonlinearity of SMC.

The gap between the nonlinear systems and frequency analysis limits the application of intuitive frequency-shaping techniques into SMC, which motivates several new prospectives to the research on SMC. This dissertation presents two frequency-shaped SMCs utilizing either the root locus technique or the H-infinity synthesis in robust control theory. The former one is effective and easy to implement especially when there is only one peak in the vibration spectrum; the latter one is a more comprehensive framework to design the sliding surface in frequency domain. The shaping filter is considered as an inner loop feedback controller, and the dynamics of the sliding surface is augmented into a feedback system. With this idea, the sliding surface design problem is formulated as a convex H-infinity optimization problem with linear matrix inequality (LMI) constraints, and the stability of the sliding surface can be guaranteed in the presence of disturbances. The resulting shaping filter minimizes the weighted H-infinity norm of the sliding dynamics and thus minimizes performance degradation at the frequencies where the servo performance is seriously degraded by large disturbances.

The proposed H-infinity based frequency-shaped SMC reveals different insights into SMC, guarantees both the stability and the desired frequency characteristics of the sliding surface dynamics in the presence of vibrations, and provides frequency-dependent control allocation. Furthermore, an explicit sub-optimal filter is obtained to avoid on-line optimization when the vibrations' frequency characteristics change over time or among different disturbance sources. Both the SMC algorithms and the shaping filters are designed in discrete time, and thus can be readily implemented on actual mechanical systems. This theoretical methodology has been evaluated on HDDs, and is potentially applicable to other advanced mechanical systems such as industrial manipulators whose performance is extensively limited by strong nonlinearities and vibrations introduced by flexibility.

## 1.3 Dissertation Organization

The remainder of the dissertation is organized as shown in Figure 1.7. Chapter 2 presents a systematic framework to design arbitrary-order ILC in frequency domain; it is a feedforward control technique to improve the tracking performance over iterations when the reference is repetitive. Chapters 3 and 4 present vibration estimation techniques. Chapter 3 presents

a generalized design procedure for DOB which estimates the disturbances of the system without the explicit inverse of the plant. Chapter 4 presents two techniques to increase the estimation bandwidth of ESO for both the state and the disturbance estimation. Chapters 5 and 6 present frequency-shaped SMC algorithms based on the root locus technique and the H-infinity synthesis, respectively. The former one is easy to implement, and the stability can be easily guaranteed when the vibrations have single peak frequency; the latter one is a systematic framework to design the optimal shaping filter with guaranteed stability when the vibrations have one or more peak frequencies. Chapter 7 presents the proposed frequency-shaped SMC based on the estimators for both the states and the vibrations. Chapter 8 concludes this dissertation and discusses some future topics.

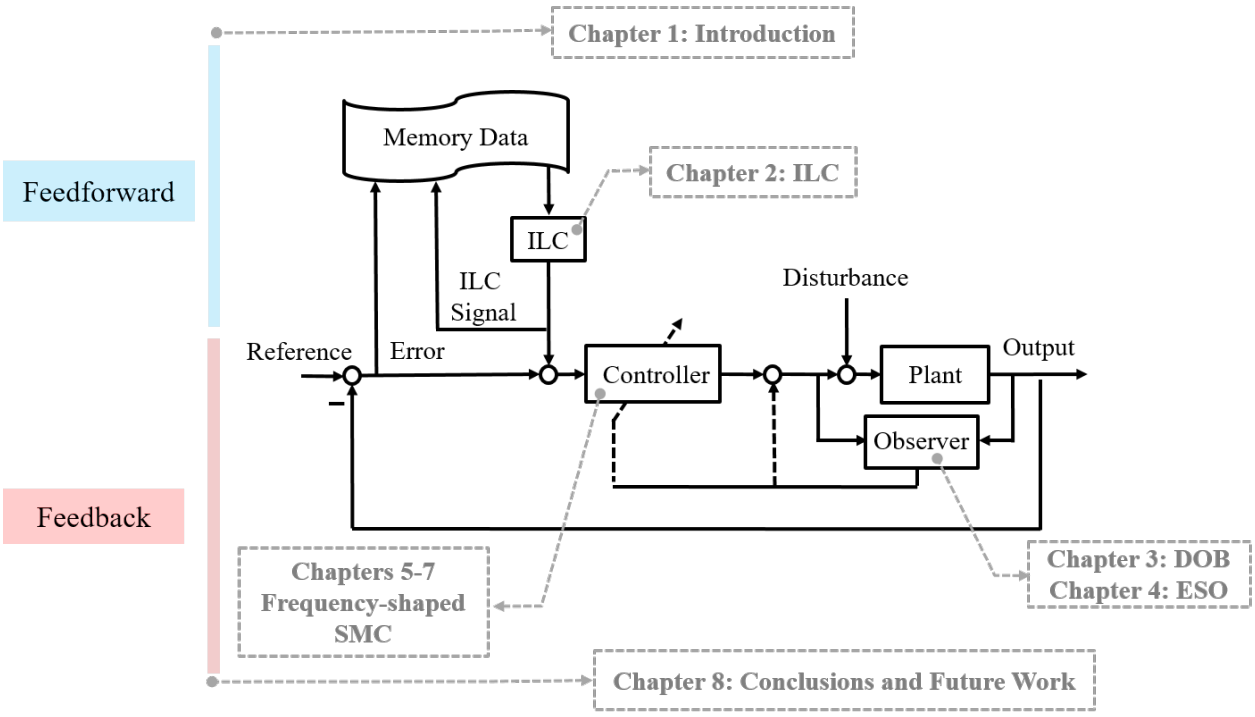


Figure 1.7: Dissertation organization

# Chapter 2

# Iterative Learning Control

## 2.1 Introduction

Iterative learning control (ILC) is an effective technique to suppress repetitive disturbances and improve the tracking performance of systems that operate in a repetitive manner. It tunes the feedforward control signal iteratively from one trail to the next. ILC has been applied to a variety of industrial problems. One main challenge in ILC is to design learning filters to guarantee both the tracking error convergence and the robustness to system variations. A common design approach is based on the pseudo-inverse of the plant dynamics, which may be hard to obtain, or introduce a sensitivity problem to unmodeled dynamics [55]. An alternative approach with little tuning effort was proposed based on the $H_\infty$ optimal control theory [56, 57]. This method was further improved by $\mu$-synthesis technique to explicitly take system variations into account with acceptable compromise of the convergence rate [58–61]. Comprehensive reviews of the basic formulations of ILC, its variations and the frequency-domain design approaches are provided in [62–65].

Most research efforts for the $H_\infty/\mu$-based approach have focused on the first-order ILC. Recently the high-order ILC that utilizes more data from previous iterations has gained increasing attention. Compared to the first-order ILC, the high-order ILC has more flexibilities when designing learning filters and is promising to achieve better performance such as faster tracking or additional robustness to some non-repetitive disturbances [66–70]. Despite such favorable performances, designing multiple learning filters is a difficult task with even more tuning efforts in the high-order ILC. To reduce such efforts, similar to the first-order ILC case, $H_\infty$ synthesis was utilized to design learning filters in the high-order ILC [71, 72], in which the algorithms were proposed in the super-vector framework based on a finite impulse response (FIR) system and the lifting technique. However, the frequency-domain design approach for high-order ILC has not been fully investigated in the existing literature.

This chapter develops a systematic frequency-domain design framework for high-order ILC based on the $H_\infty/\mu$ synthesis to fill in the knowledge gap [73]. Because the algorithm is designed in frequency domain, and every iteration is assumed to have infinite horizon, the

systems in this chapter are represented by infinite impulse response (IIR) filters, which have been extensively studied in control theory and are easier for implementation. Specifically, a systematic approach of designing an arbitrary-order ILC algorithm is proposed in the iteration-frequency domain based on an IIR system. The learning filters are generated off-line through designing an $H_\infty$ optimal controller for a constructed feedback system. A $\mu$-synthesis based ILC is also developed to explicitly consider system variations. The effectiveness of the proposed ILC algorithms is demonstrated on a wafer scanning testbed through both simulations and experiments. The main contribution of the work presented in this chapter lies in the novel frequency-design approach with systematic inclusion of both first-order and high-order ILC.

## 2.2 Standard ILC

Consider a general discrete-time linear time invariant (LTI) system

$$y = P(u + d) \tag{2.1}$$

where $y$ is the output, $u$ is the control signal, $d$ is the disturbance, and $P$ is the plant. $P$ can be described either by an FIR model:

$$P = h_0 + h_1 z^{-1} + h_2 z^{-2} + \cdots \tag{2.2}$$

or by an IIR model:

$$P = \frac{b_1 z^{-1} + b_2 z^{-2} + ... + b_n z^{-n}}{1 + a_1 z^{-1} + a_2 z^{-2} + ... + a_n z^{-n}} \tag{2.3}$$

where $z$ is the discrete frequency domain operator. As mentioned in the introduction, generally ILC is designed based on the FIR model (2.2); alternatively, this chapter designs ILC based on the IIR model (2.3) that may include feedback terms and is more efficient for practical implementation.

The structure of the ILC algorithm for the system in (2.1) is shown in Figure 2.1, where the reference $r$ is assumed to be repetitive over iterations. $e{=}r{-}y$ is the tracking error, and $u^f$ is the feedforward control signal that is refined by the ILC algorithm iteration by iteration. $C$ is a feedback controller. $u{=}C(u^f + e)$ is the total real-time control signal. Use $j$ to index the iterations. By assuming that the end time of each iteration is at infinity, the tracking error during the $j^{\text{th}}$ iteration is

$$e_j = T_u u_j^f + T_r r + T_d d_j \tag{2.4}$$

where $T_u$, $T_r$, and $T_d$ are the closed-loop transfer functions from $u_f$ to $e$, $r$ to $e$, and $d$ to $e$, respectively,

$$\begin{aligned} T_u &= -(1 + PC)^{-1} PC \\ T_r &= (1 + PC)^{-1} \\ T_d &= -(1 + PC)^{-1} P \end{aligned} \tag{2.5}$$

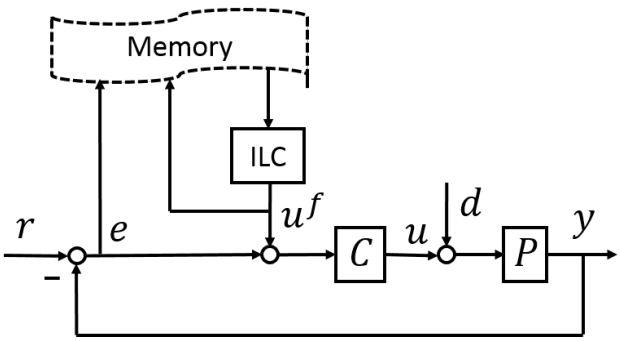


Figure 2.1: Control system with ILC.

A standard first-order ILC is designed as follows,

$$u_{j+1}^f = Q(u_j^f + Le_j) \tag{2.6}$$

where the filter $Q$ and the learning filter $L$ are to be designed. Substituting Equation (2.6) into Equation (2.4), we have

$$\begin{aligned} e_{j+1} &= T_u[Q(u_j^f + Le_j)] + T_d d_{j+1} + T_r r \\ &= Q(1 + T_u L)e_j + T_r(1 - Q)r \\ &\quad + T_d(d_{j+1} - Qd_i) \end{aligned} \tag{2.7}$$

Assuming that the disturbance $d$ is consistent through iterations, i.e., $d_{j+1} = d_j$, Equation (2.7) becomes

$$e_{j+1} = Q(1 + T_u L)e_j + T_r(1 - Q)r + T_d(1 - Q)d \tag{2.8}$$

A sufficient condition to guarantee the stability of Equation (2.8) with respect to $e_j$ is

$$\|Q(1 + T_u L)\|_\infty < 1 \tag{2.9}$$

To eliminate the tracking error, ideally $Q$=1, and Equation (2.8) becomes

$$e_{j+1} = (1 + T_u L)e_j \tag{2.10}$$

In this case, if $\|1+T_uL\|_\infty<1$, $e_{j+1}$ converges to zero monotonically over iterations. However, it is usually difficult to find a $L$ such that $|(1+T_uL)(jw)|<1$ is achieved over all frequencies. A major challenge comes from system uncertainties in $T_u$ which are usually large at high frequencies. Therefore, to obtain robustness against system uncertainties and variations, instead of setting $Q$=1, $Q$ is often designed as a low-pass filter. As a compromise, this introduces the effects of $T_r(1-Q)r$ and $T_d(1-Q)d$, as expressed in Equation (2.8). Nevertheless, the reference $r$ is usually a low-frequency signal, so that $T_r(1-Q)r$ is almost zero. The disturbance $d$, on the other hand, usually contains high-frequency components, which leads to a nontrivial $T_d(1-Q)d$.

In general, a trade-off exists when designing $Q$: the robustness to system variations requires a small gain of $Q$ at high frequencies, while the disturbance rejection desires a high bandwidth of $Q$. To address this trade-off effectively, we design ILC in two steps: (1) design $L$ through the minimization of $\|(1+T_uL)W\|_\infty$, where $W$ is the weighting filter to 'shape' the expected frequency response of $(1+T_uL)(jw)$; (2) design $Q$ to guarantee $\|Q(1+T_uL)\|_\infty<1$.

## 2.3 First-order ILC Based on H-infinity Synthesis

The learning filter (denoted as $L_\infty$ in this section) design problem can be formulated as an $H_\infty$ optimization problem:

$$\min_{L_\infty} \ \|(1+T_uL_\infty)W\|_\infty \tag{2.11}$$

where $W$ is a frequency-dependent weighting filter to provide additional design flexibilities and mitigate the trade-off in the design of $Q$ (described in the end of Section II). This section shows that the optimization problem (2.11) can be solved by transforming it into an $H_\infty$ optimal control problem. To do so, a fictitious feedback control system is constructed in Figure 2.2. Let $T_{zw}$ denote the closed-loop transfer function from $z$ to $w$, i.e., $T_{zw} \triangleq L_f(M, L_\infty)$, where $L_f(\cdot)$ is the lower linear fractional transformation (LFT) and $M$ is defined in Figure 2.2. The following is to show that $T_{zw}$ is exactly the transfer function whose $H_\infty$ norm is the one to be minimized, i.e.,

$$T_{zw} = (1+T_uL_\infty)W \tag{2.12}$$

From Figure 2.2,

$$\begin{aligned} \begin{bmatrix} w \\ g \end{bmatrix} &= M \begin{bmatrix} z \\ v \end{bmatrix} = \begin{bmatrix} W & T_u \\ W & 0 \end{bmatrix} \begin{bmatrix} z \\ v \end{bmatrix} \\ v &= L_\infty g \end{aligned} \tag{2.13}$$

Then

$$\begin{aligned} w &= Wz + T_uv = Wz + T_u(L_\infty g) \\ &= Wz + T_uL_\infty(Wz) = (1+T_uL_\infty)Wz \end{aligned} \tag{2.14}$$

Therefore, Equation (2.12) holds.

Assume $T_{zw}$ has the following state-space realization,

$$T_{zw} \backsim \begin{bmatrix} A_c & B_c \\ C_c & D_c \end{bmatrix} \tag{2.15}$$

The $H_\infty$ optimization problem (2.11) becomes designing a fictitious feedback 'controller' $L_\infty$ to minimize $\|T_{zw}\|_\infty$, i.e.,

$$\begin{aligned} \min_{L_\infty,\gamma} \quad & \gamma \\ & |\lambda_i(A_c)| < 1, \quad \forall i \\ & \|T_{zw}\|_\infty < \gamma \end{aligned} \tag{2.16}$$

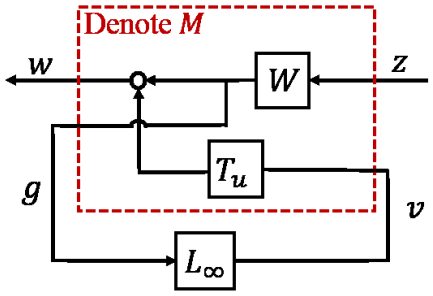


Figure 2.2: Constructed feedback system for first-order ILC

where $\lambda_i(A_c)$ is the $i^{\text{th}}$ eigenvalues of $A_c$.

A standard method of solving the optimization problem (2.16) is transforming it into a convex optimization problem with linear matrix inequality (LMI) constraints [74], which can be efficiently solved thereafter. Once $L_\infty$ is obtained, a $Q$ is designed to guarantee $\|Q(1+T_uL_\infty)\|_\infty<1$.

## 2.4 First-order ILC Based on Mu Synthesis

Based on the analysis in Section III, this section introduces a technique of designing a robust ILC algorithm based on $\mu$ synthesis. In many related papers, the system uncertainty is lumped as $T_u = \hat{T}_u(1+\tilde{N}_T\Delta_T)$, where $\hat{T}_u$ is the nominal closed-loop response from $u^f$ to $e$, $\Delta_T$ is the unknown dynamics (bounded) and $\tilde{N}_T$ is a weighting filter. Such a formulation, however, is difficult to be explicitly related to the uncertainties in the actual plant. In this chapter, the uncertainty is assumed explicitly in $P$, as shown in Figure 2.3, i.e.,

$$P(\Delta) = \hat{P}(1 + \tilde{N}\Delta) \tag{2.17}$$

where $\hat{P}$ is the nominal model, $\Delta$ is the unknown dynamics with $\|\Delta\|_\infty<1$, and $\tilde{N}$ is the weighting filter (system dependent) to characterize $\Delta$ over different frequencies. The multiplicative uncertainty model in Equation (2.17) can capture a wide variety of plant variations. As shown in Figure 2.3, with the uncertainty described in Equation (2.17), $T_u(\Delta)$ becomes

$$\begin{aligned} T_u(\Delta) &= F_u(H, \Delta) \\ &= H_{21}\Delta(I - H_{11}\Delta)^{-1}H_{12} + H_{22} \end{aligned} \tag{2.18}$$

where $F_u(\cdot)$ is the upper LFT, and $H$ is defined as

$$\begin{bmatrix} h \\ y \end{bmatrix} = \begin{bmatrix} H_{11} & H_{12} \\ H_{21} & H_{22} \end{bmatrix} \begin{bmatrix} s \\ u^f \end{bmatrix} \tag{2.19}$$

with

$$\begin{aligned} H_{11} &= -\tilde{N}(1 + \hat{P}C)^{-1}C\hat{P} & H_{12} &= \tilde{N}(1 + \hat{P}C)^{-1}C \\ H_{21} &= (1 + \hat{P}C)^{-1}\hat{P} & H_{22} &= (1 + \hat{P}C)^{-1}\hat{P}C \end{aligned} \tag{2.20}$$

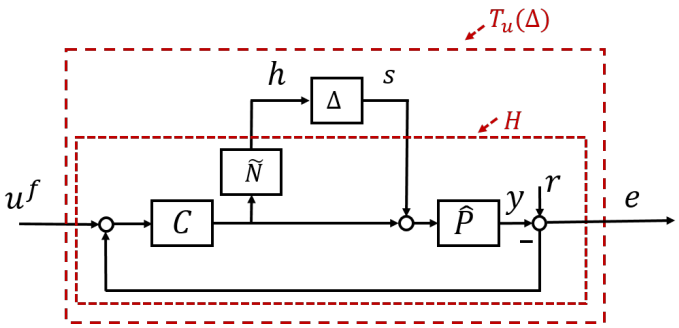


Figure 2.3: Uncertainties in $P$.

Similar to the formulation of $H_\infty$-based ILC, the following optimization problem can be formulated

$$\min_{L_\mu} \|(1 + T_\mu(\Delta)L_\mu)W\|_\infty \tag{2.21}$$

where $L_\mu$ denotes the learning filter designed based on $\mu$ synthesis. To solve the optimization problem in Equation (2.21), a fictitious feedback control system is constructed in Figure 2.4, whose closed-loop transfer function is $T_{zw}(\Delta)$=$F_l[F_u(F, \Delta), L_\mu]$, and $F$ is defined as in Figure 2.4. The following is to show that $T_{zw}(\Delta)$ is exactly the transfer function whose $H_\infty$-norm

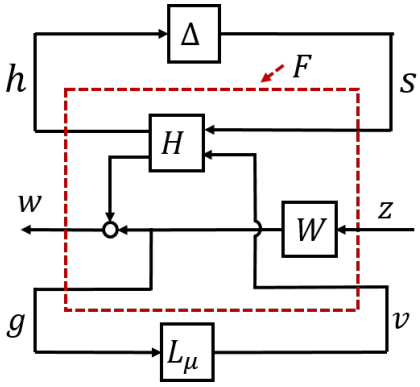


Figure 2.4: Constructed feedback system (with uncertainties) for first-order ILC

is to be minimized, i.e.,

$$T_{zw}(\Delta) = (1 + T_u(\Delta)L_\mu)W \tag{2.22}$$

From Figure 2.4,

$$\begin{bmatrix} h \\ w \\ g \end{bmatrix} = F \begin{bmatrix} s \\ z \\ v \end{bmatrix} = \begin{bmatrix} H_{11} & 0 & H_{12} \\ H_{21} & W & H_{22} \\ 0 & W & 0 \end{bmatrix} \begin{bmatrix} s \\ z \\ v \end{bmatrix} \tag{2.23}$$

Noting $v{=}L_\mu g$, $s{=}\Delta h$ and Equation (2.23),

$$\begin{aligned} h &= H_{11}s + H_{12}v \\ &= H_{11}\Delta h + H_{12}L_\mu g \\ &= H_{11}\Delta h + H_{12}L_\mu W z \end{aligned} \tag{2.24}$$

we have

$$h = [1 - H_{11}\Delta]^{-1}H_{12}L_\mu W z \tag{2.25}$$

Therefore, from Equations (2.23) and (2.25),

$$\begin{aligned} w &= H_{21}s + Wz + H_{22}v \\ &= H_{21}\Delta h + Wz + H_{22}L_\mu W z \\ &= (H_{21}\Delta[1 - H_{11}\Delta]^{-1}H_{12}L_\mu + 1 + H_{22}L_\mu)Wz \\ &= [(H_{21}\Delta[1 - H_{11}\Delta]^{-1}H_{12} + H_{22})L_\mu + 1]Wz \end{aligned} \tag{2.26}$$

Considering Equation (2.18), we have

$$w = [1 + T_u(\Delta)L_\mu]Wz \tag{2.27}$$

Therefore, Equation (2.22) holds. The optimization problem in Eq. (2.21) becomes a standard $\mu$ synthesis problem for the system in Figure 2.4. $D$-$K$ iterations can be utilized to solve the problem [75–77] . As long as $\|Q(1{+}T_u(\Delta)L_\mu)\|_\infty{<}1$, the ILC algorithm in Equation (2.6) can guarantee the stability in spite of the uncertainty in $P$ (Figure 2.3).

## 2.5 Arbitrary-order ILC

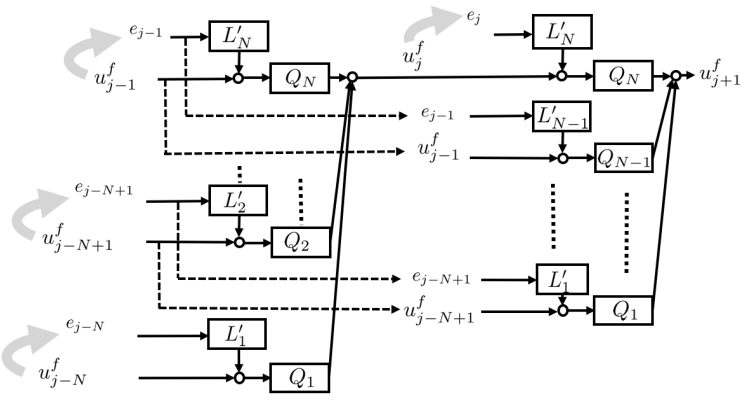


Figure 2.5: High-order ILC

As mentioned in the introduction, the high-order ILC can perform better (faster convergence or robustness to certain non-repetitive disturbances) with more designing effort in the

learning filters. This section extends the $H_\infty$ and $\mu$ syntheses for the first-order ILC to the ones for the high-order ILC. A general Nth-order ILC (which uses both the control signals and the error signals from N preceding iterations) has a standard learning law as follows [78]

$$u^f_{j+1} = \sum_{i=1}^{N} Q_i \left( u^f_{j-N+i} + L'_i e_{j-N+i} \right) \tag{2.28}$$

which is illustrated by Figure 2.5. Substituting Equation (2.28) into Equation (2.4), we have

$$\begin{aligned} e_{j+1} &= T_u \sum_{i=1}^{N} Q_i \left( u^f_{j-N+i} + L'_i e_{j-N+i} \right) + T_d d + T_r r \\ &= \sum_{i=1}^{N} Q_i \left( T_u u^f_{j-N+i} + T_d d + T_r r \right) \\ &\quad + \sum_{i=1}^{N} Q_i T_u L'_i e_{j-N+i} + (1 - Q_f)(T_d d + T_r r) \\ &= \sum_{i=1}^{N} Q_i \left( 1 + T_u L'_i \right) e_{j-N+i} + (1 - Q_f)(T_d d + T_r r) \end{aligned} \tag{2.29}$$

where $\sum_{i=1}^{N} Q_i = Q_f$. Similar to the first-order ILC, $Q_f$ ideally equals to 1. In practice, $Q_f$ is often designed as a low-pass filter with a specific bandwidth to gain robustness. If $Q_f = 1$, the tracking error during the $(j+1)^{\text{th}}$ iteration is

$$e_{j+1} = \sum_{i=1}^{N} Q_i \left( 1 + T_u L'_i \right) e_{j-N+i} \tag{2.30}$$

which can be rewritten as

$$\begin{aligned} \begin{bmatrix} e_{j-N+2} \\ e_{j-N+3} \\ \vdots \\ e_j \\ e_{j+1} \end{bmatrix} &= \begin{bmatrix} 0 & 1 & 0 & \cdots & 0 \\ 0 & 0 & 1 & \cdots & 0 \\ \vdots & \vdots & \vdots & \cdots & \vdots \\ 0 & 0 & 0 & \cdots & 1 \\ T_1 & T_2 & T_3 & \cdots & T_N \end{bmatrix} \begin{bmatrix} e_{j-N+1} \\ e_{j-N+2} \\ \vdots \\ e_{j-1} \\ e_j \end{bmatrix} \\ &\triangleq J E_{j-1} \end{aligned} \tag{2.31}$$

where $T_i = Q_i(1 + T_u L'_i), \forall i = 1, 2, ..., N$. Some related papers (e.g.[67]) on high-order ILC mentioned that if $\|J\|_\infty < 1$ the system is monotonically convergent over iterations. This is correct for general linear systems but not applicable for the system (2.31): $\|J\|_\infty \geq 1$ in Equation (2.31). Therefore, for high-order ILC, it is very difficult to guarantee the monotonic convergence in general. Instead, the system in Equation (2.31) is stable if [63]

$$\|e_{j+1}\|_2 < \max\{\|e_i\|_2,\ i = j, ..., j - N + 1\} \tag{2.32}$$

**Proposition 1:** A sufficient condition for the stability of the system in Equation (2.31) in the sense of Equation (2.32) is that $\begin{bmatrix} T_1 & T_2 & \cdots & T_N \end{bmatrix}$ is stable and

$$\| \begin{bmatrix} T_1 & T_2 & \cdots & T_N \end{bmatrix} \|_\infty < \frac{1}{N} \tag{2.33}$$

**Proof:** Equation (2.33) implies that

$$\|T_i\|_\infty < \frac{1}{N} \tag{2.34}$$

which further implies that

$$\sum_{i=1}^{N} \|T_i\|_\infty < 1 \tag{2.35}$$

Considering Equation (2.35) and

$$\begin{aligned} \|e_{j+1}\|_2 &= \|T_1 e_{j-N+1} + ... + T_N e_j\|_2 \\ &\leq \|T_1 e_{j-N+1}\|_2 + ... + \|T_N e_j\|_2 \\ &\leq \|T_1\|_\infty \|e_{j-N+1}\|_2 + ... + \|T_N\|_\infty \|e_j\|_2 \\ &\leq (\|T_1\|_\infty + ... + \|T_N\|_\infty) \max\{\|e_{j-N+1}\|_2, ..., \|e_j\|_2\} \\ &\leq \max\{\|e_{j-N+1}\|_2, ..., \|e_j\|_2\} \end{aligned} \tag{2.36}$$

Equation (2.32) holds and the system of Equation (2.31) is stable in the sense of Equation (2.32). It is worth noting that condition (2.33) is a conservative condition which can be relaxed to condition (2.35). ■

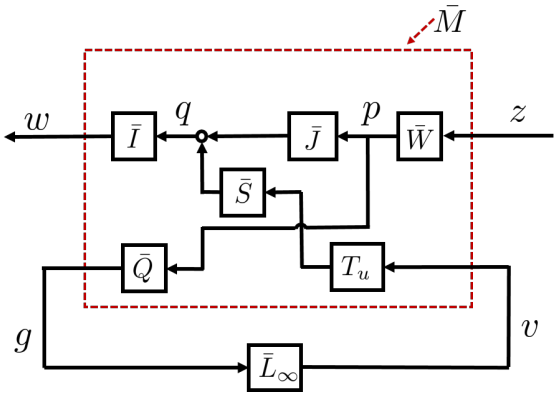


Figure 2.6: Constructed feedback system for high-order ILC

Similar to the formulation of the first-order ILC, the following $H_\infty$ optimization problem can be formulated

$$\min_{[L_{ki}]_{N\times N}} \| \begin{bmatrix} T_1 W_1 & T_2 W_2 & \cdots & T_N W_N \end{bmatrix} \|_\infty \tag{2.37}$$

To solve Equation (2.37), a fictitious feedback system is constructed in Figure 2.6, where $\bar{L}_\infty = [L_{ki}]_{N\times N}$ is to be designed, and

$$\bar{J} = \left[\begin{array}{c:ccc} 0_{N-1,1} & I_{N-1.N-1} & & \\ \hdashline Q_1 & Q_2 & \cdots & Q_N \end{array}\right] \tag{2.38}$$

$$\bar{I} = \left[\begin{array}{c:c} 0_{1,N-1} & 1 \end{array}\right] \tag{2.39}$$

$$\bar{S} = \begin{bmatrix} 0_{N-1,1} & 0_{N-1,1} & \cdots & 0_{N-1,1} \\ 1 & 1 & \cdots & 1 \end{bmatrix} \tag{2.40}$$

$$\bar{W} = \text{diag}\{W_1,\ W_2,\ \cdots,\ W_N\} \tag{2.41}$$

$$\bar{Q} = \text{diag}\{Q_1,\ Q_2,\ \cdots,\ Q_N\} \tag{2.42}$$

The following proposition shows that the closed-loop response of the system in Figure 2.6 equals to the transfer function whose $H_\infty$ norm is to be minimized in Equation (2.37).

**Proposition 2**: With the definition of $\bar{M}$ in Figure 2.6, and the definitions of $\bar{J}$, $\bar{I}$, $\bar{S}$, $\bar{W}$ and $\bar{Q}$ in Equations (2.38)-(2.42), by setting $L'_i = \sum_{k=1}^{N} L_{ki}$ with $\bar{L}_\infty = [L_{ki}]_{N\times N}$,

$$T_{zw} \triangleq L_f(\bar{M}, \bar{L}_\infty) = \begin{bmatrix} T_1W_1 & T_2W_2 & \cdots & T_NW_N \end{bmatrix}.$$

**Proof**: From the definition of $\bar{M}$ with the input $[z\ v]^T$ and the output $[w\ g]^T$, as shown in Figure 2.6, we have

$$\begin{bmatrix} w \\ g \end{bmatrix} = \bar{M} \begin{bmatrix} z \\ v \end{bmatrix} = \begin{bmatrix} \bar{I}\bar{J}\bar{W} & \bar{I}\bar{S}T_u \\ \bar{Q}\bar{W} & 0 \end{bmatrix} \begin{bmatrix} z \\ v \end{bmatrix} \tag{2.43}$$
$$v = \bar{L}_\infty g$$

Further,

$$\begin{aligned} w &= \bar{I}\bar{J}\bar{W}z + \bar{I}\bar{S}T_u\bar{L}_\infty g \\ &= \bar{I}(\bar{J} + \bar{S}T_u\bar{L}_\infty\bar{Q})\bar{W}z \\ &= \bar{I}\Bigg(\left[\begin{array}{c:ccc} 0_{N-1,1} & I_{N-1.N-1} & & \\ \hdashline Q_1 & Q_2 & \cdots & Q_N \end{array}\right] \\ &\quad + \left[\begin{array}{c:ccc} 0_{N-1,1} & 0_{N-1.N-1} & & \\ \hdashline Q_1T_uL'_1 & Q_2T_uL'_2 & \cdots & Q_NT_uL'_N \end{array}\right]\Bigg)\bar{W}z \\ &= \left[\begin{array}{c:c} 0_{1,N-1} & 1 \end{array}\right] \left[\begin{array}{c:ccc} 0_{N-1,1} & I_{N-1.N-1} & & \\ \hdashline T_1 & T_2 & \cdots & T_N \end{array}\right] \bar{W}z \\ &= \begin{bmatrix} T_1W_1 & T_2W_2 & \cdots T_NW_N \end{bmatrix} z \end{aligned} \tag{2.44}$$

Therefore,

$$T_{zw} = \begin{bmatrix} T_1W_1 & T_2W_2 & \cdots T_NW_N \end{bmatrix} \tag{2.45}$$

■

Assume $T_{zw}$ has the following state-space realization,

$$T_{zw} \backsim \begin{bmatrix} A_c & B_c \\ C_c & D_c \end{bmatrix} \tag{2.46}$$

Then the design of the learning filter $\bar{L}_\infty$ can be formulated as a standard $H_\infty$ optimization problem (which can be transformed into a convex optimization problem with LMI constraints thereafter) to obtain the learning filter matrix $\bar{L}_\mu$:

$$\begin{aligned} \min_{\bar{L}_\infty} \quad & \gamma \\ & \lambda_i(A_c) < 1, \quad \forall i \\ & \|T_{zw}\|_\infty \le \gamma \end{aligned} \tag{2.47}$$

As long as $\|T_{pw}\|_\infty = \|\bar{I}J\| = \|[T_1, T_2, ..., T_N]\|_\infty < 1/N$, based on Proposition 1, the stability condition in Eq.(2.35) can be guaranteed. Otherwise, a different weighting filter matrix can be designed, or additional low-pass or band-pass filters can be multiplied to $Q_f$.

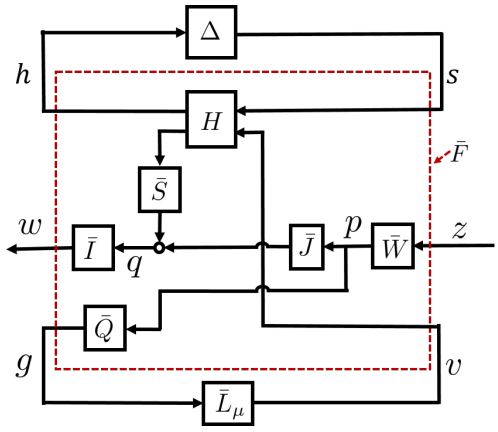


Figure 2.7: Constructed feedback system (with uncertainties) for high-order ILC

To obtain the robustness to large system variations, the multiplicative uncertainty in $P$ (Equation (2.17)) is considered. Similarly, a fictitious feedback system (in Figure 2.7) is constructed, and we have the following proposition.

**Proposition 3:** With the definition of $\bar{F}$ in Figure 2.7, and the definitions of $\bar{J}$, $\bar{I}$, $\bar{S}$, $\bar{W}$ and $\bar{Q}$ in Equations (2.38)-(2.42), by setting $L'_i = \sum_{k=1}^{N} L_{ki}$ with $\bar{L}_\mu = [L_{ki}]_{N\times N}$,

$$\begin{aligned} T_{zw} &\triangleq F_l[F_u(F, \Delta), \bar{L}_\mu] \\ &= \begin{bmatrix} T_1(\Delta)W_1 & T_2(\Delta)W_2 & \cdots & T_N(\Delta)W_N \end{bmatrix}. \end{aligned} \tag{2.48}$$

**Proof**: From Figure 2.7,

$$\begin{bmatrix} h \\ w \\ g \end{bmatrix} = \bar{F} \begin{bmatrix} s \\ z \\ v \end{bmatrix} = \begin{bmatrix} H_{11} & 0 & H_{12} \\ \bar{I}\bar{S}H_{21} & \bar{I}\bar{J}\bar{W} & \bar{I}\bar{S}H_{22} \\ 0 & \bar{Q}\bar{W} & 0 \end{bmatrix} \begin{bmatrix} s \\ z \\ v \end{bmatrix} \tag{2.49}$$

Noting

$$s = \Delta h,\ v = \bar{L}_\mu g = \bar{L}_\mu \bar{Q} \bar{W} z \tag{2.50}$$

we have

$$\begin{aligned} h &= H_{11}s + H_{12}v = H_{11}\Delta h + H_{12}\bar{L}_\mu g \\ &= H_{11}\Delta h + H_{12}\bar{L}_\mu \bar{Q}\bar{W}z \end{aligned} \tag{2.51}$$

Then

$$h = (1 - H_{11}\Delta)^{-1} H_{12}\bar{L}_\mu \bar{Q}\bar{W}z \tag{2.52}$$

Therefore

$$s = \Delta h = \Delta[I - H_{11}\Delta]^{-1} H_{12}\bar{L}_\mu \bar{Q}\bar{W}z \tag{2.53}$$

Considering Equation (2.50) and Equation (2.53)

$$\begin{aligned} w &= \bar{I}\bar{S}H_{21}s + \bar{I}\bar{J}\bar{W}z + \bar{I}\bar{S}\bar{H}_{22}v \\ &= \bar{I}\left[\bar{S}[H_{21}\Delta(I - H_{11}\Delta)^{-1}H_{12} + H_{22}]\bar{L}_\mu\bar{Q} + \bar{J}\right]\bar{W}z \\ &= \bar{I}\left[\bar{J} + \bar{S}T_u(\Delta)\bar{L}_\mu\bar{Q}\right]\bar{W}z \\ &= \bar{I}J(\Delta)\bar{W}z \end{aligned} \tag{2.54}$$

Therefore

$$T_{zw}(\Delta) = \begin{bmatrix} T_1(\Delta)W_1 & T_2(\Delta)W_2 & \cdots & T_N(\Delta)W_N \end{bmatrix} \tag{2.55}$$

■

Similar to the $H_\infty$-based ILC, as long as $\|T_{pw}(\Delta)\|_\infty = \|\bar{I}J(\Delta)\| = \|[T_1(\Delta), ..., T_N(\Delta)]\|_\infty < 1/N$, based on Proposition 1, the stability condition in Equation (2.35) can be guaranteed.

To quantify the guaranteed convergence rate level for ILC with different orders, we provide the following proposition.

**Proposition 4:** Let $\gamma_N$ defined as the $H_\infty$ norm of the closed-loop system from $p$ to $w$ in an $N$th-order ILC system; similarly, let $\gamma_M$ defined as the $H_\infty$ norm of the closed-loop system from $p$ to $w$ in an $M$th-order ILC system. If

$$(\gamma_N)^{\frac{1}{N}} < (\gamma_M)^{\frac{1}{M}} \tag{2.56}$$

then the $N$th-order ILC system has better guaranteed convergence performance than the $M$th-order ILC system.

*Remarks*: Proposition 4 provides an easy and effective theoretical tool to compare the convergence performances with different-order ILCs. For example, if $\gamma_1$=0.8, and $\gamma_2$=0.5; it makes sense to state that the guaranteed convergence rate of the 1st-order ILC is lower than the 2nd-order ILC because $0.8 > 0.5^{1/2}$. It is worth noting that high-order ILC does not necessarily perform better than first-order ILC.

Based on the Proposition 2 and Proposition 3, the ILC design problem has been transfered into feedback controller design problems based on $H_\infty$ synthesis and $\mu$ synthesis respectively. It is worth noting that these ILCs are not guaranteed to satisfy the convergence condition provided

| Notations | Definitions |
|---|---|
| $L$ | Learning filter in general first-order ILC |
| $L_\infty$ | Learning filter in $H_\infty$-based first-order ILC |
| $L_\mu$ | Learning filter in $\mu$-based first-order ILC |
| $L'$ | Learning filter vector in general high-order ILC |
| $\bar{L}_\infty$ | Learning filter matrix in $H_\infty$-based high-order ILC |
| $\bar{L}_\mu$ | Learning filter matrix in $H_\mu$-based high-order ILC |

Table 2.1: Notations of learning filters in different ILCs

in Proposition 1. The condition of Equation (2.32) should be checked after the ILCs have been designed.

Table 2.1 provides the notations of learning filters in different ILCs. For a linear control system as described in Equation (2.1), an $N$th-order ILC control algorithm is designed as described in Figure 2.1 and Equation (2.30); the learning filter matrix is designed based on $H_\infty$ synthesis ($\bar{L}_\infty$) and $\mu$ synthesis ($\bar{L}_\mu$) for the constructed feedback systems in Figure 2.6 and Figure 2.7, respectively. As long as $\|T_{pw}\|_\infty = \|[T_1, T_2, ..., T_N]\|_\infty < 1/N$, the convergence in the sense of Equation (2.32) can be guaranteed. Otherwise, a different $W$ or $Q$ can be designed. Some discussions on the $W$ and $Q$ design are provided in the following section.

## 2.6 Application

The effectiveness of the proposed $H_\infty$-based and $\mu$-based ILCs is demonstrated and validated through simulations and experiments on a wafer scanning system. A desired repetitive trajectory for the scanning system is shown in Figure 1.6. The frequency response of the nominal closed-loop system $T_u$ is provided in Figure 2.8. Furthermore, to demonstrate the benefit of $\mu$-based ILC, large system variations (especially at high frequencies) are purposely added in simulations. The frequency responses of the system with such large variations ($T_u(\Delta)$) are also provided in Figure 2.8. In the following, two comparisons are studied: (1) the first-order and the second-order ILCs; (2) the $H_\infty$-based and the $\mu$-based ILCs.

### First-order and second-order ILCs

This section validates the effectiveness of both first-order and second-order ILCs designed based on $H_\infty$ synthesis, and also demonstrates the benefit of the second-order ILC: the second-order ILC updates the feedforward control signals based on the memory data from previous two iterations, which makes it possible to gain faster convergence compared to the first-order ILC. This comparison is validated through both simulations and experiments. Simulation validation was provided in [73]; here we only provide experimental results to validate the effectiveness of the two ILCs. The results are provided from Figure 2.9 to Figure 2.11.

In the application, for both the first-order and the second-order ILCs, the weighting filters $W$ are designed as a stable, first-order filter that satisfies $W(e^{j0})=2$, $W(e^{j30\cdot 2\pi T_s})=1$ and $W(e^{j\pi})=0.1$.

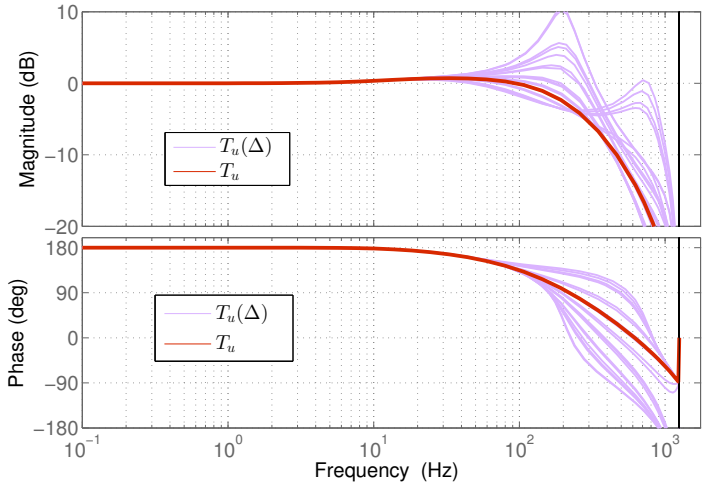


Figure 2.8: Frequency responses of $T_u$ (with and without uncertainties).

This means $(1+L_\infty T_u)$ is expected to be small at low frequencies below 30Hz (cross frequency), which would result a faster convergence performance when the reference is a low-frequency signal. The cross frequency is expected to be higher if the reference has some components at higher frequencies. $Q$ in the first-order ILC and $Q_f$ in the second-order ILC are designed as a low-pass filter with bandwidth of 300 Hz, to gain robustness of system variations beyond 300Hz. The learning filters are obtained through solving the H-infinity optimization problems using the robust control toolbox in MATLAB 2013a, and the order of the learning filters has been reduced to six using approximation. Figure 2.9 shows the frequency responses of corresponding filters in the first-order and second-order ILCs respectively: (1) $W$, $Q$ and $Q(1+L_\infty T_u)$ in the first-order ILC; (2) $W_{1,2}$,$Q_f$,$Q_1$, $Q_2$, $Q_1[1+(L_{11}+L_{21})T_u]$, and $Q_2[1+(L_{12}+L_{22})T_u]$ in the second-order ILC. It is observed that in the first-order ILC, $\|Q(1+L_\infty T_u)\|_\infty < 0dB$ for all $w$. Similarly, in the second-order ILC, $\|Q_2[1+(L_{12}+L_{22})T_u]\|_\infty < \|Q_1[1+(L_{11}+L_{21})T_u]\|_\infty < -6dB$, which guarantees the convergence according to Proposition 1. It is also worth noting that

$$\rho_1 = \|Q(1+L_\infty T_u)\|_\infty = 0.7219$$

and

$$\rho_2 = \|[Q_1[1+(L_{11}+L_{21})T_u,\ Q_2[1+(L_{12}+L_{22})T_u]\|_\infty = 0.0963$$

from which we have

$$\rho_1 > (\rho_2)^{\frac{1}{2}}$$

Therefore, the second-order ILC system here has better guaranteed convergence performance than the first-order ILC system. However, this does not mean that second-order ILC would always perform better than the first-order ILC in general systems.

Figure 2.10 and Figure 2.11 show the tracking errors in the first-order and the second-order ILC systems, in iteration domain and time domain respectively. Using the proposed ILC algorithms, the tracking errors are significantly reduced after 1 iteration and even more after 3 iterations. In

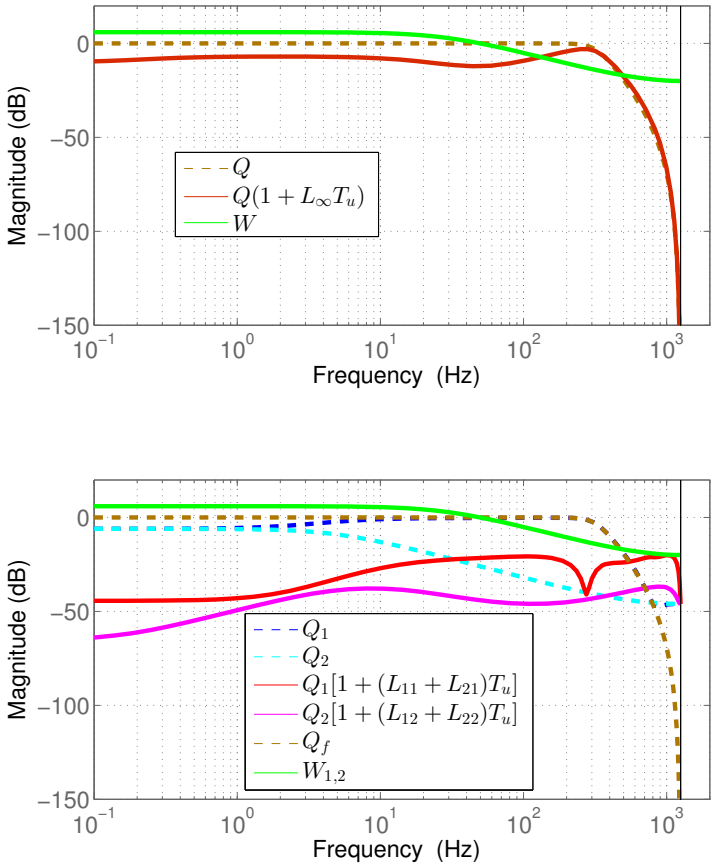


Figure 2.9: Frequency responses of filters ($H_\infty$-based ILC).

the first-order ILC system, the tracking error converges to a small band (1e-5 m) after 3 iterations; while in the second-order ILC system, it takes only 2 iteration for the tracking error to converge into the small band. Figure 2.10 shows the 2-norm of the tracking errors up to 7 iterations in both the first-order and the second-order ILC systems. The second-order ILC utilizes two preceding iteration data and it converges faster than the first-order ILC in this case.

From the experimental results, both the first-order ILC and the second-order ILC designed based on the $H_\infty$ synthesis are effective for the wafer scanning system. Since the second-order ILC utilizes more information and has more design flexibilities than the first-order ILC, with careful design, it is possible to achieve faster convergence than the first-order ILC. In the wafer scanning system, because the tracking error converges into a small region within 2 or 3 iterations, the third-order ILC works very similarly to the second-order ILC. Furthermore, it is worth noting that the tracking error does not converge to zero ultimately; such non-zero steady state errors come from the non-repetitive disturbances in the actual systems.

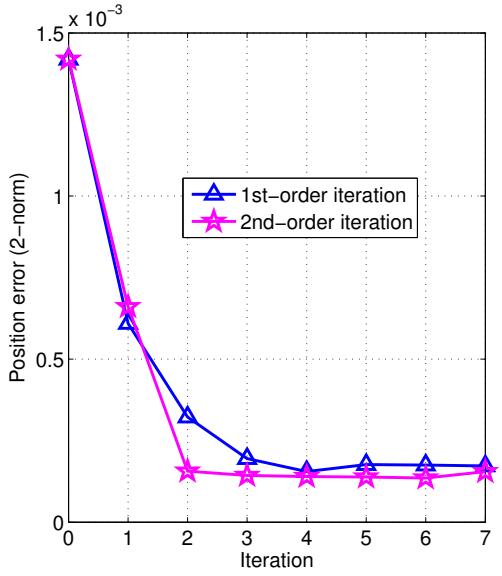


Figure 2.10: Tracking errors in iteration domain ($H_\infty$-based ILC).

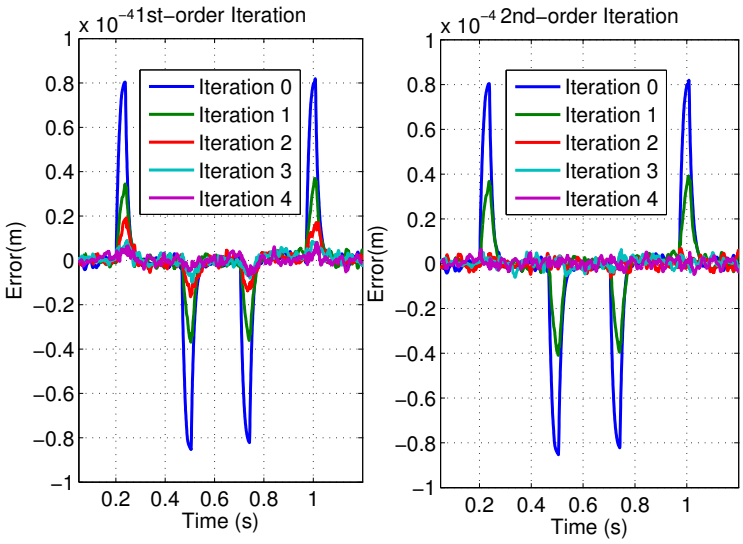


Figure 2.11: Tracking errors in time domain ($H_\infty$-based ILC).

## H-infinity based and $\mu$ based ILCs

This section compares the $H_\infty$-based and the $\mu$-based ILCs, and validates the benefit of the $\mu$-based ILC: the $\mu$-based ILC explicitly considers system variations when designing the learning filters and thus is more robust than the $H_\infty$-based ILC. Since the actual system variations are not large enough to make the ILC system unstable, this comparison is validated by simulation only, and system variations are purposely added in the simulations. This $\mu$-based ILC is promising in

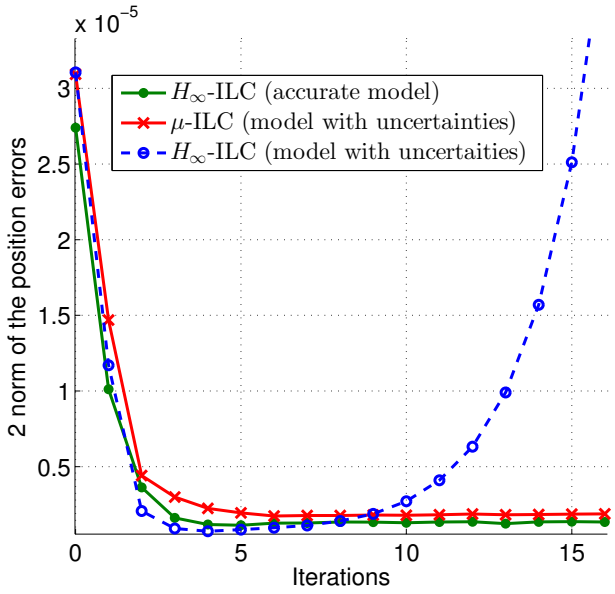


Figure 2.12: Tracking errors in iteration domain ($\mu$-based ILC).

the systems where variations are nontrivial, such as industrial manipulators.

The weighting filter $W$ and the filter $Q$ are with the same design in the $H_\infty$-based ILC. The simulation results are provided in Figure 2.12. The ILC using $H_\infty$ synthesis is designed based on the nominal closed-loop system $T_u$. It is worth noticing that $L_\infty$ is closed to the inverse of $T_u$, which also provides an alternative and interesting way of designing the inverse of a plant. If the injected repetitive $d$ contains high-frequency components (>300Hz), $Q$ is desired to have high bandwidth ($>$ 300 Hz) to suppress these disturbances. Consequently, $Q(1 + L_\infty T_\mu)$ is close to $0dB$ around 300 Hz, which makes the ILC sensitive to system variations, and indicates the necessity of a more conservative learning filter in the presence of the large system variations and high-frequency disturbances. The ILC using $\mu$ synthesis is designed based on the model with large system variations ($T_u(\Delta)$). Figure 2.12 compares the tracking errors up to 15 iterations in the $H_\infty$-based ILC system and the $\mu$-based ILC system, in which large system variations are purposely added. It is observed that these system variations cause instability in the $H_\infty$-based ILC system, while the $\mu$-based ILC system maintains good tracking performance and reasonable convergence rate even with system variations. The ideal case of using $H_\infty$-based ILC simulated on the nominal model without the system variations is also provided in Figure 2.12 for reference.

## 2.7 Chapter Summary

This chapter has proposed a systematic approach to design learning filters for arbitrary-order ILC. It is an off-line optimization procedure performed in iteration-frequency domain with guaranteed convergence and ease of tuning. A feedback system is first constructed and the $H_\infty$ optimal control design technique is applied thereafter to obtain the optimal learning filters. This approach is further

advanced based on $\mu$ synthesis to explicitly take system variations into consideration. Important characteristics such as the convergence and robustness are demonstrated and validated through simulations and experiments on a wafer scanning system. Although this framework applies to causal learning filter design, it can easily include the non-causal case by explicitly adding delays into the constructed feedback system. As a follow-up exploration, the proposed framework will be applied to a multi-input-multi-output system and extended to a more generic formulation where an $N$th-order ILC uses the information from both the preceding iterations and the current iteration, which is an optimization procedure that involves both feedforward and feedback controls.

# Chapter 3

# Disturbance Observer

## 3.1 Introduction

Disturbance observer (DOB) is a powerful technique to estimate and compensate the disturbance in high-precision systems. It is a plant-inverse based technique and has many industrial applications including hard disk drives (HDDs) and wafter scanning systems.

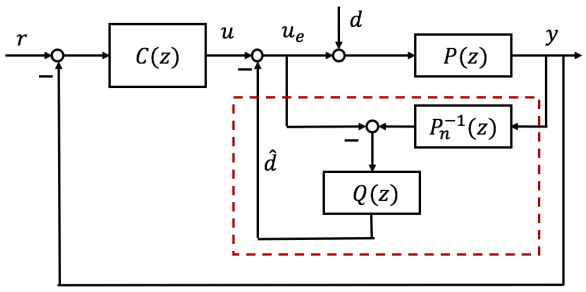


Figure 3.1: A general system with conventional DOB

Figure 3.1 shows a general system with a conventional DOB (in the dash rectangular box), in which $P(z)$ is the plant; $C(z)$ is the baseline feedback controller; $P_n(z)$ is a nominal model of the plant; and $Q(z)$ is a filter to maintain the causality and robustness of the DOB. The reference signal $r$, the output signal $y$, the control signal $u$ generated by $C(z)$, the disturbance $d$, the disturbance estimate $\hat{d}$, and the control signal $u_e$=$u-\hat{d}$ injected into the plant are all defined in this figure. The DOB includes a plant inverse $P_n^{-1}(z)$ and a filter $Q(z)$; the input signals to the DOB are $u_e$ and $y$, and the output signal is $\hat{d}$. The intuitive idea of the conventional DOB is to utilize the inverse of the plant model to reconstruct the plant's input signals which consist of the control signal $u_e$ and the actual disturbance $d$. A general DOB design procedure includes two steps: (1) design a stable inverse of the plant; and (2) design a Q-filter to maintain the causality and robustness. The plant inverse is usually obtained from a low-order nominal model of the plant. The Q-filter can be designed as a low/high/band-pass filter based on the frequency characteristics of the disturbance and the uncertainties in the plant.

Among numerous DOB design algorithms developed in recent years, robust control theory has been utilized with guaranteed stability and robustness of the systems [79–82]. In [79], the DOB design problem was transformed into the $H_\infty$ synthesis problem by finding an optimal static output feedback gain for an extended plant. In [80–82], the Q-filter was designed through solving an $H_\infty$ optimization problem. However, these DOB design procedures were only applied to single-input-single-output (SISO) systems and were based on the conventional DOB structure that requires a well-designed stable inverse of plant. Usually designing a stable plant inverse is not trivial for some SISO systems and even more challenging for multi-input-multi-output (MIMO) systems.

There exist some DOB design methods for MIMO systems in the literature. For example, the method in [83] treated each input-output channel of the plant separately by ignoring the coupling effect. However, this introduced plant modeling errors and the stability was difficult to guarantee. An alternative method proposed in [3] first decoupled the system using the nominal model of the plant and then followed the conventional DOB design procedure for SISO systems. These techniques did not mitigate the issue of designing a good plant inverse in the DOB design. Furthermore, most of them were only applicable to the square systems: systems with the same dimensions of the inputs and outputs. It is rather challenging to apply these DOB techniques to the systems with the inputs of higher dimension than the outputs.

To unnecessitate plant inverse and apply DOB to a general class of MIMO plant, instead of following the conventional DOB structure, this chapter formulates the DOB design problem into an $H_\infty$ optimization problem by treating the whole observer as a 'black' box without specifying any explicit structure [4]. The proposed design methodology is different from the existing $H_\infty$ design methods for DOBs which still follow the conventional DOB structure with well-designed plant inverse and Q-filters. Being relaxed from the restrictions due to the conventional the DOB structure, the proposed approach has more design flexibilities and is possible to achieve better performance than the conventional DOB. It is also worth mentioning that the proposed DOB is still an add-on algorithm aiming to estimate and compensate the disturbance without redesigning the baseline feedback controller.

## 3.2 Conventional DOB Design Methodology

As stated in the introduction, with well-defined $P_n^{-1}(z)$ and $Q(z)$, the DOB can recover the actual disturbance over specified frequency ranges. To further explain this, the transfer function from $d$ to $\hat{d}$ is derived as follows. From Figure 3.1,

$$\hat{d} = Q(z)[P_n^{-1}(z)y - (u - \hat{d})] \tag{3.1}$$

which implies

$$(1 - Q(z))\hat{d} = Q(z)P_n(z)^{-1}y - Q(z)u \tag{3.2}$$

Noting that $y{=}P(z)[u{-}\hat{d}{+}d]$ and $u{=}-C(z)y$,

$$y = P(z)[-C(z)y - \hat{d} + d] \tag{3.3}$$

which implies

$$y = [1 + P(z)C(z)]^{-1}P(z)(d - \hat{d}) \tag{3.4}$$

Substituting $u=-C(z)y$ and Equation (3.4) into Equation (3.1), after some manipulations, we have

$$\hat{d} = \frac{Q[P_n^{-1}P + PC][1+PC]^{-1}}{(1-Q) + Q[P_n^{-1}P + PC][1+PC]^{-1}} d \tag{3.5}$$

where $z$ is omitted for simplicity. Note that if

$$Q(z) = 1 \tag{3.6}$$

and

$$P_n^{-1}(z)P(z) = 1 \tag{3.7}$$

then $d=\hat{d}$, which means that the actual disturbance $d$ is completely reconstructed.

In general there are three considerations in DOB design: stability, causality, and robustness. (1) Stability: if $P(z)$ is a non-minimum phase model (i.e., the zeros of $P(z)$ are unstable), there does not exist a stable plant inverse satisfying Equation (3.7); an alternative stable plant inverse satisfying $P_n^{-1}(z)P(z)\approx 1$ should be designed. (2) Causality: if $P(z)$ is strictly causal, then its inverse is non-causal and not realizable; a $Q(z)$ needs to be designed such that $Q(z)P_n^{-1}(z)$ is causal. (3) Robustness: if there exist some uncertainties in $P(z)$, i.e., $P(z) = P_n(z)(1+\Delta(z))$ where $\Delta(z)$ denotes bounded un-modeled dynamics, $Q(z)$ needs to be designed such that robustness of the system is guaranteed. Detailed discussions can be found in [84].

## 3.3 Reformulation of DOB

This section formulates the DOB design problem into an $H_\infty$ optimization problem based on robust control theory. Define $T_f(z)$ as the transfer function from $d$ to $(d-\hat{d})$, i.e.,

$$d - \hat{d} = T_f(z)d \tag{3.8}$$

From Equation (3.5),

$$T_f = 1 - \frac{Q[P_n^{-1}P + PC][1+PC]^{-1}}{(1-Q) + Q[P_n^{-1}P + PC][1+PC]^{-1}} \tag{3.9}$$

In this section, the DOB design problem is transfered into the minimization of the $H_\infty$ norm of $T_f(z)$, i.e., $\|T_f(z)\|_\infty$, which is defined as the supremum of the maximum singular value of $T_f(e^{j\Theta})$ $(\Theta \in [0, 2\pi))$,

$$\|T_f(z)\|_\infty = \sup_{\Theta\in[0,2\pi)} \bar{\sigma}[T_f(e^{j\Theta})] \tag{3.10}$$

where $\bar{\sigma}[\cdot]$ denotes the maximum singular value of a matrix. If $\bar{\sigma}[T_f(e^{j\Omega})]$ is small over certain frequency range, $(d-\hat{d})$ would be small, and thus $\hat{d}$ is a good estimate of $d$ over this frequency range.

Assume $T_f(z)$ has the following state-space realization:

$$T_f : \left[\begin{array}{c} x_c(k+1) \\ \hdashline d(k) - \hat{d}(k) \end{array}\right] = \left[\begin{array}{c:c} A_c & B_c \\ \hdashline C_c & D_c \end{array}\right] \left[\begin{array}{c} x_c(k) \\ \hdashline d(k) \end{array}\right] \tag{3.11}$$

The following optimization is formulated to achieve the best disturbance estimate in the sense of the smallest $\|T_f(z)\|_\infty$,

$$\begin{aligned} \min_{Q(z),\ P_n^{-1}(z)} \quad & \|T_f(z)\|_\infty \\ \text{s.t.} \quad & \lambda_i(A_c) \leq 1\ \forall i \\ & Q(z)P_n^{-1}(z) \text{ causal} \end{aligned} \tag{3.12}$$

where $\lambda_i(A_c)$ denotes the $i^{th}$ eigenvalue of $A_c$. The optimization problem (3.12) is very difficult to solve: it is not convex with respect to the decision variables $Q(z)$ and $P_n^{-1}(z)$. To transform it into a convex optimization problem, the following new variable $D(z)$ is introduced:

$$D(z) = [D_1(z) \quad D_2(z)] = [-Q(z) \quad Q(z)P_n^{-1}(z)] \tag{3.13}$$

This leads to a new expression of $T_f(z)$ with respect to the new variable $D(z)$, as the following proposition describes.

**Proposition**: With the definition of $T_f$ in Equation (3.8), and the definition of $D$ in Equation (3.13), $T_f$ can be written as

$$T_f = F_l(M, D) = M_{11} + M_{12}D(I - \begin{bmatrix} M_{22} \\ M_{32} \end{bmatrix} D)^{-1} \begin{bmatrix} M_{21} \\ M_{31} \end{bmatrix} \tag{3.14}$$

where $F_l$ stands for the linear fractional transformation (LFT), and

$$M = \begin{bmatrix} 1 & -1 \\ -C(1+PC)^{-1}P & 1 - C(1+PC)^{-1}P \\ (1+PC)^{-1}P & (1+PC)^{-1}P \end{bmatrix} \tag{3.15}$$

*Proof*: Figure 3.2 is an equivalence of the system in Figure 3.1. $M$ is the transfer function from

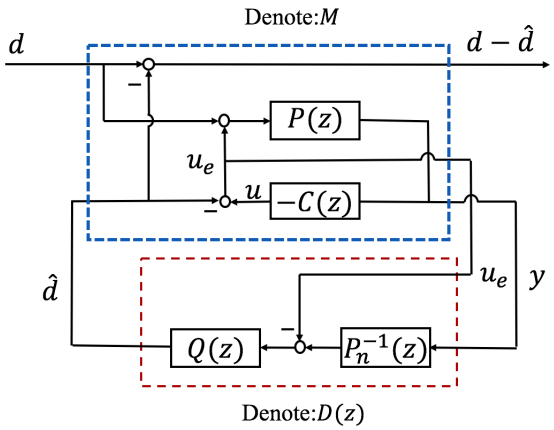


Figure 3.2: Equivalent representation for the system in Figure 3.1

$[d,\ \hat{d}]^T$ to $[d-\hat{d},\ u_e,\ y]^T$. Therefore, $T_f = F_l(M, D)$ as described in Equation (3.14)

Based on the Proposition, the optimization problem (3.12) is reformulated as

$$\begin{aligned} \min_{D(z),\ \text{causal}} \quad & \|F_l(M(z), D(z))\|_\infty \\ \text{s.t.} \quad & \lambda_i(A_c) \leq 1\ \forall i \\ & D_2(z) = -D_1(z)P_n^{-1}(z) \end{aligned} \tag{3.16}$$

for which the decision variable becomes $D(z)$ with the constraint of $D_2(z)=-D_1(z)P_n^{-1}(z)$. This constraint is a requirement induced from the conventional structure of DOB. Here this constraint is relaxed to utilize $H_\infty$ synthesis and to provide more flexibilities in the DOB design. With the constraint relaxing, the optimization problem becomes

$$\begin{aligned} \min_{D(z)\ \text{causal},\ \gamma} \quad & \gamma \\ \text{s.t.} \quad & |\lambda_i(A_c)| < 1 \qquad \forall i \\ & \|F_l(M(z), D(z))\|_\infty < \gamma \end{aligned} \tag{3.17}$$

Compared to the conventional DOB design, the proposed DOB design solves the optimization problem (3.17) over a larger feasible region with the constraint relaxing, which results in a smaller $\gamma$. This optimization problem can be reformulated into a convex optimization problem with linear matrix inequality (LMI) constraints [74] which can be solved efficiently thereafter.

*Remarks:* The main differences between Problem (3.12) and Problem (3.17) arise from two aspects: (a) Problem (3.17) considers $D$ as the decision variable, while Problem (3.12) considers $Q$ and $P_n^{-1}$ as the decision variables; and (b) Problem (3.17) removes the constraint for $D$. With variable transforming and constraint relaxing, Problem (3.17) can be reformulated into a convex optimization problem with LMI constraints based on robust control theory. Furthermore, the proposed DOB design procedure can be modified into the one that explicitly considers system uncertainties based on $\mu$ synthesis.

## 3.4 Application to Dual-stage HDDs

In the literature, the generalized DOB design methodology for dual-stage HDDs has not been fully investigated due to its dual-input-single-output (DISO) plant model whose inverse is not applicable. Using the proposed DOB design procedure, the disturbance can be estimated and compensated in both the voice coil motor (VCM) loop and the piezoelectric motor (PZT) loop.

The classic dual-stage HDD control scheme is shown in Figure 3.3 [85], in which $P_v$ is the VCM plant, $P_m$ is the PZT plant, $C_v$ is the baseline feedback controller for $P_v$, $C_m$ is the baseline feedback controller for $P_m$, and $\hat{P}_m$ is the nominal plant of $P_m$. The signals are also defined in Figure 3.3: $r$ is the reference, $y$ is the output, $d_v$ is the disturbance in the VCM loop, $d_m$ is the disturbance in the PZT loop, and $u_v$ and $u_m$ are the control signals generated by $C_v$ and $C_m$ respectively. The position error signal (PES) is defined as $e=r-y$.

The $H_\infty$-based DOB (denoted as $D$) is designed as shown in Figure 3.4. The input signals to $D$ are $u_{ve}$, $u_{me}$, and $y$; the output signals from $D$ are $\hat{d}_v$ and $\hat{d}_m$; $u_{ve}=u_v-\hat{d}_v$ and $u_{me}=u_m-\hat{d}_m$. Separating the design parameter $D$ from other dynamics in Figure 3.4, an $H_\infty$-based DOB scheme

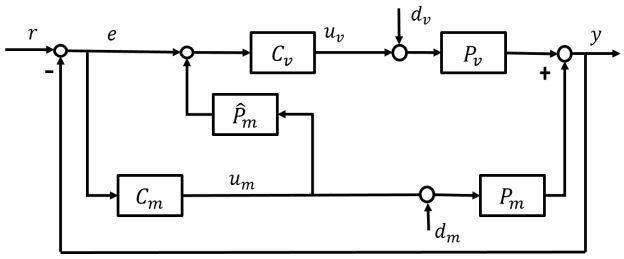


Figure 3.3: Dual-stage HDD

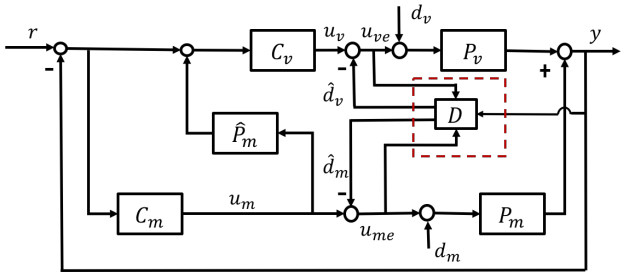


Figure 3.4: Dual-stage HDD with DOB

can be constructed in Figure 3.5, where $C$ and $P$ are

$$C = \begin{bmatrix} (1 + C_m\hat{P}_m)C_v & 0 \\ 0 & C_m \end{bmatrix}, \; P = \begin{bmatrix} P_v & 0 \\ 0 & P_m \end{bmatrix} \tag{3.18}$$

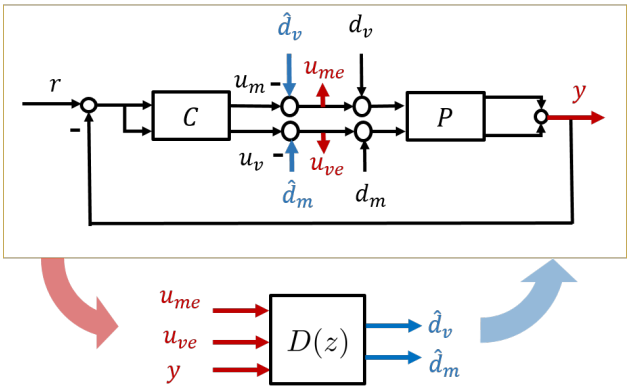


Figure 3.5: $H_\infty$-based DOB design scheme

Denote

$$d = \begin{bmatrix} d_m \\ d_v \end{bmatrix}, \; \hat{d} = \begin{bmatrix} \hat{d}_m \\ \hat{d}_v \end{bmatrix}, \; u_e = \begin{bmatrix} u_{ve} \\ u_{me} \end{bmatrix} \tag{3.19}$$

Define $M(z)$ as the MIMO system with inputs of $[d, \hat{d}]$ and outputs of $[d - \hat{d}, u_e, y]$. A LFT representation of Figure 3.5 is obtained in Figure 3.6 to utilize the $H_\infty$ synthesis. It is easy to

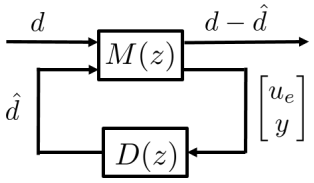


Figure 3.6: LFT representation of Figure 3.5

notice that $M$ has the same mathematical representation as in Equation (3.15). Therefore, the original DOB design problem is transformed into an $H_\infty$ synthesis problem as illustrated in Figure 3.6, i.e.,

$$\min_{D,\ \text{causal, stabilizing}} \|F_l(M, D)\|_\infty \tag{3.20}$$

*Weighting filters*: In general, adding weighting filters is necessary to enhance the performance according to specific requirements. With the following general weighting filters,

$$W(z) = \begin{bmatrix} W_v(z) & 0 \\ 0 & W_m(z) \end{bmatrix} \tag{3.21}$$

the optimization problem becomes

$$\min_{D,\ \text{causal, stabilizing}} \|F_l(M, D)W\|_\infty \tag{3.22}$$

which can be further transformed into a convex optimization problem with LMI constraints as stated in Section III.

## 3.5 Simulation Validation

### SISO Case

In the first simulation study, the proposed DOB is applied to a single-stage HDD with a baseline controller [86]. The disturbance is set as band-limited white noise. The weighting filter is designed as a low-pass filter whose bode plot is provided in Figure 3.7.

The simulation results are provided in Figures 3.8-3.10. Figure 3.8 provides the bode plots of $D(z)$ and an exact non-causal plant inverse $P_n^{-1}(z)$ for comparison. It is worth noting that $D_1(z)$ is close to 1 over a large frequency range, and the causal $D_2(z)$ is very close to the non-causal $P_n^{-1}(z)$. This implies that in SISO systems, $D(z)$ designed by the proposed procedure plays a similar role as $Q(z)$ and $P_n^{-1}Q(z)$ in the conventional DOB. Figure 3.9 provides the closed-loop bode plots from $d$ to $\hat{d}$, which indicates $\hat{d}{\approx}d$ over a large frequency range. Figure 3.10 shows the PES comparison with and without the DOB. It is observed that the PES has been significantly reduced with the proposed DOB.

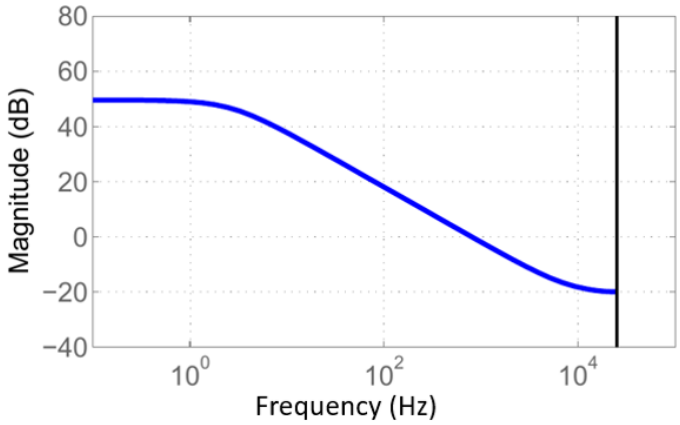


Figure 3.7: Bode plot of the weighting filter

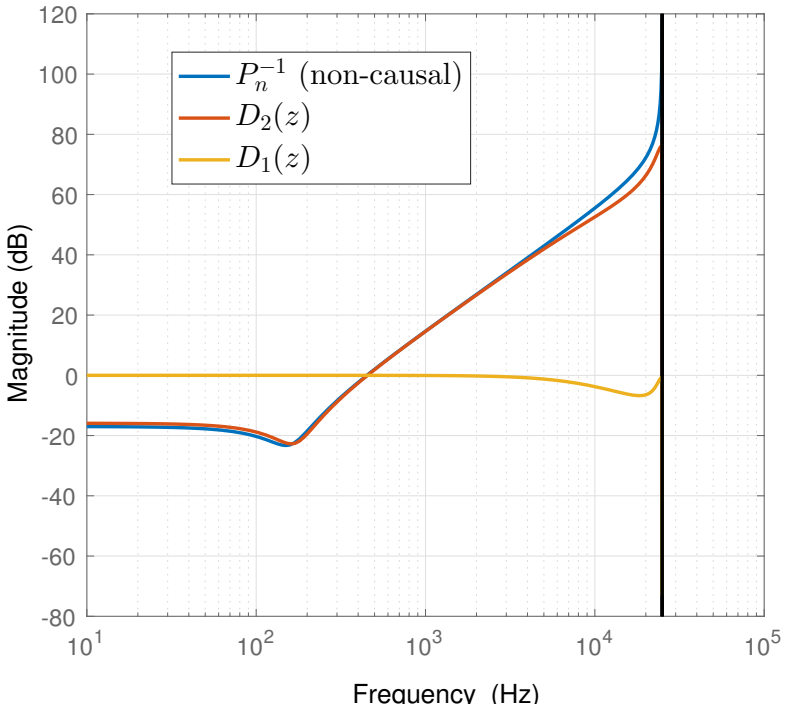


Figure 3.8: Bode plots of the proposed DOB

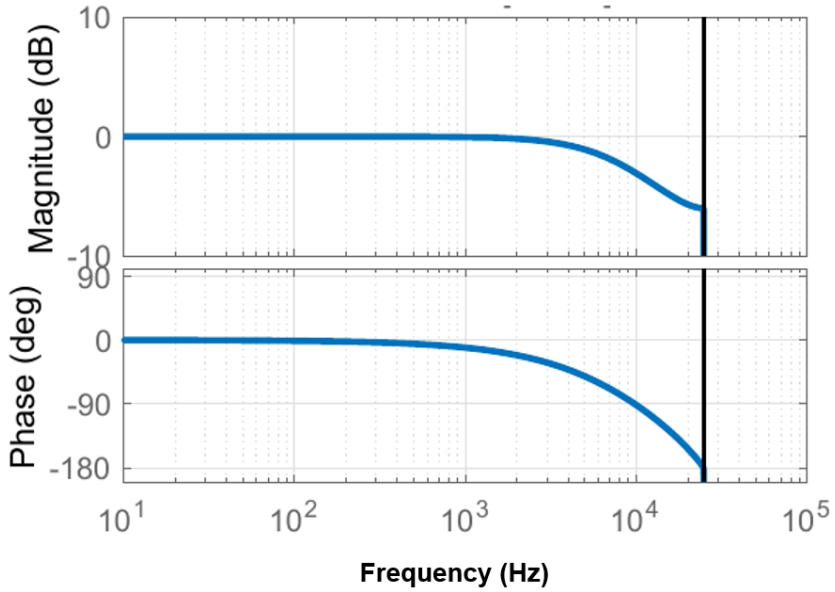


Figure 3.9: Bode plots from $d$ to $\hat{d}$

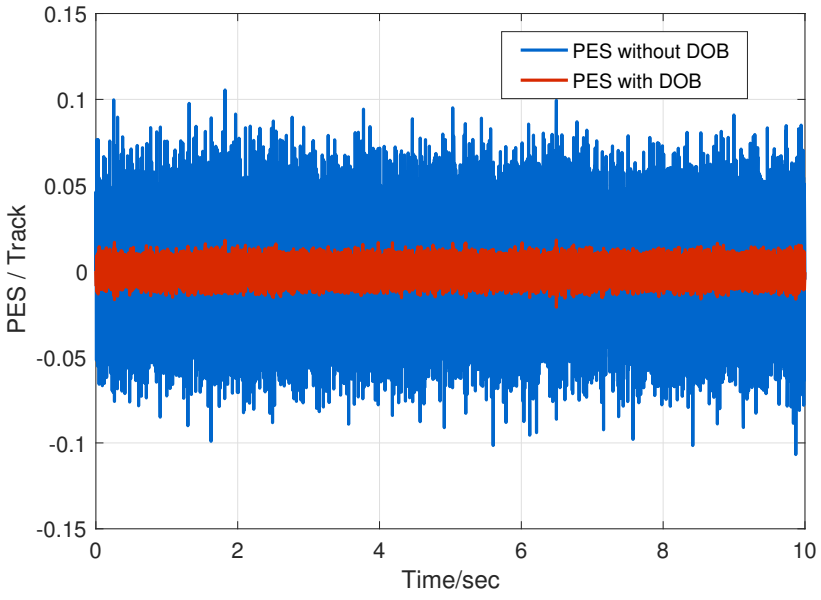


Figure 3.10: PES comparison with and without DOB

## DISO Case

In the second simulation study, the proposed DOB is applied to a dual-stage HDD benchmark model [87]. The weighting filters $W_v(z)$ and $W_m(z)$ are designed based on the frequency characteristics of the disturbance in both the VCM and the PZT loops. Similar to the assumption made in [3], it is assumed that the disturbance in the VCM loop focuses around 1000 Hz and that the disturbance in the PZT loop focuses around 2500 Hz. Therefore, $W_v(z)$ and $W_m(z)$ are designed as band-pass filters or peak filters centered around 1000 Hz and 2500 Hz respectively. Figure 3.11 provides the bode plots of $W_v(z)$ and $W_m(z)$ which are used in this simulation study.

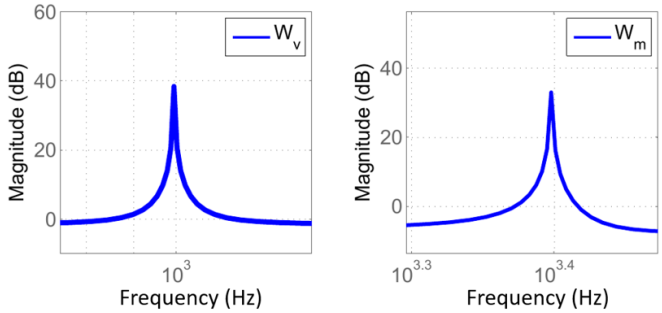


Figure 3.11: Bode plots of weighting filters

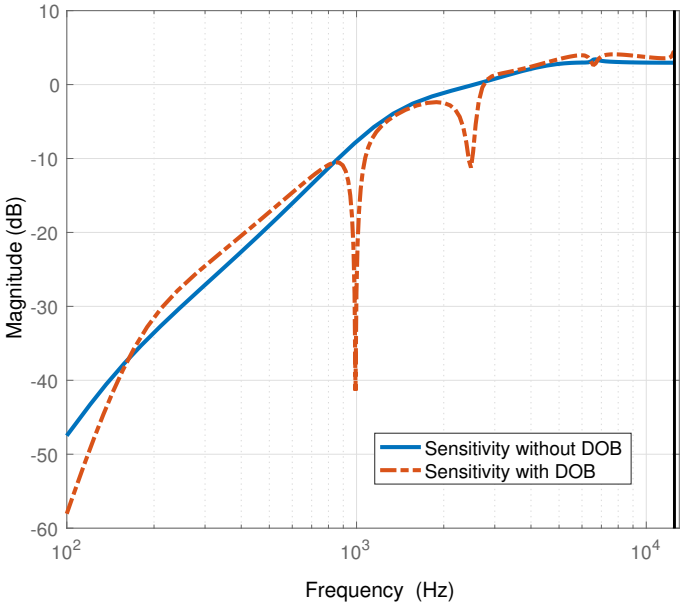


Figure 3.12: Bode plots of sensitivities with and without DOB

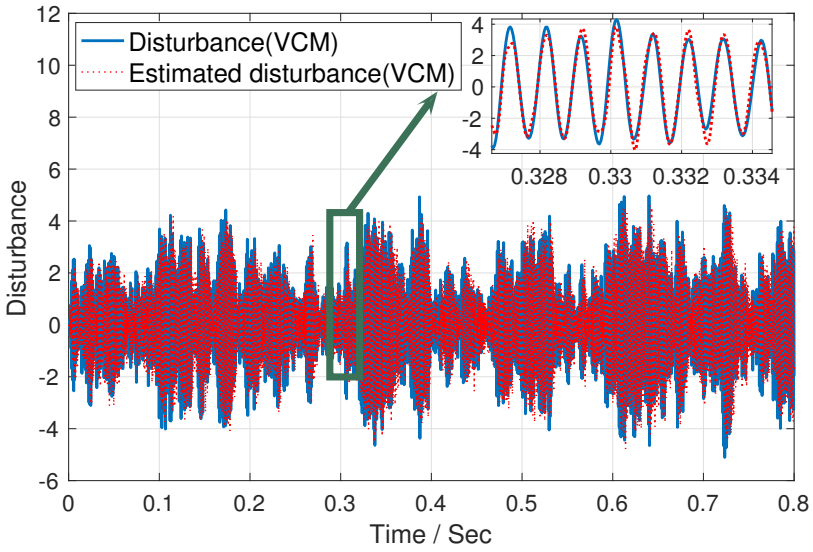


Figure 3.13: Disturbance estimate: $d_v$ and $\hat{d}_v$

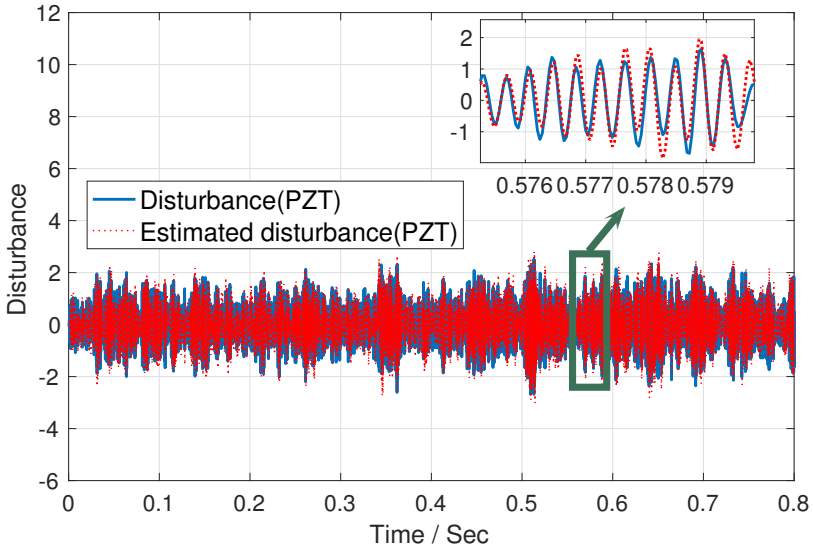


Figure 3.14: Disturbance estimate: $d_m$ and $\hat{d}_m$

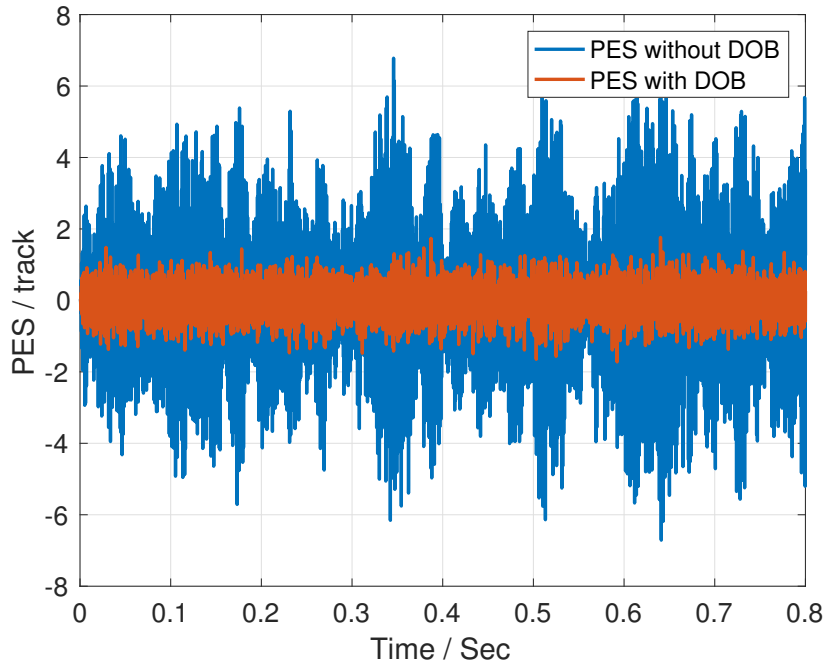


Figure 3.15: PES comparison with and without DOB (time domain)

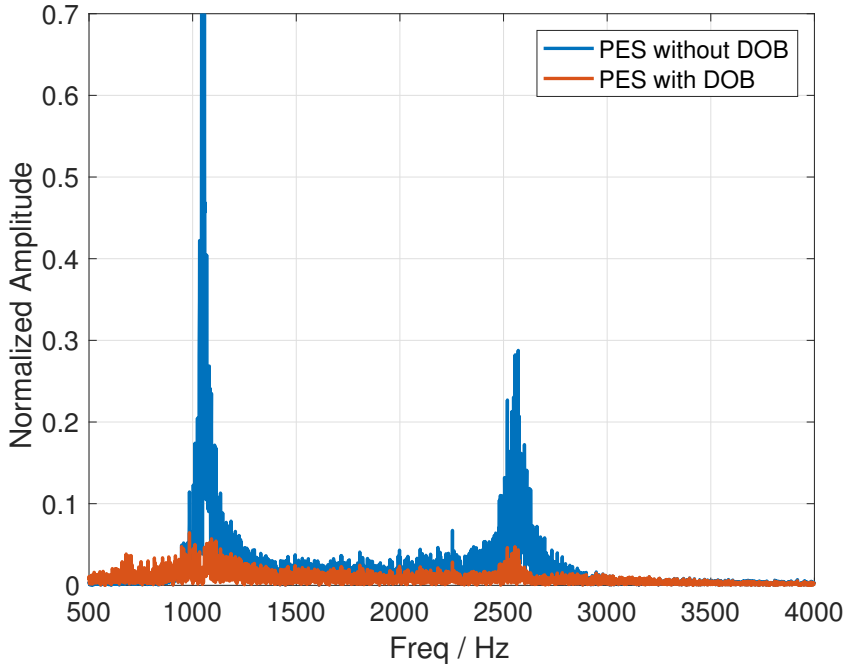


Figure 3.16: PES comparison with and without DOB (frequency domain)

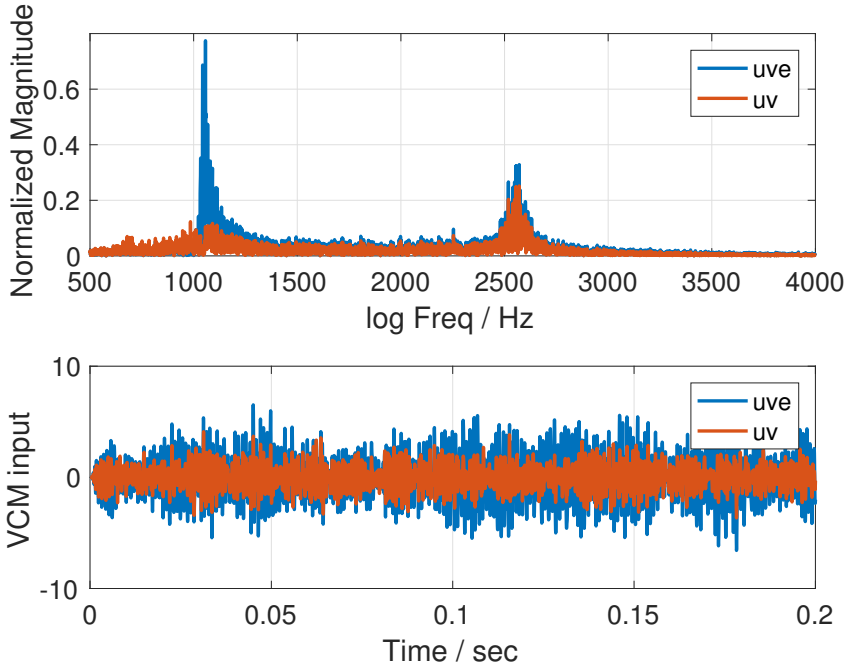


Figure 3.17: Control signal in VCM loop

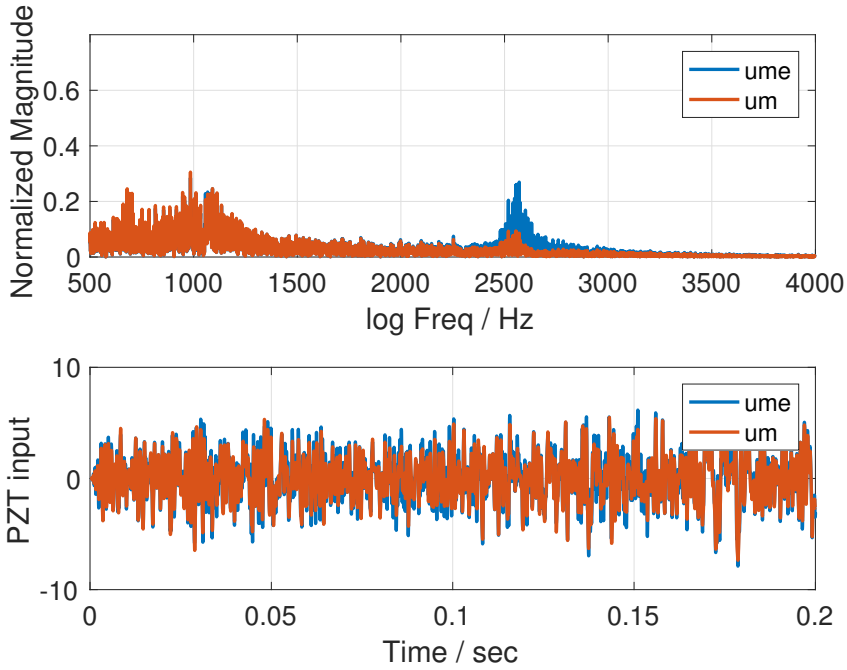


Figure 3.18: Control signal in PZT loop

Simulation results are provided in Figures 3.12-3.18. Figure 3.12 compares the bode plots of the system sensitivities with and without the proposed DOB. It is observed that the dual-stage HDD with the proposed DOB has better vibration attenuation around 1000 Hz and 2500 Hz. Figures 3.13 to 3.16 show a practical case when the input disturbance data is modified from actual on-drive test. Figures 3.13 and 3.14 provide the disturbance estimates: the proposed DOB is able to estimate the disturbance in both the VCM loop and the PZT loop. The PES comparisons (with and without DOB) in both time domain and frequency domain are provided in Figures 3.15 and 3.16 respectively. It is observed from Figure 3.16 that the amplitude of the PES around 1000 Hz and 2500 Hz has been significantly reduced. Figures 3.17 and 3.18 provide the control signals in VCM and PZT loops in both time domain and frequency domain. It is worth noticed that, with the proposed DOB, the control effort around 1000 Hz increases in the VCM loop, while the one around 2500 Hz increases in the PZT loop.

## 3.6 Chapter Summary

A generalized DOB design procedure has been proposed for both SISO systems and MIMO systems based on $H_\infty$ synthesis. The proposed DOB assures the stability and minimizes the weighted $H_\infty$ norm of the dynamics from the disturbance to its estimation error. This DOB design procedure is applicable not only to the square systems, but also to the systems with the inputs of higher dimension than the outputs. Detailed evaluation has been performed on a dual-stage HDD plant that has dual inputs and single output. The simulation results demonstrate the effectiveness of the proposed DOB.

# Chapter 4

# Extended State Observer

## 4.1 Introduction

During the track-following process of hard disk drives (HDDs), the read/write head is expected to stay on the target data track with small position error signal (PES). This process is subjected to vibrations both below and beyond the Nyquist frequency. Most of the external vibrations are below the Nyquist frequency; and the vibrations beyond the Nyquist frequency are mainly caused by the excitation of resonances. This chapter presents two techniques based on the extended state observer (ESO) to estimate the high-frequency vibrations both below and beyond the Nyquist frequency.

Besides the disturbance observer (DOB) technique presented in Chapter 3, ESO, as a special class of the high-gain observers, is an alternative promising method to estimate the disturbances by treating them as state variables. Existing ESO works well for low-frequency disturbance estimation; however, such good performance is not inherited to high-frequency disturbance estimation. The main problem is the phase loss introduced by both the plant and the ESO itself. For low-frequency disturbances, the effect of a small delay is not serious. However, in HDDs, the disturbances usually include large high-frequency components, and a small delay may cause large estimation error. To extend ESO's performance range from low frequencies to high frequencies, this chapter presents a phase compensator to recover the phase loss in the traditional ESO and increases the ESO's estimation bandwidth.

This chapter further pushes the estimation bandwidth of ESO beyond the Nyquist frequency through multi-rate technique based on the priorly known nominal dynamic model of the vibrations. Nyquist frequency limits the frequency range of the continuous-time signals that can be reconstructed through the sampled discrete-time signals. In HDDs, there exist resonance modes near and beyond the Nyquist frequency in the voice coil motor (VCM). Such resonance modes, if excited, may generate vibrations beyond the Nyquist frequency which would seriously degrade the servo performance. To capture such vibrations, motived by the ESO [88, 89] and Kalman filter [90], this chapter presents a multi-rate extended observer to estimate the inter-sample behaviors of the VCM and the vibrations beyond the Nyquist frequency.

## 4.2 ESO: from Low Frequency to High Frequency

Consider a general linear system in continuous time described by

$$\begin{aligned} \dot{x} &= Ax + B(u + d) \\ y &= Cx \end{aligned} \tag{4.1}$$

where $x \in \Re^{n\times 1}$ is the state vector; $y \in \Re$ is the output; $u \in \Re$ is the control input; $d \in \Re$ is the unknown disturbance; $A \in \Re^{n\times n}$; $B \in \Re^{n\times 1}$; and $C \in \Re^{1\times n}$. Assume that $(C, A)$ is observable; $d$ and its derivative $\dot{d}$ are bounded by $\delta_d$ and $\delta_d'$ respectively.

By treating $d$ as a state variable, and $\dot{d}$ as the unknown disturbance, the system (4.1) is rewritten as

$$\begin{aligned} \begin{bmatrix} \dot{x} \\ \dot{d} \end{bmatrix} &= \begin{bmatrix} A & B \\ 0 & 0 \end{bmatrix} \begin{bmatrix} x \\ d \end{bmatrix} + \begin{bmatrix} B \\ 0 \end{bmatrix} u + \begin{bmatrix} 0 \\ 1 \end{bmatrix} \dot{d} \\ y &= \begin{bmatrix} C & 0 \end{bmatrix} \begin{bmatrix} x \\ d \end{bmatrix} \end{aligned} \tag{4.2}$$

Denote

$$\begin{aligned} A_e &= \begin{bmatrix} A & B \\ 0 & 0 \end{bmatrix}, B_e = \begin{bmatrix} B \\ 0 \end{bmatrix}, B_d = \begin{bmatrix} 0 \\ 1 \end{bmatrix} \\ C_e &= \begin{bmatrix} C & 0 \end{bmatrix}, x_e = \begin{bmatrix} x^T & d^T \end{bmatrix}^T \end{aligned}$$

Then

$$\begin{aligned} \dot{x}_e &= A_e x_e + B_e u + B_d \dot{d} \\ y &= C_e x_e \end{aligned} \tag{4.3}$$

A state observer can be designed for the augmented system (4.3) to estimate both the disturbance $d$ and the states $x$.

### Observability Analysis

Before designing the observer for the system (4.3), the observability needs to be analyzed. Define

$$Q(\lambda; A, C) = \begin{bmatrix} A - \lambda I \\ C \end{bmatrix} \tag{4.4}$$

where $I \in \Re^{n\times n}$ is an identity matrix.

**Theorem** (PBH Test) [91]: The system (4.1) is observable if and only if $Q(\lambda; A, C)$ has rank $n$ for all $\lambda \in \mathbb{C}$. Based on this, we have the following proposition.

**Proposition**: System (4.2) is observable if and only if the following two conditions hold:

(a) $(C,\ A)$ is observable;
(b) rank$\{Q(0; A_e, C_e)\}= n+1$, where

$$Q(0; A_e, C_e) = \begin{bmatrix} A & B \\ 0 & 0 \\ C & 0 \end{bmatrix} \tag{4.5}$$

The proof is provided as follows.

(i) *Sufficiency*: we first prove that (a) and (b) imply the observability of the system (4.2). Given any $\lambda \in \mathbb{C}$, the following two cases are considered. (1) If $\lambda \neq 0$: the observability of $(C,\ A)$ implies that rank $\{Q(\lambda; A, C)\} = n$, which further implies that rank $\{Q(\lambda; A_e, C_e\} = n+1$. (2) If $\lambda = 0$: rank$\{Q(0; A_e, C_e)\}= n+1$. Therefore, $\forall\lambda \in \mathbb{C}$, rank$\{Q(\lambda; A_e, C_e)\}= n+1$, which implies that $(C_e, A_e)$ is observable.

(ii) *Necessity*: we now prove that the observability of the system (4.2) implies (a) and (b). (1) The observability of $(C_e, A_e)$ obviously implies the observability of $(C, A)$. (2) The observability of $(C_e, A_e)$ implies that rank$\{Q(\lambda; A_e, C_e)\}= n+1$ $(\forall\lambda \in \mathbb{C})$, which further implies that rank$\{Q(0; A_e, C_e\}= n+1$ by setting $\lambda = 0$. Therefore, the observability of augmented system (4.2) implies conditions (a) and (b).

Many systems satisfy conditions (a) and (b). For example, for the following system matrices,

$$A = \begin{bmatrix} -a_{n-1} & 1 & 0 & \cdots & 0 \\ -a_{n-2} & 0 & 1 & \cdots & 0 \\ \vdots & \vdots & \vdots & \vdots & \vdots \\ -a_0 & 0 & 0 & 0 & 0 \end{bmatrix}, B = \begin{bmatrix} b_{n-1} \\ b_{n-2} \\ \vdots \\ b_0 \end{bmatrix},$$
$$C = \begin{bmatrix} 1 & 0 & 0 & \cdots & 0 \end{bmatrix}$$

as long as $b_0 \neq 0$, conditions (a) and (b) are satisfied.

## Standard Extended State Observer

The standard ESO for the system (4.1) is designed as follows,

$$\begin{aligned} \begin{bmatrix} \dot{\hat{x}} \\ \dot{\hat{d}} \end{bmatrix} = \begin{bmatrix} A & B \\ 0 & 0 \end{bmatrix} \begin{bmatrix} \hat{x} \\ \hat{d} \end{bmatrix} + \begin{bmatrix} B \\ 0 \end{bmatrix} u + \\ \begin{bmatrix} L_x \\ L_d \end{bmatrix} \left( \begin{bmatrix} C & 0 \end{bmatrix} \begin{bmatrix} x \\ d \end{bmatrix} - \begin{bmatrix} C & 0 \end{bmatrix} \begin{bmatrix} \hat{x} \\ \hat{d} \end{bmatrix} \right) \end{aligned} \tag{4.6}$$

where $L_x = [\beta_1\ \beta_2\ ...\ \beta_n]^T$ and $L_d = \beta_{n+1}$. Equation (4.6) is actually a standard state observer for the system (4.2). From (4.2) and (4.6), we have

$$\begin{aligned} \begin{bmatrix} \dot{e}_x \\ \dot{e}_d \end{bmatrix} &= \begin{bmatrix} A - L_x C & B \\ -L_d C & 0 \end{bmatrix} \begin{bmatrix} e_x \\ e_d \end{bmatrix} + B_d \dot{d} \\ e_d &= C_d \begin{bmatrix} e_x & e_d \end{bmatrix}^T \end{aligned} \tag{4.7}$$

where $e_x = x - \hat{x}$ is the state estimation error; $e_d = d - \hat{d}$ is the disturbance estimation error; and $C_d = [0 \quad 1]$. $e_x$ and $e_d$ are preferred to be as small as possible in the presence of unknown $\dot{d}$.

During the design of the ESO (4.6), $\dot{d}$ is actually assumed to be zero, i.e., $\dot{d} = 0$. This explains why standard ESO is only effective for low-frequency disturbance estimation. Let $G_d^{'}$ denote the

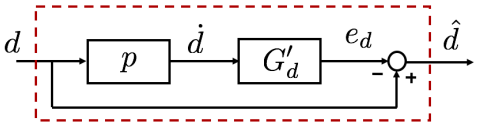


Figure 4.1: Dynamic system from $d$ to $\hat{d}$

transfer function from $\dot{d}$ to $e_d$. From (4.7), we have

$$\begin{aligned} G_d^{'} &= C_d(pI - \begin{bmatrix} A - L_xC & B \\ -L_dC & 0 \end{bmatrix})^{-1}B_d \\ &= (p + L_dC(pI_x - A + L_xC)^{-1}B)^{-1} \end{aligned} \tag{4.8}$$

where $p$ is the Laplace variable. The relationship among $d$, $\hat{d}$ and $\dot{d}$ is shown in Figure 4.1. Let $G_d$ denote the transfer function from $d$ to $\hat{d}$, then

$$\begin{aligned} G_d &= 1 - pG_d^{'} \\ &= 1 - p(p + L_dC(pI_x - A + L_xC)^{-1}B)^{-1} \end{aligned} \tag{4.9}$$

Denote $G_x = C(pI_x - A + L_xC)^{-1}B$, then

$$G_d = 1 - p(p + L_dG_x)^{-1} = \frac{L_dG_x}{p + L_dG_x} \tag{4.10}$$

Ideally, $G_d$=1. The ideal case can be approximated by choosing a large $L_d$. If $L_d \gg 1$ such that $|L_dG_x(jw)| \gg w$, we have $|G_d(j\omega)| \approx 1$ and $\angle G_d(j\omega) \approx 0°$. This explains why high gain ($L_d$) is required for ESO. In practice, $G_d$ proximately performs as a low-pass filter whose bandwidth depends on $L_d$. To ensure accurate state estimates, $L_x$ should also be large enough to reduce the effect of unknown $\dot{d}$. Usually we select $L_d > L_{x,n} > L_{x,n-1} > ... > L_{x,1}$ (i.e., $\beta_{n+1} > \beta_n > ... > \beta_1$).

## Phase Compensation

This section extends the performance range of the standard ESO from low frequencies to high frequencies, based on the assumption that the disturbances' energy is concentrated over a certain frequency range, for example, around $\omega_0$. Figure 4.2 provides the frequency response of $G_d$. It is noticed that at low frequencies, the magnitude of $G_d$ is approximately 1 and the phase of $G_d$ is approximately 0; the standard ESO works well for low-frequency disturbances. As the frequency increases, the phase delay becomes larger and seriously degrades the accuracy of the estimation. In this section, a phase compensator $G_c$ is proposed to recover the phase loss, which results in a compensated ESO.

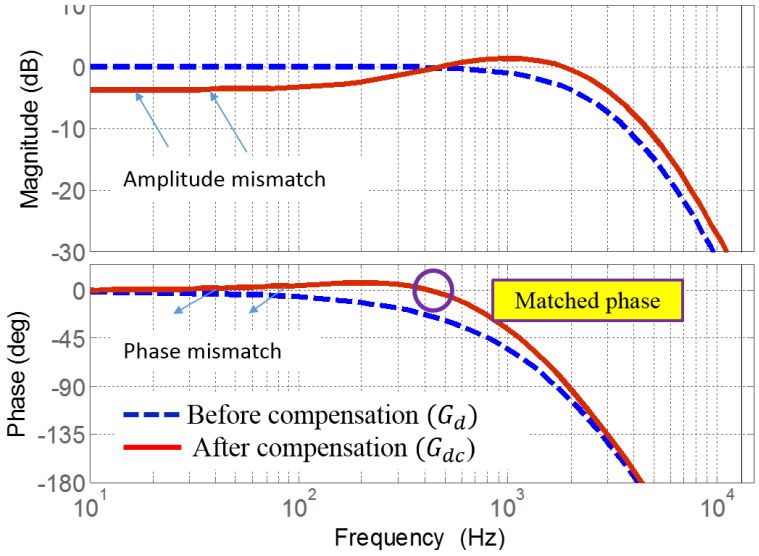


Figure 4.2: Frequency responses of $G_d$ and $G_{dc}$

Let $\hat{d}_c$ denote the estimated disturbance from the compensated ESO. Let $G_{dc}$ denote the transfer function from $d$ to $\hat{d}_c$, i.e.,

$$\hat{d}_c = G_{dc} d = \frac{L_d G_x G_c}{p + L_d G_x} d \tag{4.11}$$

$G_{dc}$ is desired to have zero phase at $\omega_0$. With this goal, $G_c$ is designed as

$$G_c = \frac{p + \omega_0/\phi}{p + \phi\omega_0} \ (\phi > 1) \tag{4.12}$$

Based on (4.12), the phase compensated at $\omega_0$ is

$$\varphi_m = \arcsin \frac{\phi^2 - 1}{\phi^2 + 1} \tag{4.13}$$

where $\phi$ is designed such that $\angle G_{dc}(\omega_0) = 0$, as shown in Figure 4.2. $G_c$ can be realized by the following system:

$$\begin{aligned} \dot{\hat{z}} &= A_c \hat{z} + B_c \hat{d} \\ \hat{d}_c &= C_c \hat{z} + D_c \hat{d} \end{aligned} \tag{4.14}$$

where $A_c = -\phi\omega_0$, $B_c = \omega_0/\phi - \phi\omega_0$, $C_c = 1$, $D_c = 1$. From (4.6) and (4.14), the compensated ESO becomes:

$$\begin{aligned} \begin{bmatrix} \dot{\hat{x}} \\ \dot{\hat{z}} \\ \dot{\hat{d}} \end{bmatrix} &= \begin{bmatrix} A & 0 & B \\ 0 & A_c & B_c \\ 0 & 0 & 0 \end{bmatrix} \begin{bmatrix} \hat{x} \\ \hat{z} \\ \hat{d} \end{bmatrix} + \begin{bmatrix} B \\ 0 \\ 0 \end{bmatrix} u + \begin{bmatrix} L_x(y - C\hat{x}) \\ 0 \\ L_d(y - C\hat{x}) \end{bmatrix} \\ \begin{bmatrix} \hat{x} \\ \hat{d}_c \end{bmatrix} &= \begin{bmatrix} I & 0 & 0 \\ 0 & C_c & D_c \end{bmatrix} \begin{bmatrix} \hat{x} \\ \hat{z} \\ \hat{d} \end{bmatrix} \end{aligned} \tag{4.15}$$

As explained previously, the ESO belongs to the class of high-gain observers. If the initial estimation error is large, such high gains may cause the 'peak phenomenon' and make the linear ESO impractical or even unsafe to use [92, 93]. Here nonlinear gains are designed as in [89] to reduce such 'peak phenomenon'.

### Simulation Validation

Figure 4.3 compares the estimated disturbances by the standard ESO and the compensated ESO. The disturbance source in Figure 4.3a is a sinusoid signal with the frequency of 1000 Hz. It is observed that there is no delay between the disturbance and its estimate by the compensated ESO, while the standard ESO estimates the disturbance with a non-trivial phase delay. The disturbance source in Figure 4.3b is the actual audio vibrations in HDDs, whose energy is concentrated around 1000 Hz. Figure 4.3b shows that the compensated ESO has better disturbance estimate than the standard ESO in the sense of smaller phase delay.

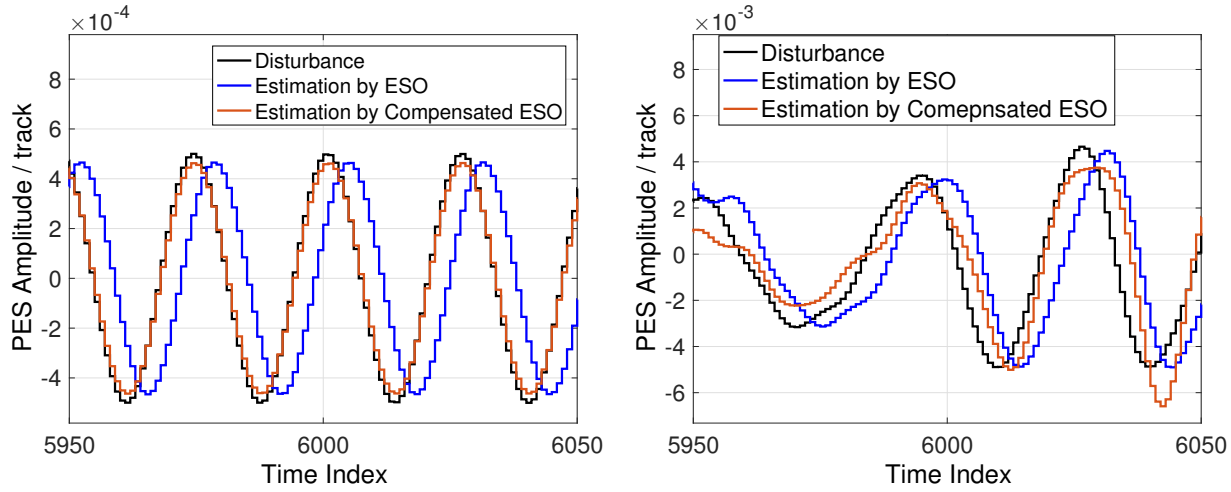


(a) Sinusoid vibrations (b) Audio vibrations

Figure 4.3: Estimated disturbances by ESO

## 4.3 Multi-rate ESO: beyond the Nyquist Frequency

In HDDs, the sampling frequency is strictly limited by the number of the servo sectors which cannot be increased arbitrarily. Meanwhile, one or more resonances beyond the Nyquist frequency exist in the VCM of HDDs and may generate the vibrations which cannot be directly captured by the sampled PES. Such 'unobservable' vibrations may seriously degrade the servo performance, and even wipe data and damage the disks. Therefore, it is important and beneficial to quickly reconstruct and suppress such high-frequency head motions beyond the Nyquist frequency. Reference [94] applied multi-rate notch filters to reduce the gain of the system beyond the Nyquist frequency for the stability purpose. Atsumi, et al. [95–97] derived the sensitivity function in the sampled-data HDD

control systems and designed stable resonant filters. These frequency-domain algorithms were able to decrease the gain of the sensitivity function beyond the Nyquist frequency. There are also some time-domain algorithms aiming to track signals beyond the Nyquist frequency [98].

This section proposes an alternative approach to enhance the servo performance beyond the Nyquist frequency. Considering that the vibrations beyond the Nyquist frequency are usually generated through the excitation of the resonances in HDDs, it is reasonable to assume a known nominal dynamics of the vibrations [99, 100]. By incorporating the vibration dynamics, this section proposes a multi-rate extended observer to estimate the inter-sample behaviors of VCM and high-frequency vibrations [101].

## Problem Description

As mentioned in the introduction, the vibrations beyond the Nyquist frequency may cause large off-track behaviors of the heads which cannot be captured through the sampled PES, as illustrated by Figure 4.4, Therefore, in the presence of such vibrations, a good estimate for the inter-sample behaviors of PES is fundamental to enable fast updating of the control signal and suppress the vibrations beyond the Nyquist frequency.

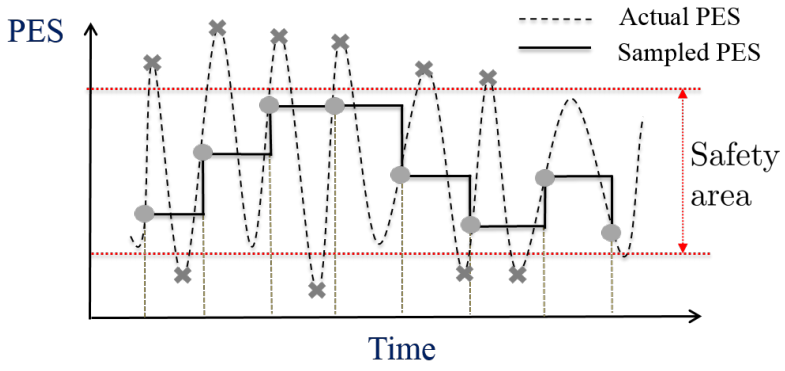


Figure 4.4: PES with components beyond Nyquist frequency

With the vibrations beyond the Nyquist frequency, the HDD control system becomes a multi-rate system with fast vibration injection and slow PES measurement:

$$x_p[(i+1)T_f] = A_p x_p[iT_f] + B_p(u[iT_f] + d[iT_f]) \tag{4.16a}$$
$$y[jT_s] = C_p x_p[jT_s] + v[jT_s] \tag{4.16b}$$

where $x_p$ is the state vector; $u$ is the control signal; $y$ is the measured PES; $d$ is the vibrations; $v$ is the measurement noise; $T_f$ is the control signal updating rate and $T_s$ is the PES sampling rate; $T_s = NT_f$ where $N$ is an integer. $A_p, B_p$ and $C_p$ are the plant matrices with compatible dimensions. The Nyquist frequency is $1/(2T_s)$. To make the notations more clear, rewrite (4.16) as

$$x_p(i+1) = A_p x_p(i) + B_p u(i) + B_p d(i) \qquad (i = 1, 2, 3, ..) \tag{4.17a}$$
$$y(j) = C_p x_p(j) + v(j) \qquad (j = N, 2N...) \tag{4.17b}$$

The control goal is (1) to estimate $x_p$ and $d$ at the fast rate $T_f$ based on the measured PES at the slow rate $T_s$, and (2) to suppress $d$ (which contains the components beyond the Nyquist frequency) through the control signal $u$ which is updated at the fast rate $T_f$.

## Multi-rate Observer

To estimate the inter-sample behaviors of PES and the vibrations, this section proposes a multi-rate extended observer by incorporating the nominal dynamics of the vibrations. This observer is designed based on the techniques of ESO and Kalman filter. ESO allows estimation for both the states and the disturbances by treating the disturbances as state variables [35, 89]. Rewrite the system dynamics (4.17) as follows:

$$\begin{aligned} \begin{bmatrix} x_p(i+1) \\ d(i+1) \end{bmatrix} &= \begin{bmatrix} A_p & B_p \\ 0 & 1 \end{bmatrix} \begin{bmatrix} x_p(i) \\ d(i) \end{bmatrix} + \begin{bmatrix} B_p \\ 0 \end{bmatrix} u(i) + \begin{bmatrix} 0 \\ 1 \end{bmatrix} w(i) \\ y(j) &= \begin{bmatrix} C_p & 0 \end{bmatrix} \begin{bmatrix} x_p(j) \\ d(j) \end{bmatrix} + v(j) \end{aligned} \tag{4.18}$$

where $w(i) = d(i+1) - d(i)$. ESO is essentially a state observer for the augmented system in (4.18). If $w(i)$ is deterministic but unknown, a high-gain state observer can be designed. If $w(i)$ is process noise, Kalman filter can be designed. In both ways, ESO implies an assumption of the disturbance dynamics as follows

$$d(i+1) = d(i) + w(i) \tag{4.19}$$

That is, $d$ is assumed a constant plus the uncertainties $w$. This explains why ESO works well for slowly time-varying / low-frequency disturbances.

Motivated by the assumption (4.19) made by the standard ESO theory, more complex vibration dynamics can be introduced for vibration estimation beyond the Nyquist frequency. Assume $d$ is generated through certain dynamics which is driven by broadband noise $w$, i.e.,

$$\begin{aligned} x_d(i+1) &= A_d x_d(i) + B_d w(i) \\ d(i) &= C_d x_d(i) \end{aligned} \tag{4.20}$$

Combining (4.17) and (4.20), the augmented system becomes

$$\begin{aligned} \begin{bmatrix} x_p(i+1) \\ x_d(i+1) \end{bmatrix} &= \begin{bmatrix} A_p & B_p C_d \\ 0 & A_d \end{bmatrix} \begin{bmatrix} x_p(i) \\ x_d(i) \end{bmatrix} + \begin{bmatrix} B_p \\ 0 \end{bmatrix} u(i) + \begin{bmatrix} 0 \\ B_d \end{bmatrix} w(i) \\ y(j) &= \begin{bmatrix} C_p & 0 \end{bmatrix} \begin{bmatrix} x_p(j) \\ x_d(j) \end{bmatrix} + v(j) \\ d(i) &= C_d x_d(i) \end{aligned} \tag{4.21}$$

which is further written in a compact format

$$\begin{aligned} x(i+1) &= Ax(i) + Bu(i) + B_w w(i) \\ y(j) &= Cx(j) + v(j) \end{aligned} \tag{4.22}$$

where

$$\begin{aligned} A &= \begin{bmatrix} A_p & B_p C_d \\ 0 & A_d \end{bmatrix}, B = \begin{bmatrix} B_p \\ 0 \end{bmatrix}, B_w = \begin{bmatrix} 0 \\ B_d \end{bmatrix} \\ C &= \begin{bmatrix} C_p & 0 \end{bmatrix}, x = \begin{bmatrix} x_p^T & x_d^T \end{bmatrix}^T \end{aligned} \tag{4.23}$$

For single-rate systems, conventional Kalman filter [90] provides the best linear estimation for $x$ in the sense of mean square error (MSE) when $w$ and $v$ are zero-mean white noises. Considering that the augmented system (4.22) is a dual-rate system with slow measurement, multi-rate Kalman filter [102] is designed with two steps: (1) prediction between the sampling instants and (2) correction at the sampling instants.

Rewrite (4.22) with a unified time step $k$ ($k = 1, 2, 3...$) as follows

$$\begin{aligned} x(kN + c + 1) &= Ax(kN + c) + Bu(kN + c) + B_w w(kN + c) \\ y(kN) &= Cx(kN) + v(kN) \end{aligned} \tag{4.24}$$

where $c = 0, 1, ..., N - 1$; $w(kN + c)$ and $v(kN)$ are assumed to be zero-mean, Gaussian and white. The multi-rate system (4.24) can be lifted into a single-rate system ($T_s$) as follows

$$\begin{aligned} x(kN + N) &= A^N x(kN) + \sum_{c=0}^{N-1} A^{N-1-c} Bu(kN + c) + \sum_{c=0}^{N-1} A^{N-1-c} B_w w(kN + c) \\ y(kN) &= Cx(kN) + v(kN) \end{aligned} \tag{4.25}$$

Denote

$$\begin{aligned} A_e &= A^N, \\ u_e &= \sum_{c=0}^{N-1} A^{N-1-c} Bu(kN + c), \\ w_e &= \sum_{c=0}^{N-1} A^{N-1-c} B_w w(kN + c) \end{aligned} \tag{4.26}$$

Equation (4.25) can be rewritten in a more compact way

$$\begin{aligned} x(kN + N) &= A_e x(kN) + u_e + w_e \\ y(kN) &= Cx(kN) + v(kN) \end{aligned} \tag{4.27}$$

Denote $\hat{x}(i|j)$ as the estimate of $x(i)$ based on the measurement before and on time $jT_s$. The multi-rate Kalman filter for the system (4.24) is designed as follows.
(1) Prediction. There is no measurement available between the sampling instants; the best fast-rate estimate between the sampling instants comes from the prediction based on the open-loop dynamics (4.22) including the nominal vibration dynamics. Therefore, at the time instants $t{=}(Nk + m)T_f$ ($\forall m = 1, 2, .., N$),

$$\hat{x}(Nk + m|Nk) = A^m \hat{x}(Nk|Nk) + \sum_{c=0}^{m-1} A^{m-1-c} Bu(kN + c) \tag{4.28}$$

(2) Correction. At the time instants $t{=}N(k+1)T_f$, new measurement $y(Nk+N)$ is available; therefore

$$\hat{x}(Nk+N|Nk+N) = \hat{x}(Nk+N|Nk) + K(k+1)[y(Nk+N) - C\hat{x}(Nk+N|Nk)] \tag{4.29}$$

Noting the correction law in (4.29) is based on the lifted model described by (4.27), the process noise is $w_e$ instead of $w$. Therefore, $K$ is updated through the following equations:

$$\begin{aligned} K(k+1) &= M(k+1)C^T[CM(k+1)C^T + V]^{-1}; \\ M(k+1) &= A_e M(k) A_e^T + W_e - A_e M(k) C^T [CM(k)C^T + V]^{-1} CM(k) A_e^T \end{aligned} \tag{4.30}$$

where $V$ and $W_e$ are the covariances of the noise $v$ and $w_e$. That is, $V = Cov(v)$ and

$$\begin{aligned} W_e =& Cov(\sum_{c=0}^{N-1} A^{N-1-c} B_w w(kN+c)) \\ &= E\{[\sum_{c=0}^{N-1} A^{N-1-c} B_w w(kN+c)][\sum_{c=0}^{N-1} A^{N-1-c} B_w w(kN+c)]^T\} \\ &= (\sum_{c=0}^{N-1} A^{N-1-c} B_w) W (\sum_{c=0}^{N-1} A^{N-1-c} B_w)^T \end{aligned} \tag{4.31}$$

where $W{=}Cov(w)$ and $E\{\cdot\}$ denotes the expectation. Based on (4.21), the vibration estimate is

$$\hat{d} = C_d \hat{x}_d \tag{4.32}$$

It is worth remarking that, usually $\hat{d}$ is filtered by certain filter before it is added back to the feedback loop to compensate the actual disturbances. Such filter can be a low/high/band-pass filter or phase compensator to recover some phase loss or amplitude mismatch over certain frequency ranges as discussed in [89].

In sum, by incorporating the nominal dynamics of the vibrations, this section has presented the design of a multi-rate extended estimator based on the augmented system. The estimated PES and vibrations between the sampling instants enable fast updating of the control signal.

## Simulation Validation

The simulation is performed on the single-stage HDD Benchmark system described in Chapter 1. The Nyquist frequency is 13200Hz. There exists one major resonance beyond the Nyquist frequency. The disturbance file used in this simulation is provided in Figure 4.5, in which the top figure is the frequency response of the nominal dynamics, and the bottom figure is the spectrum of the actual injected disturbance.

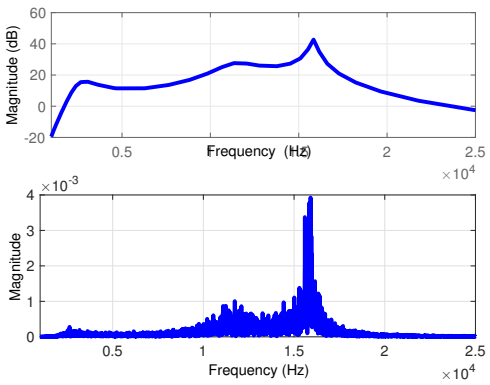


Figure 4.5: Disturbance file

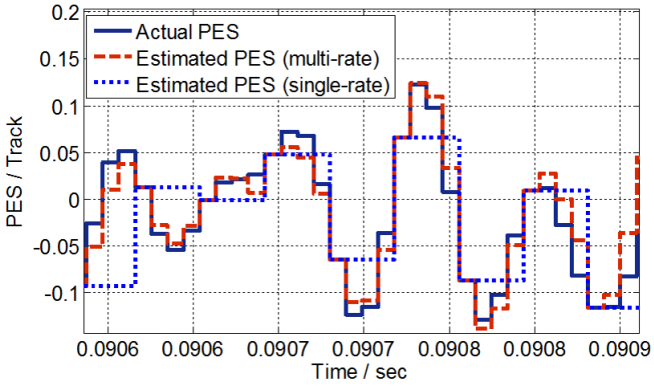


Figure 4.6: PES estimates

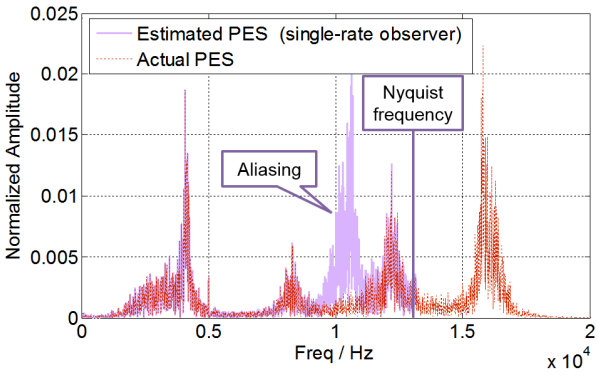


(a) Single-rate observer

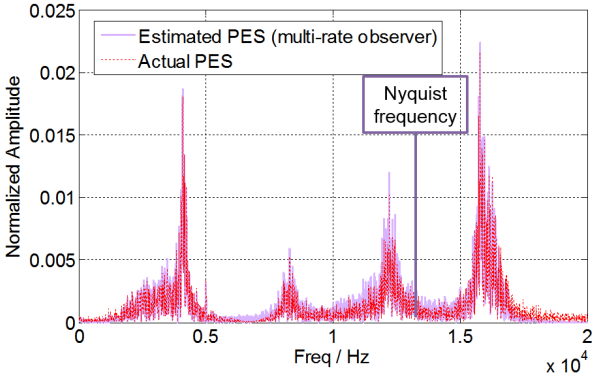


(b) Multi-rate observer

Figure 4.7: PES spectrum estimate

Figure 4.6 compares the actual PES and estimated PES in time domain. Due to the vibration components beyond the Nyquist frequency, the estimated PES based on the single-rate observer misses some off-track behaviors of the actual PES (for example, within the period from 0.0907 sec to 0.0908 sec). Instead, the multi-rate observer is able to capture most of the PES's behaviors. Figure 4.7a compares the spectrum of the actual PES and the estimated PES through the single-rate observer, in which the aliasing effect shows up. Figure 4.7b compares the spectrums of the actual PES and the estimated PES through the multi-rate observer, in which even the PES beyond the Nyquist frequency is reconstructed by the multi-rate observer. In sum, by incorporating the disturbance dynamics and the design of the multi-rate extended observer, the estimation bandwidth has been pushed beyond the Nyquist frequency.

## 4.4 Chapter Summary

This chapter has explored the algorithms of pushing the bandwidth of the ESO to higher frequency ranges based on a phase compensator and a priorly known nominal disturbance dynamics. For the former one, the phase compensator recovers the phase loss in the standard ESO; such compensated ESO provides more accurate estimates for both the states and the disturbances at high frequencies. For the latter one, a multi-rate observer has been proposed to incorporate the nominal dynamics of the vibrations and is able to estimate both the state and the vibrations beyond the Nyquist frequency; large off-track behaviors of the VCM have been effectively captured. The simulation study performed on the HDD Benchmark model has been provided to validate these benefits.

# Chapter 5

# Frequency-shaped Sliding Mode Control Based on Root Locus

## 5.1 Introduction

Discrete-time sliding mode control (SMC) is a powerful nonlinear technique that has been comprehensively studied in the existing literature. Various SMCs have been proposed to enhance system performances: disturbance observer (DOB) based SMC [103] to increase the robustness to external disturbances, robust terminal SMC [104] to overcome the singularity problem and gain faster convergence. These SMC algorithms have been applied to various mechanical systems including quadrotors [105], active suspension vehicle systems [106], manipulators [107] and spherical mobile robots [108]. Comprehensive reviews on recent improvements and new perspectives of SMC have been provided in [109–111].

SMC has been applied to hard disk drives (HDDs) due to its fast convergence and good robustness to unknown disturbances in the past few years. A SMC algorithm was applied to HDDs to achieve a fast track-seeking performance in [51]. A time-optimal SMC algorithm with a time-varying sliding surface was proposed in [52] for the smooth transition from the track-seeking process to the track-following process, which was further improved to reduce the setting time during the track-seeking process in [53]. Another sliding mode control for HDDs was also proposed based on a time-optimal sliding surface to improve both the transient performance and the steady-state performance [54]. SMC has been considered as a promising technique with excellent transient performance in HDDs.

Aiming to extend the design of sliding mode control from time domain to frequency domain, motivated by the frequency-shaped linear quadratic regulator (LQR), a frequency-shaped sliding mode control (FSSMC) with a new switching plane was proposed and applied it to a flexible robot manipulator in [112]. Many researchers then extended, improved and applied FSSMC to different areas. A FSSMC based on the robust control theory was designed for a flexible arm in [113]. A conventional sliding surface that can be made equivalent to the frequency-shaped one was provided and applied to a single degree of freedom robot with a flexible appendage in [114] . A low-pass filter was added to the control input to suppress chatter in SMC in [115]. The design of the frequency-shaped sliding surface based on LQR weighting functions was discussed in [116]. A FSSMC with

an inverse notch filter was designed to control the flying height of the pickup head in optical disk dives in [117]. A FSSMC based on the output sampled measurements was designed to damp the vibration amplitude of a smart beam at its resonance frequencies in [118].

In most of the aforementioned literature, FSSMC is motivated by the frequency-shaped LQR control problem with frequency-varying weighting functions, aiming to attenuate the excitation of undesired system dynamics and enhance the robustness. This chapter proposes an alternative FSSMC with intuitive design guidelines; the proposed FSSMC is motivated by direct enhancement at the frequencies where the performance is degraded by large peaks in the vibrations. Specifically, to have customized control allocation for attenuating large peaks in the vibrations, the proposed FSSMC increases the 'local gain' of SMC at these peak frequencies. Peak filters are utilized to increase the local gain. Analysis based on root locus is provided for intuitive design and easy stability analysis. Control algorithms and shaping filters are designed in the discrete time domain. This makes analysis more complex than the continuous-time domain, but the design algorithms and filters are directly implementable on actual HDDs.

## 5.2 Frequency-shaped SMC

A continuous-time nominal model that captures the central low-frequency characters of HDDs is

$$\begin{bmatrix} \dot{y} \\ k_y \dot{v} \end{bmatrix} = \begin{bmatrix} k_y v \\ k_y k_v u \end{bmatrix} \tag{5.1}$$

where $u$ is the control signal, $y$ is the position of the head in the unit of tracks, $v$ is the velocity, $k_v$ is the acceleration constant, and $k_y$ is the position measurement gain.

Denote $e_1 = y - y_r$, and $e_2 = \dot{e}_1 = k_y v - \dot{y}_r$. In HDD track-following control, $y_r$ and $\dot{y}_r$ are set as zero. From (5.1), the discrete-time error dynamics with unknown bounded disturbances is

$$e(k+1) = Ae(k) + B(u(k) + d(k)) \tag{5.2}$$

where

$$e(k) = \begin{bmatrix} e_1(k) \\ e_2(k) \end{bmatrix}, A = \begin{bmatrix} 1 & T_s \\ 0 & 1 \end{bmatrix}, B = \begin{bmatrix} T_s^2 k_y k_v / 2 \\ T_s k_y k_v \end{bmatrix},$$

$T_s$ is the sampling time, and $|d| \leq D$ is the input disturbances.

In this section, a FSSMC algorithm is proposed to provide enhancements at the frequencies where the servo performance is seriously degraded by large disturbances. A peak filter $Q_f$ is introduced to shape sliding surface at the preferred frequencies. $Q_f$ can be regarded as a weighting function to allocate the control effort in the frequency domain: it is expected that the controller allocates more energy at the frequencies where the weight is large. Here, the peaks of $Q_f$ are selected at the frequencies where PES is large.

Based on this idea, we have a different definition for the sliding surface in FSSMC as shown in Figure 5.1. In the traditional definition of sliding surface $s_t(k) = 0$, $s_t(k)$ is defined as $s_t(k) = He(k) = \begin{bmatrix} 1 & h_2 \end{bmatrix} e(k)$ $(h_2 > 0)$. In the frequency-shaped sliding surface $s(k) = 0$, $s(k)$ is modified to

$$s(k) = H \begin{bmatrix} Q_f\{e_1(k)\} \\ e_2(k) \end{bmatrix} = e_f(k) + h_2 e_2(k) \tag{5.3}$$

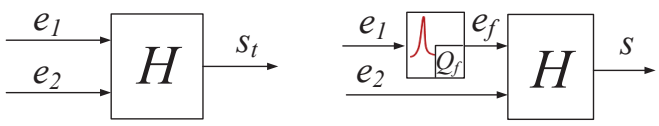


(a) Traditional Sliding Surface Definition

(b) Frequency-shaped Sliding Surface Definition

Figure 5.1: Sliding surface definition

where $e_f$ is the filtered position error, i.e., $e_f = Q_f\{e_1\}$. Assume that $Q_f$ has the following state-space realization:

$$\begin{aligned} e_w(k+1) &= A_w e_w(k) + B_w e_1(k) \\ Q_f\{e_1(k)\} &= C_w e_w(k) + D_w e_1(k) \end{aligned} \tag{5.4}$$

Combining (5.2) and (5.4), the augmented system can be represented as

$$\tilde{E}(k+1) = \tilde{A}\tilde{E}(k) + \tilde{B}(u(k) + d(k)) \tag{5.5}$$

where

$$\tilde{E}(k) = (e_w^T(k),\ e^T(k))^T \tag{5.6}$$

$$\tilde{A}(k) = \begin{bmatrix} A_w & B_w & 0 \\ 0 & A_{11} & A_{12} \\ 0 & A_{21} & A_{22} \end{bmatrix},\ \tilde{B}(k) = \begin{bmatrix} 0 \\ B_1 \\ B_2 \end{bmatrix} \tag{5.7}$$

The FSSMC control law is proposed as

$$u(k) = (\tilde{H}\tilde{B})^{-1}[(1 - qT_s)s(k) - \tilde{H}\tilde{A}\tilde{E}(k) - (\varepsilon T_s + \beta)\, sgn(s(k))] \tag{5.8}$$

where $\beta = \tilde{H}\tilde{B}D$, $\tilde{H} = [C_w\ D_w\ h_2]$, $q > 0$, $1 - qT_s > 0$, and $0 \lessapprox \varepsilon < 1$. Substituting (5.8) into (5.2), after some algebra, the approaching dynamics of the system becomes

$$s(k+1) = (1 - qT_s)s(k) - (\varepsilon T_s + \gamma(k))sgn(s(k)) \tag{5.9}$$

where

$$\gamma(k) = \beta - \tilde{H}\tilde{B}d(k)sgn(s(k)) \tag{5.10}$$

with $0 \leq \gamma(k) \leq 2\beta = \gamma$.

## 5.3 Stability Analysis

Two conditions have to be satisfied to ensure the stability of SMC systems: (a) approaching condition: the trajectory $s(k)$, starting from any initial point, reaches to the sliding surface $s(k) = 0$ in finite time; and (b) sliding condition: after the trajectory reaches the sliding surface, it stays on it. This means that the sliding surface $s(k) = 0$ should define stable dynamics for $\tilde{E}(k)$, which ensures the boundedness of the tracking error $e_1(k)$ and $e_2(k)$ when $s(k)$ is bounded. The overall stability analysis for System (5.2) with the controller (5.8) includes both the approaching phase and the sliding phase.

## Approaching Phase

This part shows that the sliding surface $s(k) = 0$ will be reached in finite time if the approaching dynamics satisfies (5.9). [88] proposed several conditions for a general class of discrete-time approaching dynamics: (a) starting from any initial point, the trajectory will move monotonically toward the switching plane and cross it in finite time; (b) once the trajectory has crossed the switching plane for the first time, it will cross the plane again in every successive sampling period, resulting in a zigzag motion about the switching plane; and (c) the trajectory stays in a band.

In the following, we prove that under Equation (5.9), conditions (a)-(c) are satisfied. That is, $s(k)$ will converge to and stay in the band $[-\Delta,\ \Delta]$, where

$$\Delta = \frac{\varepsilon T_s + \gamma}{1 - qT_s} \geq \frac{\varepsilon T_s + \gamma(k)}{1 - qT_s} = \Delta(k) > 0 \tag{5.11}$$

From Equation (5.9), we have

$$\begin{aligned} s(k+1) &= (1 - qT_s)|s(k)|sgn(s(k)) - (\varepsilon T_s + \gamma(k))sgn(s(k)) \\ &= (|s(k)| - \Delta(k))(1 - qT_s)sgn(s(k)) \end{aligned}$$

When $|s(k)| > \Delta(k)$, $\text{sgn}(s(k+1)) = \text{sgn}(s(k))$ and $|s(k+1)| = (|s(k)| - \Delta(k))(1 - qT_s) < |s(k)|$, which implies that $s(k)$ would move towards the band monotonically; similarly, when $|s(k)| < \Delta(k)$, $\text{sgn}(s(k+1)) = -\text{sgn}(s(k))$ and $|s(k+1)| = (\Delta(k) - |s(k)|)(1 - qT_s) < \Delta(k)$, which implies that $s(k)$ will go across the switching plane, change its sign at every step and stay in the band thereafter.

In summary, the controller (5.8) can drive the system (5.2) towards the sliding surface $s(k) = 0$ with the approaching dynamics (5.9) in finite time, and make it stay in the band $[-\Delta,\ \Delta]$ centered around the sliding surface thereafter. In practical implementation, the discontinuous function sgn is usually replaced by a saturation function to inhibit the chatter phenomenon.

## Sliding Phase

To guarantee the stability of the overall system, the convergence of $s(k)$ is not sufficient. In this section, we derive conditions for both $e_1(k)$ and $e_2(k)$ to converge to zero when $s(k)$ converges to zero. First consider the continuous-time sliding surface $s = 0$, where

$$s = e_f + h_2 e_2 = Q_f\{e_1\} + h_2 \dot{e}_1 \tag{5.12}$$

Assume that $Q_f$ has the transfer function realization: $Q_f(p) = B(p)/A(p)$, where $p$ is the Laplace variable. Then, the dynamics between $s$ and $e_1$ is

$$e_1 = \frac{1}{\frac{B(p)}{A(p)} + h_2 p} s \tag{5.13}$$

which can be realized by the block diagram in Figure 5.2.

Notice that the open-loop transfer function from $s$ to $e_1$ in Figure 5.2 is

$$G(p) = \frac{1}{h_2} \frac{B(p)}{A(p)} \frac{1}{p} \tag{5.14}$$

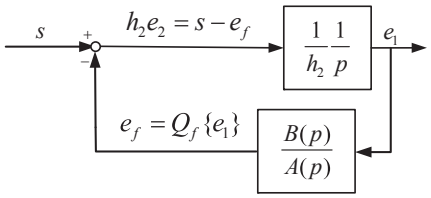


Figure 5.2: Dynamics of sliding surface

and the closed-loop characteristic equation is

$$1 + \frac{1}{h_2}\frac{B(p)}{A(p)}\frac{1}{p} = 0 \tag{5.15}$$

Given a $h_2 > 0$, if all of the closed-loop poles are in the left half plane, the systems from $s$ to $e_1$ and from $s$ to $e_2$ are stable; thus any bounded $s$ yields bounded $e_1$ and bounded $e_2$. We have thus transformed the stability analysis (in sliding phase) into a root-locus problem: as $1/h_2$ changes from 0 to $+\infty$, the poles of System (5.13) are on the root loci from the open-loop poles to the open-loop zeros and $-\infty$, and would never go into the right half plane.

For the discrete-time case, 5.12 is replaced by

$$s(k) = e_f(k) + h_2e_2(k) = Q_f\{e_1(k)\} + h_2\frac{2}{T_s}\frac{z-1}{z+1}e_1(k) \tag{5.16}$$

where $Q_f$ has the transfer function realization $Q_f(z) = B_d(z)/A_d(z)$, and the discretized version of $Q_f(p)$ via Tustin transformation:

$$p = \frac{2}{T_s}\frac{z-1}{z+1} \tag{5.17}$$

Then the discrete-time dynamics between $s(k)$ and $e_1(k)$ is

$$e_1(k) = \frac{1}{\frac{B_d(z)}{A_d(z)} + h_2\frac{2}{T_s}\frac{z-1}{z+1}}s(k) \tag{5.18}$$

and the closed-loop characteristic equation is

$$1 + \frac{1}{h_2}\frac{T_s}{2}\frac{z+1}{z-1}\frac{B_d(z)}{A_d(z)} = 0 \tag{5.19}$$

A root locus analysis similar to the continuous-time case can be performed. Alternatively, noticing that the Tustin transformation preserves stability of the poles and zeros by the mapping (5.17) (where the left-half plane is mapped to the inside of the unit cycle), we can directly conclude that (5.18) is stable if and only if its continuous-time equivalent system (5.13) is stable.

## 5.4 Filter Design

This section discusses the design of the peak filters for FSSMC.

## Peak Filter with Single Peak (PFSP)

A continuous-time PFSP is

$$Q_f(p) = \frac{B(p)}{A(p)} = \frac{p^2 + 2bw_d p + w_d^2}{p^2 + 2aw_d p + w_d^2} \tag{5.20}$$

with $0<a<b<1$. The following shows if $h_2>0$, the closed-loop poles of the system (5.13) with (5.20) remain stable; namely, FSSMC has a guaranteed stable sliding surface.

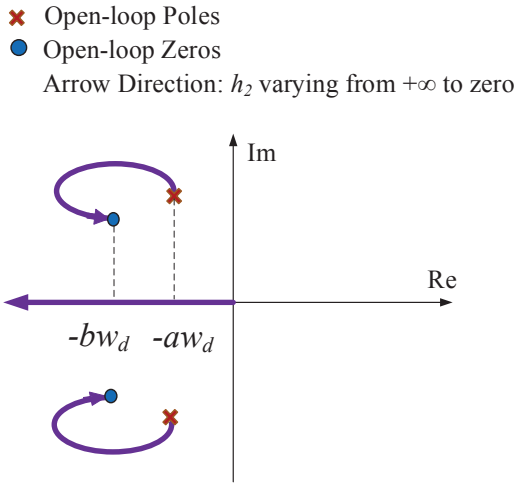


Figure 5.3: Root locus with a PFSP

Figure 5.3 shows that the root loci of the closed-loop system (5.13) with (5.20) as $h_2$ changes from $+\infty$ to zero, which are always in the left half plane. More specifically, if both the open-loop poles and zeros are in the stable region, a closed-loop pole can never be on the imaginary axis (except the one at origin), or the root loci never enters the unstable region. To prove this, suppose there exits a pole at $p = \gamma j (\gamma \neq 0)$. It must satisfy

$$1 + \frac{1}{h_2}\frac{B(\gamma j)}{A(\gamma j)}\frac{1}{\gamma j} = 0 \tag{5.21}$$

Using (5.20), we have

$$\angle \frac{(w_d^2 - \gamma^2) + 2bw_d\gamma j}{(w_d^2 - \gamma^2) + 2aw_d\gamma j}\frac{1}{\gamma j} = (2n+1)\pi \tag{5.22}$$

or

$$\arctan\left(\frac{\frac{2bw_d\gamma}{w_d^2-\gamma^2} - \frac{2aw_d\gamma}{w_d^2-\gamma^2}}{1 + \frac{2bw_d\gamma}{w_d^2-\gamma^2}\frac{2aw_d\gamma}{w_d^2-\gamma^2}}\right) = -\frac{\pi}{2} \tag{5.23}$$

This means $\left(1 + \frac{2bw_d\gamma}{w_d^2-\gamma^2}\frac{2aw_d\gamma}{w_d^2-\gamma^2}\right)$ has to be 0, which is impossible. Therefore, the root loci never cross the imaginary axis

Actually, in the single peak filter case, the sliding surface is a 3rd-order system, and the stability can be directly checked. Combining (5.13) and (5.20), we have

$$e = \left[\frac{p^2 + 2aw_d p + w_d^2}{h_2 p^3 + (1 + 2aw_d h_2)p^2 + (h_2 w_d^2 + 2bw_d)p + w_d^2}\right] s \tag{5.24}$$

The closed-loop poles satisfy

$$h_2 p^3 + (1 + 2aw_d h_2)p^2 + (h_2 w_d^2 + 2bw_d)p + w_d^2 = 0 \tag{5.25}$$

Note that the coefficients $h_2 > 0$, $(1 + 2aw_d h_2) > 0$, $(h_2 w_d^2 + 2bw_d) > 0$, $w_d^2 > 0$. From Routh test, the system is stable if and only if $(1 + 2aw_d h_2)(h_2 w_d^2 + 2bw_d) - h_2 w_d^2 > 0$, which clearly holds as $(1 + 2aw_d h_2) > 1$ and $(h_2 w_d^2 + 2bw_d) > h_2 w_d^2$.

In summary, we obtain a conclusion on the stability of the proposed FSSMC with a PFSP: as long as both the zeros and poles of (5.20) are stable, the sliding surface is guaranteed to be stable.

The corresponding discrete-time version of (5.20) based on Tustin transformation is

$$Q_f(z) = \frac{B_d(z)}{A_d(z)} \tag{5.26}$$

where $B_d(z) = 4(z-1)^2 + 4T_s bw_d(z-1)(z+1) + T_s^2 w_d^2 (z+1)^2$, $A_d(z) = 4(z-1)^2 + 4T_s aw_d(z-1)(z+1) + T_s^2 w_d^2 (z+1)^2$. With such a filter, the discrete-time sliding surface (5.16) is stable if and only if both the zeros and poles of the corresponding continuous-time filter (5.20) are stable.

## Peak Filter with Multi-peaks (PFMP)

Usually there are more than one peaks at $\omega_{di}$'s $(i = 1, 2, ..., N)$ in the external vibrations. Such cases can be handled by FSSMC with a PFMP

$$Q_f(p) = \prod_{i=1}^{N} \frac{B_i(p)}{A_i(p)} \tag{5.27}$$

where $B_i(p) = p^2 + 2bw_{di}p + w_{di}^2$, and $A_i(p) = p^2 + 2aw_{di}p + w_{di}^2$. Analogous to previous discussion, a general dynamics between $s$ and $e_1$ with a PFMP can be represented as

$$e_1 = \frac{1}{\prod_{i=1}^{N} \frac{B_i(p)}{A_i(p)} + h_2 p} s \tag{5.28}$$

and the closed-loop characteristic equation is

$$1 + \frac{1}{h_2} \prod_{i=1}^{N} \frac{B_i(p)}{A_i(p)} \frac{1}{p} = 0 \tag{5.29}$$

Although all the open-loop zeros and poles (except the one at origin) are in the left half plane, the closed-loop root loci may cross the imaginary axes. In this case, the proposed root locus method provides an intuitive way to decide the filter parameters $a$, $b$, and the sliding surface

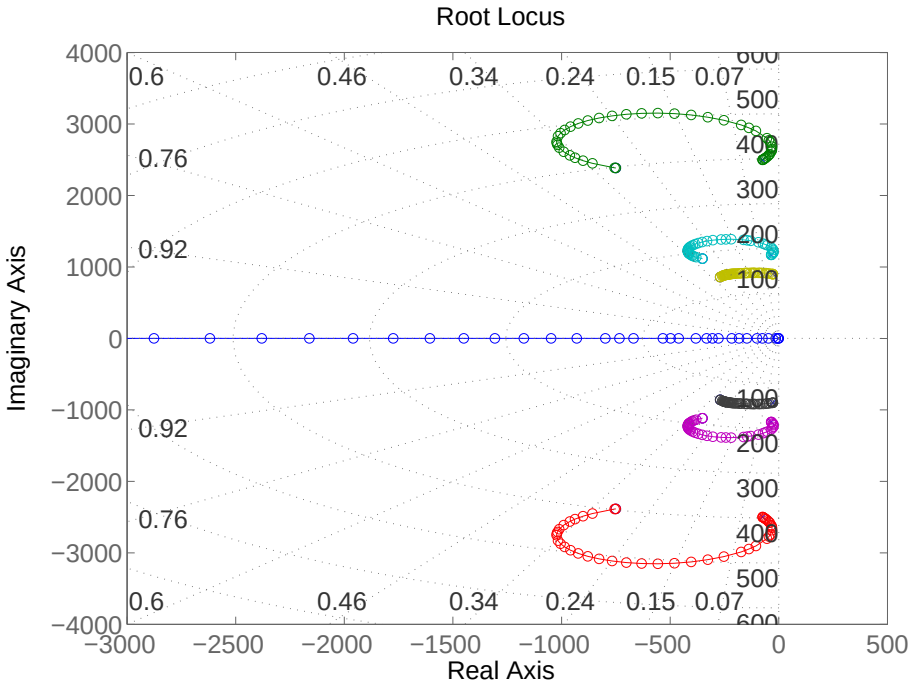


Figure 5.4: Root locus with a PFMP

parameter $h_2$ in the $p$ plane. For example, if we would like to design a three-peak filter with $n = 3, a = 0.03, b = 3, w_1 = 900\text{Hz}, w_2 = 1170\text{Hz}, w_3 = 2500\text{Hz}$, the root locus can be numerically calculated and plotted, as shown in Figure 5.4. For this particular design, FSSMC can stabilize the system when $h_2 > 0$. The sliding surface can be further refined by selecting a suitable $h_2$ based on the transient performance.

For implementation, the equivalent discretized $Q_f$ (by Tustin Transform) is

$$Q_f(z) = \prod_{i=1}^{N} \frac{B_{di}(z)}{A_{di}(z)} \tag{5.30}$$

where $B_{di}(z) = 4(z-1)^2+4T_s b w_{di}(z-1)(z+1)+T_s^2 w_{di}^2(z+1)^2$, and $A_{di}(z) = 4(z-1)^2+4T_s a w_{di}(z-1)(z+1) + T_s^2 w_{di}^2(z+1)^2$. The discrete dynamics between $s(k)$ and $e_1(k)$ is described as

$$e_1 = \frac{1}{\prod_{i=1}^{N} \frac{B_{di}(z)}{A_{di}(z)} + h_2 \frac{2}{T_s}\frac{z-1}{z+1}} s \tag{5.31}$$

with the closed-loop characteristics equation

$$1 + \frac{1}{h_2}\frac{T_s}{2}\frac{z+1}{z-1}\prod_{i=1}^{N}\frac{B_{di}(z)}{A_{di}(z)} = 0 \tag{5.32}$$

(5.31) is stable if and only if (5.28) is stable.

In most cases, it is not known in advance at which frequencies the servo performance is most degraded. Such frequency ranges may be identified in real time through processing the error signal $e_1(k)$ by an adaptive notch filter with an adjustable notch frequencies. Related work will be presented in Chapter 7.

## 5.5 Simulation Validation

The proposed FSSMC is implemented on the single-stage HDD Benchmark system. For the implementation on the dual-stage HDDs, please see [119]. In this simulation study, the system is injected with three sets of audio vibrations with peak frequencies around 1200Hz, 900Hz, 2500Hz respectively. Two control algorithms are compared: the traditional SMC, and the proposed FSSMC.

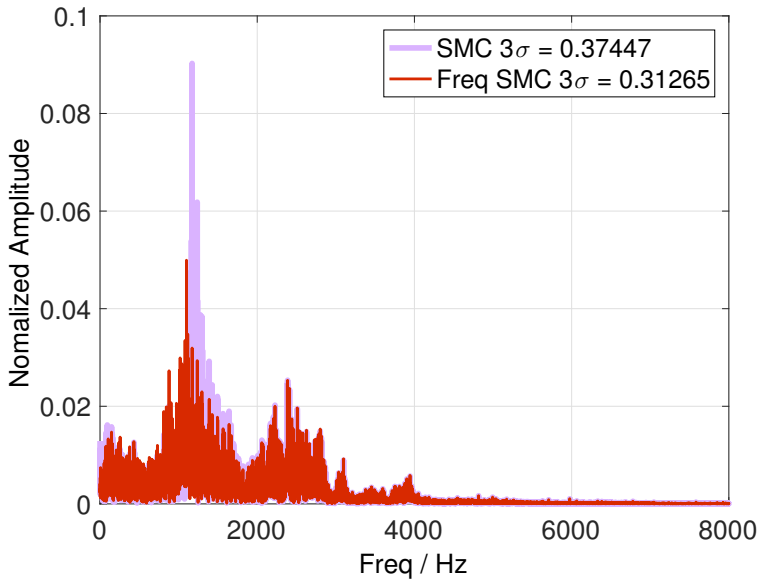


Figure 5.5: PES spectrum with audio vibration 1

Figures 5.5 to 5.7 show the spectrums of PES with three sets of audio vibrations. The accumulative $3\sigma$ value of PES is calculated and shown at the top right corn of each figure. As shown in Figure 5.5, the accumulative $3\sigma$ value of PES has been reduced from 0.37447 to 0.31265 by frequency shaping, approximate 20% reduction; the amplitude reduction around the peak frequency is approximate 50%. Similar results for the other two sets of audio vibrations are shown in Figure 5.6 (approximate 26% reduction of accumulative $3\sigma$ value of PES and 50% amplitude reduction around the peak frequency) and Figure 5.7 (approximate 13% reduction of accumulative $3\sigma$ value of PES and more than 50% amplitude reduction around the peak frequency). Figure 5.8 provides the calculated frequency responses of the sensitivities when the third set of vibrations is injected.

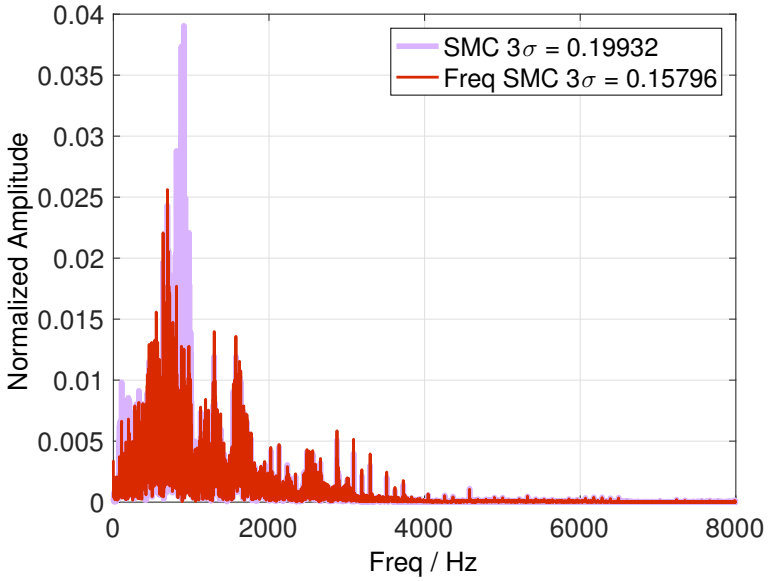


Figure 5.6: PES spectrum with audio vibration 2

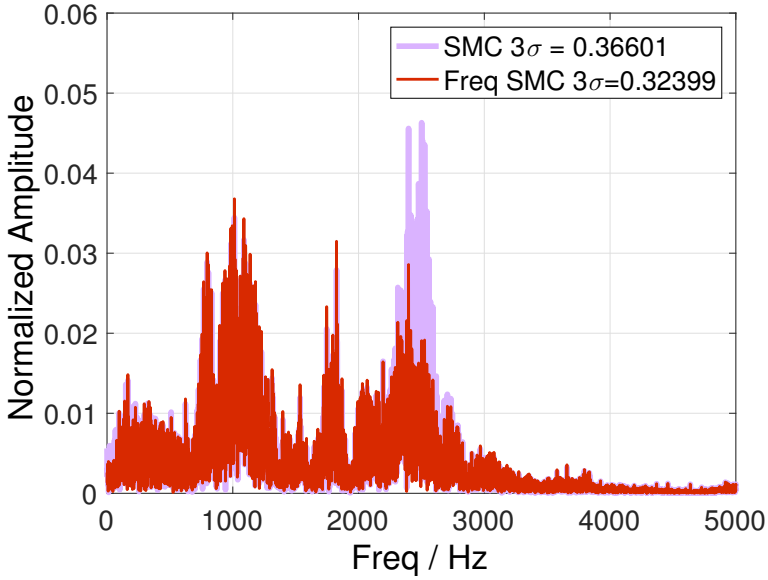


Figure 5.7: PES spectrum with audio vibration 3

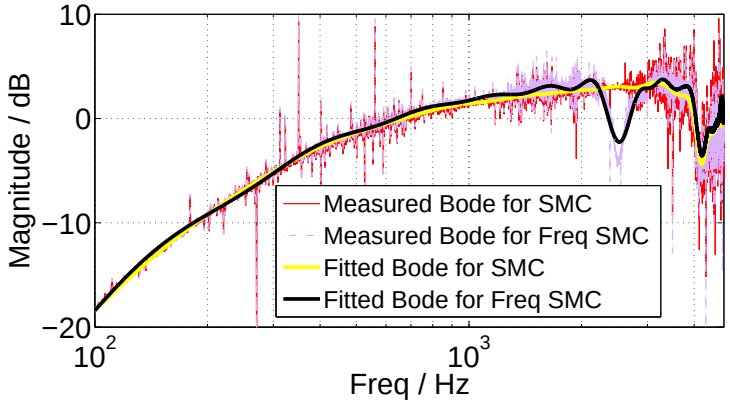


Figure 5.8: Measured frequency responses from vibration 3 to PES

Simulation results demonstrate the benefits of the proposed FSSMC: reduction of the overall $3\sigma$ value of PES, and reduction of the amplitude of the PES spectrum at specific frequencies, with very small performance sacrifice at other frequencies.

## 5.6 Chapter Summary

This chapter has proposed a FSSMC algorithm based on the root locus technique to suppress high-frequency peaks in the vibrations. Simulation results have validated the benefits of the proposed FSSMC. From the theoretical viewpoint, this work provides comprehensive stability analysis and a guideline for the filter design based on root-locus method, which provides great flexibility and convenience in the frequency-domain controller design. A nice property of the proposed PFSP design is that: as long as both the poles and the zeros of the shaping filter are stable, the sliding surface is stable. This work can also be extended to a general case to address multiple peaks in the vibrations. The peak frequencies of the shaping filters are assumed known, which otherwise can be adaptively tuned based on online identification of large peaks in the vibrations.

# Chapter 6

# Frequency-shaped Sliding Mode Control Based on H-infinity Synthesis

## 6.1 Introduction

Due to fast convergence and nice robustness to external disturbances, sliding mode control (SMC) becomes an effective technique in high-precision systems in recent years [120, 121]. For example, in hard disk drives (HDDs), several kinds of SMCs have been proposed to improve the transient performance when the track seeking is switched to the track following [51–54]. However, theses SMCs were designed and analyzed in time domain without considering the frequency-response characteristics of the closed-loop systems, which are critically important for high-precision systems that are subjected to narrow band disturbances such as high-frequency vibrations. Therefore, it makes significant sense to explicitly consider frequency-domain performances of the closed-loop systems when designing SMC, which is rather challenging due to the nonlinearity of SMC.

To extend the SMC design from time domain to frequency domain, frequency-shaped sliding mode control (FSSMC) has been proposed and applied to different mechanical systems, such as flexible robot manipulators [112, 114, 116], electrohydraulic servo-motors [115], pickup heads in optical disk dives [117], and smart beams with resonances [118]. However, in most of the aforementioned literature, FSSMC was designed based on the frequency-shaped linear-quadratic regulator (LQR). Furthermore, these shaping approaches were not generalized into a systematic methodology and the stability of the sliding surface was usually difficult to guarantee. Chapter 5 proposed a FSSMC with intuitive design guidelines motivated by the root locus technique, which is easy to implement and guarantee the stability when there is only one peak frequency in the shaping filter.

This chapter makes one more step towards the frequency-domain design methodology for SMC, and presents a systematic framework to design the sliding surface in frequency domain based on the loop-shaping technique and the $H_\infty$ synthesis [122]. Similar to the work of [123] and [113], the proposed deign procedure also involves $H_\infty$ synthesis. The difference is that the algorithm presented here treats the shaping filter as an inner loop feedback controller, and augments the dynamics of the sliding surface into a feedback system. With this idea, the stability of the sliding surface can be guaranteed in the presence of disturbances. Furthermore, the shaping filter minimizes the weighted $H_\infty$-norm of the sliding dynamics and thus minimizes performance degradation at $w_{di}$'s, where

$w_{di}$'s $(i = 1, 2, ..., N)$ denote these frequencies where the servo performance is seriously degraded by large disturbances. Both the sliding mode control algorithm and the shaping filter are designed in discrete-time, and thus can be readily implemented on actual mechanical systems. Furthermore, this chapter presents an explicit sub-optimal solution to avoid on-line optimization when $w_d$'s change according to different disturbance sources.

## 6.2 Frequency-domain Analysis of Discrete-time SMC

This section provides a general SMC and the analysis in frequency domain. Consider a controllable single-input-single-output (SISO) plant described by

$$\begin{aligned} e(k+1) &= A_p e(k) + B_p(u(k) + d(k)) \\ y(k) &= C_p e(k) \end{aligned} \tag{6.1}$$

where

$$e(k) = \begin{bmatrix} e_1(k) \\ e_2(k) \end{bmatrix} \in \begin{bmatrix} \mathbb{R}^{(n-1)\times 1} \\ \mathbb{R}^{1\times 1} \end{bmatrix} \tag{6.2}$$

$$\begin{aligned} A_p &= \begin{bmatrix} A_{11} & A_{12} \\ A_{21} & A_{22} \end{bmatrix} \in \begin{bmatrix} \mathbb{R}^{(n-1)\times(n-1)} & \mathbb{R}^{(n-1)\times 1} \\ \mathbb{R}^{1\times(n-1)} & \mathbb{R}^{1\times 1} \end{bmatrix} \\ B_p &= \begin{bmatrix} 0 \\ b_n \end{bmatrix} \in \begin{bmatrix} \mathbb{R}^{(n-1)\times 1} \\ \mathbb{R}^{1\times 1} \end{bmatrix} \\ C_p &= \begin{bmatrix} c_1 & c_2 \end{bmatrix} \in \begin{bmatrix} \mathbb{R}^{1\times(n-1)} & \mathbb{R}^{1\times 1} \end{bmatrix} \end{aligned} \tag{6.3}$$

$b_n \neq 0$; $y(k)$ is the position error signal (PES); $e(k)$ is the error signal; $u(k)$ is the control input to be designed; $d(k)$ is the disturbance bounded by $D$, i.e., $|d(k)| \leq D$.

It is worth noting that the controllability of $[A_p,\ B_p]$ implies the controllability of $[A_{11}, A_{12}]$. This is an important property when designing sliding mode control. Brief explanation base on Popov-Belovich-Hautus (PBH) test [124] is provided as follows. The controllability of $[A_p,\ B_p]$ implies

$$\begin{aligned} &\text{rank}(\begin{bmatrix} \rho I_n - A_p & B_p \end{bmatrix}) \\ &= \text{rank}(\begin{bmatrix} \rho I_{n-1} - A_{11} & -A_{12} & 0 \\ -A_{21} & \rho - A_{22} & b_n \end{bmatrix}) = n \end{aligned} \tag{6.4}$$

for all $\rho \in \mathbb{C}$, which further implies

$$\text{rank}(\begin{bmatrix} \rho I_{n-1} - A_{11} & -A_{12} \end{bmatrix}) = n - 1 \tag{6.5}$$

for all $\rho \in \mathbb{C}$. Therefore, $[A_{11},\ A_{12}]$ is controllable.

In traditional discrete-time sliding mode control, the sliding surface is usually defined as $s(k) = 0$ [88, 125], where

$$\begin{aligned} s(k) &= He(k) \\ &= \begin{bmatrix} h_1, & h_2, & , \cdots, & h_{n-1}, & 1 \end{bmatrix} e(k) \\ &= \tilde{h} e_1(k) + e_2(k) \end{aligned} \tag{6.6}$$

with $\tilde{h} = \begin{bmatrix} h_1, & h_2, & , \cdots, & h_{n-1} \end{bmatrix}$. The control law must be designed so that the following two conditions are satisfied to guarantee the stability of System (6.1) under control: (a) Approaching condition: the trajectory $s(k)$, starting from any initial point, enters in a vicinity (e.g. $\pm\delta$ band) of the surface $s(k) = 0$ in finite time steps and stays in the bound thereafter; (b) Sliding condition: in the vicinity of $s(k) = 0$, $e(k)$ remains bounded and exhibits stable dynamics.

Condition (a) can be guaranteed by appropriate approaching laws [88, 126, 127]

$$s(k+1) - s(k) = -qT_s s(k) - \epsilon T_s \text{sgn}(s(k)) \tag{6.7}$$

with $\epsilon > 0$, $q > 0$, and $1 - qT_s > 0$, where $T_s$ is the sampling time. This approaching law drives the trajectory $s(k)$ towards the sliding surface and results in a zigzag motion along the sliding surface with bounded amplitude [88]. There also exits several other kinds of approaching laws to guarantee $s(k)$ stay in the vicinity of the sliding surface [128, 129].

Condition (b) can be guaranteed by a stable sliding surface. From Equation (6.6), $e_2(k) = s - \tilde{h}e_1(k)$. From Equations (6.1) to (6.3),

$$\begin{aligned} e_1(k+1) &= A_{11}e_1(k) + A_{12}e_2(k) \\ &= (A_{11} - A_{12}\tilde{h})e_1(k) + A_{12}s(k) \end{aligned} \tag{6.8}$$

where $\tilde{h}$ is designed to guarantee $(A_{11} - A_{12}\tilde{h})$ is Schur (i.e., all the eigenvalues of $(A_{11} - A_{12}\tilde{h})$ are inside the unit circle on the complex plane). The controllability of $(A_{11},\ A_{12})$ guarantees the existence of such a $\tilde{h}$. After the trajectory is restricted within the vicinity the sliding surface (i.e., $s(k)$ is small and bounded), $e_1(k)$ and $e_2(k)$ stay bounded.

In the following, the sliding surface dynamics in traditional SMC is newly analyzed in frequency domain, based on which a FSSMC algorithm is proposed. In traditional SMC, denote $P(z)$ as the transfer function from $s$ to $y$, i.e., $y = P(z)s$. Then $P(z)$ can be obtained as follows. From Equations (6.1)-(6.3) and (6.6),

$$e_1(k+1) = A_{11}e_1(k) + A_{12}[s - \tilde{h}e_1(k)] \tag{6.9}$$

which can be represented through a transfer function, i.e.,

$$e_1 = [zI - (A_{11} - A_{12}\tilde{h})]^{-1}A_{12}s \tag{6.10}$$

Then,

$$\begin{aligned} y &= c_1e_1 + c_2e_2 \\ &= c_1e_1 + c_2(s - \tilde{h}e_1) \\ &= \left[(c_1 - c_2\tilde{h})[zI - (A_{11} - A_{12}\tilde{h})]^{-1}A_{12}) + c_2\right] s \\ &\triangleq P(z)s \end{aligned} \tag{6.11}$$

The two conditions for stability become (a) Approaching condition; (b) $P(z)$ is stable. The stability of $P(z)$ requires that $(A_{11} - A_{12}\tilde{h})$ is Schur; this is consistent with the statement in Section II.

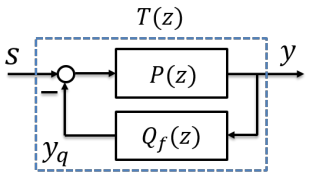


Figure 6.1: Sliding surface dynamics in FSSMC

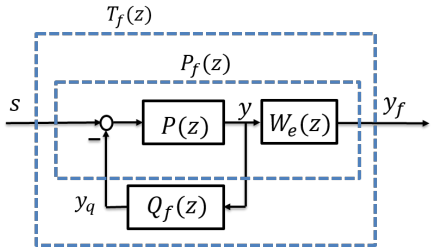


Figure 6.2: Sliding surface dynamics with a weighting filter

## 6.3 H-infinity Based Frequency-shaped SMC

This section describes the design and analysis for FSSMC. As an extension of traditional sliding mode control, FSSMC is proposed to provide specific performance enhancement at certain frequencies. The stability of the sliding surface is one important issue when frequency shaping is introduced. [127] provides one way to check the stability based on root locus technique. However, this approach for stability checking may not be easy when the order of the sliding surface dynamics is high. Here we presents a different frequency-shaping method based on $H_\infty$ synthesis which can easily guarantee the stability of the sliding surface.

In FSSMC, to guarantee the stability and performance, besides the two conditions in the traditional SMC, there is an additional requirement for the sliding surface: the dynamics from $s$ to $y$ should have desired frequency properties. In this chapter, to guarantee the stability of the sliding surface, a shaping filter $Q_f(z)$ is newly introduced in the feedback loop, as shown in Figure 6.1. By augmenting the sliding surface dynamics into a feedback structure, the FSSMC is enabled to suppress disturbances with known characteristics in frequency domain; and the order of the dynamics is increased.

Denote the transfer function from $y$ to $s$ in FSSMC as $T(z)$, i.e., $y = T(z)s$, then

$$T(z) = \frac{P(z)}{1 + P(z)Q_f(z)} \tag{6.12}$$

Similar to traditional SMC, in FSSMC, two conditions need to be satisfied: (1) Approaching condition; (2) $T(z)$ is stable. Additionally, $T(z)$ should have desired frequency properties, i.e., $T(z)$ has small amplifications at frequencies $w_{di}$'s. Those requirements can be satisfied by designing $Q_f(z)$ based on $H_\infty$ synthesis.

The following part of this section provides the design process of $Q_f(z)$, such that $T(z)$ is stable and has desired frequency property. To achieve small amplification of $T(z)$ at $w_{di}$'s, a weighting filter $W_e(z)$ is introduced as shown in Figure 6.2.

Define $P_f(z)$ as the transfer function matrix from $[s,\ y_q]^T$ to $[y_f,\ y]^T$, and define $T_f(z)$ as the transfer function from $s$ to $y_f$. Assume $T_f(z)$ and $P_f(z)$ have the following state-space realizations, respectively

$$T_f : \left[\begin{array}{c} x_f(k+1) \\ \hdashline \xi(k+1) \\ \hdashline y_f(k) \end{array}\right] = \left[\begin{array}{c:c} A_c & B_c \\ \hdashline C_c & D_c \end{array}\right] \left[\begin{array}{c} x_f(k) \\ \hdashline \xi(k) \\ \hdashline s(k) \end{array}\right] \tag{6.13}$$

$$P_f : \left[\begin{array}{c} x_f(k+1) \\ \hdashline y_f(k) \\ \hdashline y(k) \end{array}\right] = \left[\begin{array}{c:cc} A & B_1 & B_2 \\ \hdashline C_1 & D_{11} & D_{12} \\ \hdashline C_2 & D_{21} & D_{22} \end{array}\right] \left[\begin{array}{c} x_f(k) \\ \hdashline s(k) \\ \hdashline y_q(k) \end{array}\right] \tag{6.14}$$

with

$$\begin{gathered} A = \begin{bmatrix} A_p & 0 \\ B_w C_p & A_w \end{bmatrix},\ \begin{bmatrix} B_1 & B_2 \end{bmatrix} = \begin{bmatrix} B_p & -B_p \\ B_w D_p & -B_w D_p \end{bmatrix} \\ \begin{bmatrix} C_1 \\ C_2 \end{bmatrix} = \begin{bmatrix} D_w C_p & C_w \\ C_p & 0 \end{bmatrix},\ \begin{bmatrix} D_{11} & D_{12} \\ D_{21} & D_{22} \end{bmatrix} = \begin{bmatrix} D_w D_p & -D_w D_p \\ -D_p & -D_p \end{bmatrix} \end{gathered} \tag{6.15}$$

where $[A_p, B_p, C_p, D_p]$ is a state-space realization for $P(z)$, and $[A_w, B_w, C_w, D_w]$ is a state-space realization for $W_e(z)$. To find a $Q_f$ filter which minimizes the $H_\infty$-norm of $T_f$, the following optimization problem is formulated:

$$\min_{Q_f,\ \gamma}\ \gamma \tag{6.16a}$$

$$|\lambda_i(A_c)| < 1 \qquad \forall i \tag{6.16b}$$

$$\|T_f\|_\infty < \gamma \tag{6.16c}$$

where $\lambda_i(A_c)$ denotes the $i^{th}$ eigenvalue of $A_c$. Based on the following theorem, the optimization problem (6.16) can be transformed into a convex optimization problem.

**Theorem** ([74]): For the system shown in Figure 6.2 with the state-space realizations in Equations (6.13-6.15), if $D_{22} = 0$, the following statements are equivalent:
(a) $A_c$ is Schur and $\|C_c(zI - A_c)^{-1}B_c + D_c\|_\infty < \gamma$;
(b) There exist symmetric matrices $R$ and $S$ satisfying

$$L_1(R,\gamma) = \left[\begin{array}{c:c} N_R & 0 \\ \hdashline 0 & I \end{array}\right]^T \left[\begin{array}{c:c:c} AR + RA^T & RC_1^T & B_1 \\ \hdashline C_1 R & -\gamma I & D_{11} \\ \hdashline B_1^T & D_{11}^T & -\gamma I \end{array}\right] \left[\begin{array}{c:c} N_R & 0 \\ \hdashline 0 & I \end{array}\right] < 0A \tag{6.17}$$

$$L_2(S,\gamma) = \left[\begin{array}{c:c} N_S & 0 \\ \hdashline 0 & I \end{array}\right]^T \left[\begin{array}{c:c:c} AS + SA^T & SB_1^T & C_1^T \\ \hdashline B_1^T S & -\gamma I & D_{11}^T \\ \hdashline C_1 & D_{11} & -\gamma I \end{array}\right] \left[\begin{array}{c:c} N_S & 0 \\ \hdashline 0 & I \end{array}\right] < 0 \tag{6.18}$$

$$L_3(R,S) = \begin{bmatrix} R & I \\ I & S \end{bmatrix} \geq 0 \tag{6.19}$$

where $N_R$ and $N_S$ denote the bases of the null spaces of $(B_2^T,\ D_{12}^T)$ and $(C_2^T,\ D_{21}^T)$, respectively. When $D_{22} = 0$, based on the Theorem 1, the optimization problem (6.16) can be reformulated as

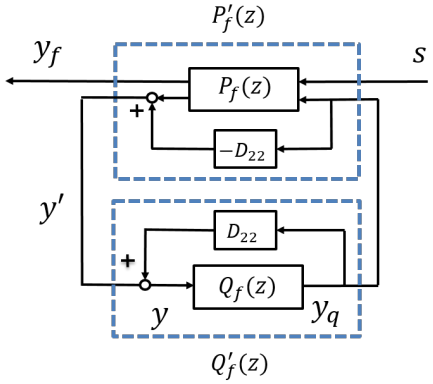


Figure 6.3: Equivalent sliding surface dynamics with a weighting filter

a convex optimization problem with linear matrix equality (LMI) constraints (6.17-6.19) that are dependent on Equations (6.13) to (6.15). Noting that $P_{f,22}(z) = -P(z)$ and Eq. (6.11), $D_{22}$ can be non-zero; in this case, the following transformation can be made before applying Theorem 1 [74]

$$P_f' = P_f - \begin{bmatrix} 0 & 0 \\ 0 & D_{22} \end{bmatrix} \tag{6.20a}$$

$$Q_f' = [I - D_{22}Q_f]^{-1}Q_f \tag{6.20b}$$

Figure 6.3 illustrates such transformation. After $Q_f'$ is obtained through solving the convex optimization problem (6.16), $Q_f$ can be obtained thereafter through Equation (6.20b).

## 6.4 An Explicit Suboptimal Solution

In general the suitable weighting filter differs among various disturbance sources. It is not efficient to solve the optimization problem (6.16) every time when the disturbance sources change. This motivates a shaping filter which is explicitly dependent on $w_d$'s. One approach of obtaining the parameter-dependent sub-optimal filter was proposed in [130, 131]. This approach requires that the state-space matrices of $P_f(z)$ are affine in the parameters of $w_d$'s, which may not always be satisfied and limits the flexibilities in the design of $W_e$. Furthermore, the constructed solutions through this approach are usually conservative by taking linear parameter-varying systems into consideration. This motivates an interesting question: is it possible to design an optimal/suboptimal shaping filter that is explicitly dependent on the weighting filter? Within this motivation, the optimization problem (6.16) is modified as follows,

$$\min_{Q_f\{W_e\},\ \gamma\{W_e\}} \quad \gamma\{W_e\} \tag{6.21a}$$

$$|\lambda_i(A_c\{W_e\})| < 1 \qquad \forall i \tag{6.21b}$$

$$\|T_f\{W_e\}\|_\infty < \gamma(W_e) \tag{6.21c}$$

It is challenging to obtain the optimal filter explicitly dependent on $W_e$. Alternatively, a suboptimal solution that is explicitly dependent on $W_e$ is beneficial enough in practice. We provide the following proposition for the construction of such a suboptimal filter.

**Proposition**: Suppose (1) $P(z)$ is a stable minimum-phase system with a causal pseudo inverse $P^\dagger(z)$; (2) $W_e(z)$ is a stable minimum-phase weighting filter; (3) $Q_f$ is the shaping filter incorporated in the 'feedback' loop as shown in Figure 6.1. The following design of $Q_f(z)$ can guarantee the stability and bounded $H_\infty$-norm of the sliding surface dynamics:

$$Q_f\{W_e\} = [\gamma^*(z)]^{-1}W_e(z) - P^\dagger(z) \tag{6.22}$$

where $\gamma^*(z)$ is a stable, invertible and minimum-phase filter that satisfies $\|\gamma^*(z)\|_\infty < 1$ and

$$|\gamma^*(e^{j\Theta})(1 - P(e^{j\Theta})P^\dagger(e^{j\Theta}))| << 1 \quad \forall\Theta \in [0, 2\pi) \tag{6.23}$$

**Proof:** From the definition of $T_f$ in Figure 6.2 (the transfer function from $s$ to $y_f$),

$$\begin{aligned} T_f(z) &= \frac{P(z)}{1 + P(z)Q_f(z)}W_e(z) \\ &= \frac{P(z)}{1 + P(z)([\gamma^*(z)]^{-1}W_e(z) - P^\dagger(z))}W_e(z) \\ &= \frac{P(z)\gamma^*(z)}{\gamma^*(z)(1 - P(z)P^\dagger(z)) + P(z)W_e(z)}W_e(z) \end{aligned} \tag{6.24}$$

From Equation (6.23), the magnitude of $\gamma^*(z)(1-P(z)P^\dagger(z))$ over a large frequency range is small; therefore $T_f(z)\approx\gamma^*(z)$, and $T(z)\approx\gamma^*(z)/W_e(z)$. Noting that $P(z)$, $W_e(z)$ and $\gamma^*(z)$ are all stable minimum-phase systems, the derivation in Equation (6.24) does not cause unstable zero-pole cancellation. Therefore, $T_f$ is stable and $\|T_f(z)\|_\infty<1$.

This proposition provides an efficient approach to construct the shaping filter $Q_f(z)$ that is strictly affine in the weighting filter $W_e(z)$, which is usually designed based on the frequency characteristics of the disturbances. Two follow-up remarks on $P^\dagger(z)$ and $\gamma^*(z)$ are provided as follows.

- **Remark 1**: There are several ways to design $P^\dagger(z)$. A good design of $P^\dagger(z)$ should guarantee that $P(e^{j\Theta})P^\dagger(e^{j\Theta})=1$ over a large frequency range. Considering $P(z)$ is a stable minimum-phase system, a simple design of $P^\dagger(z)$ is suggested as follows

$$P^\dagger(z) = F_P(z)P^{-1}(z) \tag{6.25}$$

where $P^{-1}(z)$ is the exact inverse of $P(z)$ and $F_P(z)$ is a filter to maintain the causality of $P^{\dagger}(z)$. For example, $F_P(z)$ can be designed in the following format

$$F_P(z) = M\left(\frac{1}{z+\tau}\right)^r \tag{6.26}$$

where $M$ is a constant to maintain $F_P(e^{j0}) = 1$, $r$ is an integer larger or equal to the relative degree of $P(z)$ to maintain the causality of $P^{\dagger}(z)$, and $\tau$ is a small integer.

- **Remark 2:** The construction of $Q_f(z)$ using Equation (6.22) needs a good design of $\gamma^*(z)$. From Proposition 1, $\gamma^*(z)$ should be biproper (i.e., $\gamma(z)$ has equal number of poles and zeros) and all the zeros and poles are stable; furthermore, it should be designed such that Equation (6.23) is satisfied. Usually $\gamma^*(z)$ can be designed as a low-pass filter because the mismatch between $P(z)$ and $1/P^{\dagger}(z)$ usually happens at high frequencies.

Based on Proposition 1 and the two follow-up remarks, the steps of constructing a shaping filter that is explicitly dependent on $W_e(z)$ are summarized as follows:

(a) Design a sliding surface according to Equation (6.6).
(b) Calculate the transfer function representation of the sliding surface dynamics $P(z)$ according to Equation (6.11).
(c) Design a causal (pseudo) inverse for $P(z)$; suggestions are given in Remark 1 and Equations (6.25) to (6.26).
(d) Design $\gamma^*(z)$ according to Equation (6.23); suggestions are given in Remark 2.
(e) Design the weighting filter $W_e(z)$ based on the frequency characteristics of the disturbances which can be obtained from either sensors or disturbance estimators (for example, disturbance observers [132] or extended state observers [89].
(f) Design the shaping filter $Q_f(z)$ according to Equation (6.22).

Until now, a shaping filter $Q_f(z)$ that is explicitly dependent on (and affine in) the weighting filter $W_e(z)$ has been constructed. The shaping filter can guarantee both the stability and desired frequency responses of the sliding surface dynamics.

## 6.5 Controller Design

This section provides sliding mode control design for the system (6.1) with the frequency-shaped sliding surface defined in Figure 6.1. Assume $Q_f$ has been already obtained from Sections 3 (optimal filter) or 4 (suboptimal filter), and it has the following state-space realization

$$Q_f : \left[\begin{array}{c:c} \xi(k+1) \\ \hdashline y_q(k) \end{array}\right] = \left[\begin{array}{c:c} \bar{A} & \bar{B} \\ \hdashline \bar{C} & \bar{D} \end{array}\right] \left[\begin{array}{c:c} \xi(k) \\ \hdashline y(k) \end{array}\right] \tag{6.27}$$

Combining Equation (6.1) and Equation (6.27), the augmented system can be written as

$$x_e(k+1) = A_e x_e(k) + B_e(u(k) + d(k)) \tag{6.28}$$

where $x_e(k) = [e(k)^T, \ \xi(k)^T]^T$, and

$$A_e = \begin{bmatrix} A_p & 0 \\ \bar{B}C_p & \bar{A} \end{bmatrix}, \ B_e = \begin{bmatrix} B_p \\ 0 \end{bmatrix} \tag{6.29}$$

Noting Equation (6.12), in frequency domain, the frequency-shaped sliding variable $s$ is derived as follows

$$s = T(z)^{-1}y = \frac{1}{P(z)}y + Q_f(z)y. \tag{6.30}$$

From Equations (6.30) and (6.27), in time domain, the sliding variable $s$ becomes

$$\begin{aligned} s(k) &= He(k) + \bar{C}\xi(k) + \bar{D}C_p e(k) \\ &= \begin{bmatrix} H + \bar{D}C_p & \bar{C} \end{bmatrix} \begin{bmatrix} e(k) \\ \xi(k) \end{bmatrix} \triangleq H_e x_e(k) \end{aligned} \tag{6.31}$$

The frequency-shaped sliding mode controller is designed as

$$\begin{aligned} u(k) = &[H_e B_e]^{-1}[(1 - qT_s)s(k) - H_e A_e x_e(k) - \\ &(\epsilon T + H_e B_e D)\text{sgn}(s(k))] \end{aligned} \tag{6.32}$$

where $0<qT_s<1$ and $0<\epsilon \ll 1$. Substituting Equations (6.32) and (6.28) into Equation (6.31), the actual approaching dynamics becomes

$$\begin{aligned} s(k+1) = &(1 - qT_s)s(k) - \\ &[\epsilon T_s + (H_e B_e D - H_e B_e d(k))]\text{sgn}(s(k)) \end{aligned} \tag{6.33}$$

which guarantees that $s(k)$ enters the band $[-\Delta, \Delta]$ in finite time steps, where

$$\Delta = (\epsilon T_s + \eta)/(1 - qT_s) > 0 \tag{6.34}$$

with $\eta = H_e B_e (D - d) \geq 0$. Detailed explanation is provided as follows. According to Equation (6.33), the approaching dynamics can be written as follows

$$s(k+1) = (|s(k)| - \Delta)(1 - qT_s)\text{sgn}(s(k)) \tag{6.35}$$

If $|s(k)|>\Delta$, then $\text{sgn}(s(k+1))=\text{sgn}(s(k))$ and $|s(k+1)| = (|s(k)| - \Delta)(1-qT_s) < |s(k)|$, $s$ would move towards the band monotonically; similarly, if $|s(k)|<\Delta$, then $\text{sgn}(s(k+1))= -\text{sgn}(s(k))$ and $|s(k+1)|=(\Delta - |s(k)|)(1-qT)<\Delta$, $s$ would cross the switching plane, change its sign at every step and stay in the band thereafter. To reduce the chattering phenomenon in SMC, $\text{sgn}(s(k))$ is usually replaced by a saturation function of $s(k)$ in real implementation.

In summary, given $P(z)$ and $W_e(z)$, a shaping filter $Q_f(z)$ can be constructed through solving the convex optimization problem (6.16). To address more general disturbances, $W_e(z)$ is preferred to be re-designed when the frequency characteristics of the disturbances change a lot. In these cases, a shaping filter that is explicitly dependent on $W_e(z)$ is desired, and Proposition 1 provides a construction approach for such a filter. After the shaping filter $Q_f(z)$ is constructed, a frequency-shaped sliding surface is defined in Figure 6.1, and a sliding mode controller is designed in Equation (6.32). Subsequently, the system (6.1) is stabilized with desired frequency properties.

## 6.6 Simulation Validation

This section applies the proposed FSSMC to suppress the vibrations with multiple peak frequencies in HDDs. To suppress this type of vibrations, the weighting filter is designed as a peak filter with multiple peak frequencies at $w_{di}$'s,

$$W_e(z) = \prod_{i=1}^{N} \frac{B_i(z)}{A_i(z)} \tag{6.36}$$

where

$$B_i(z) = 4(z-1)^2 + 4T_s b_i w_{di}(z-1)(z+1) + T_s^2 w_{di}^2 (z+1)^2$$
$$A_i(z) = 4(z-1)^2 + 4T_s a_i w_{di}(z-1)(z+1) + T_s^2 w_{di}^2 (z+1)^2$$

$N$ is the number of vibration peak frequencies to deal with; $a_i$ and $b_i$ are parameters to determine the magnitudes and the widths of the peaks. In this simulation study, all the $a_i$'s are set as 0.03, and all the $b_i$'s are set as 0.3. Three files of vibration data modified from actual drive tests are injected into the simulation systems. Correspondingly, three shaping filters are utilized for the three vibration sources: (1) single-peak case (Figure 6.4) with peak frequency of 1250 Hz ($N$=1, $w_{d1}$=1250); (3) double-peak case (Figure 6.6) with peak frequencies of 1250 Hz and 2500 Hz ($N$=2, $w_{d1}$=1250 and $w_{d2}$=2500); (3) triple-peak case (Figure 6.8) with peak frequencies of 1250 Hz, 2500 Hz and 4000 Hz ($N$=3, $w_{d1}$=1250, $w_{d2}$=2500 and $w_{d3}$=4000). The corresponding PES spectrum comparisons are provided in Figures 6.5, 6.7, and 6.9, respectively.

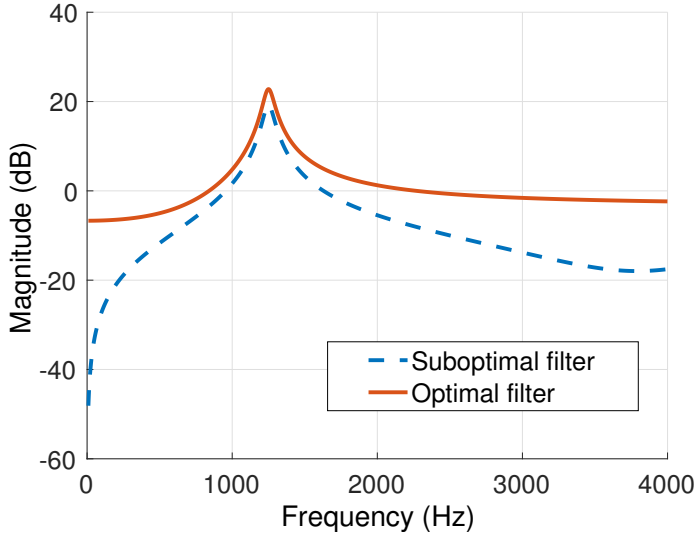


Figure 6.4: Bode plots of optimal and suboptimal shaping filters (single-peak)

To show the benefits of the proposed frequency-shaping techniques, three control algorithms are compared: traditional SMC, the proposed FSSMC and the proposed suboptimal FSSMC.

(1) *Comparison between SMC and FSSMC*: In single-peak case, the Bode plot of $Q_f(z)$ is as shown in Figure 6.4. Figure 6.5 indicates that the large peak around 1250 Hz has been reduced

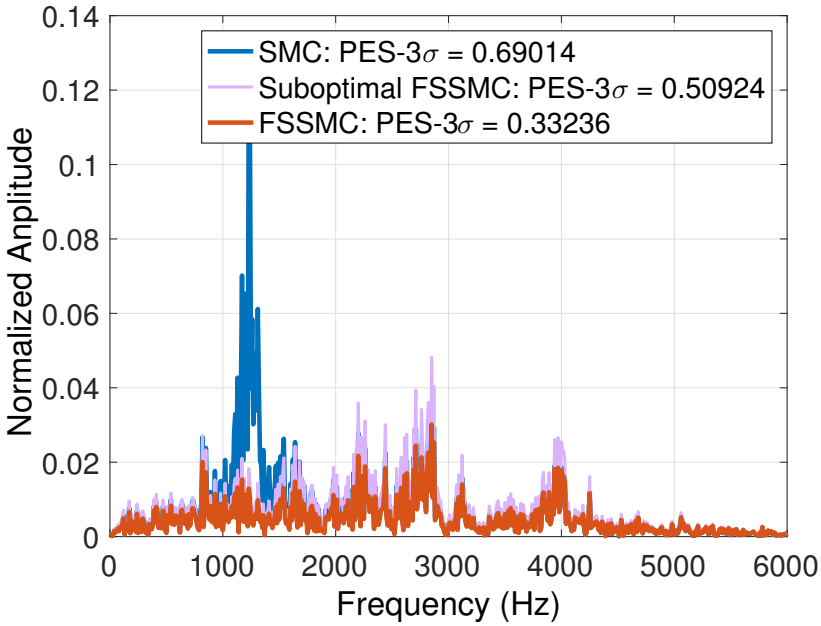


Figure 6.5: PES spectrum comparison (single-peak)

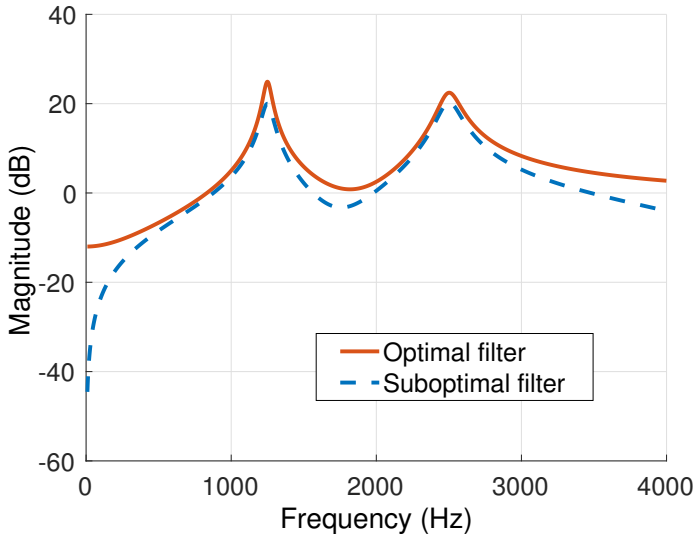


Figure 6.6: Bode plots of optimal and suboptimal shaping filters (double-peak)

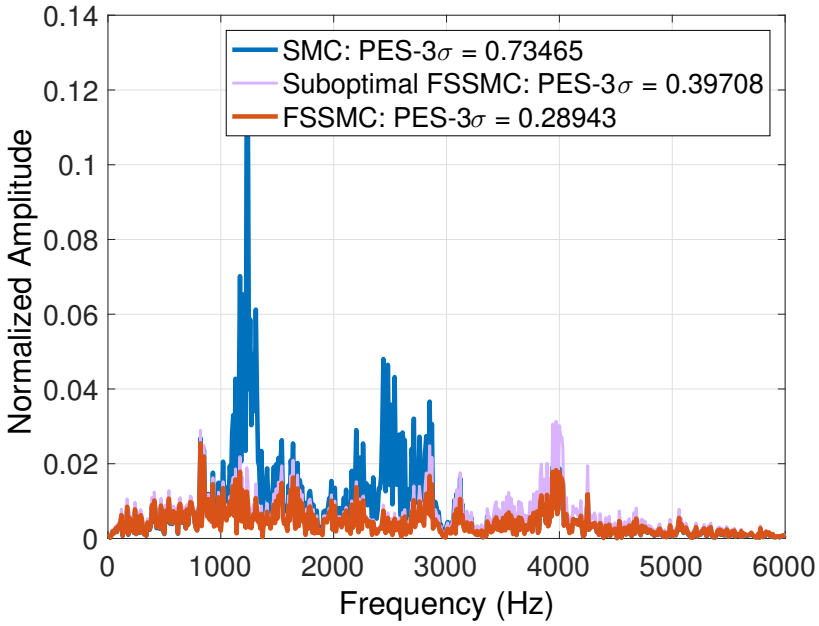


Figure 6.7: PES spectrum comparison (double-peak)

significantly by FSSMC, and the $3\sigma$ value of PES has been reduced from 0.690 to 0.332, approximately 52% reduction. Similar benefits have been demonstrated in both double-peak case and triple-peak case. Figure 6.7 indicates that large peaks around 1250 Hz and 2500 Hz have been reduced by FSSMC, and the $3\sigma$ value of PES has been reduced from 0.735 to 0.289, approximately 61% reduction. Figure 6.9 indicates that large peaks around 1250 Hz, 2500 Hz and 4000 Hz have been reduced by FSSMC, and the $3\sigma$ value of PES has been reduced from 0.665 to 0.344, approximately 48% reduction. In summary, FSSMC has better performance than traditional SMC in the sense of large vibration peak supression.

(2) *Comparison between FSSMC and suboptimal FSSMC*: Figure 6.4, 6.6 and 6.8 also compare the optimal shaping filters and the suboptimal filters. The optimal filters are obtained through solving the $H_\infty$ optimization problem and the suboptimal filters are obtained directly through Proposition 1. Figure 6.5, 6.7 and 6.9 compare their corresponding PES spectrums. It is noticed that, although the $3\sigma$ values of the PES have been slightly sacrificed using the sub-optimal filters, the PES still have been reduced significantly compared to the traditional SMC without frequency shaping. A brief summary of those improvements by FSSMC and suboptimal FSSMC are provided in Table 6.1.

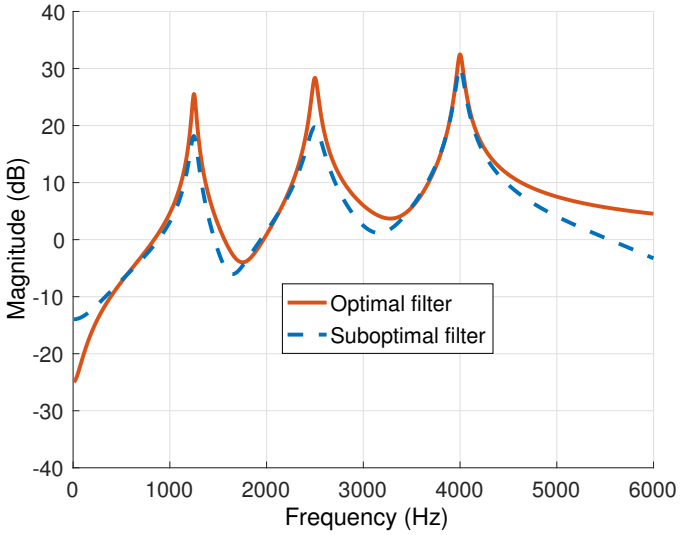


Figure 6.8: Bode plots of optimal and suboptimal shaping filters (triple-peak)

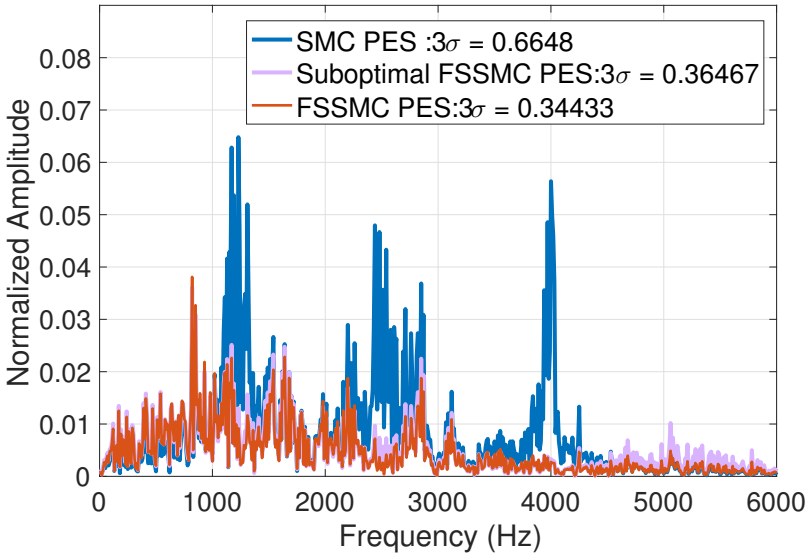


Figure 6.9: PES spectrum comparison (triple-peak)

| $N$ | $w_d$'s (Hz) | SMC | Suboptimal FSSMC | FSSMC |
|---|---|---|---|---|
| 1 | {1250} | 0.69014 | 0.50924 (↓ 26%) | 0.33236 (↓ 52%) |
| 2 | {1250, 2500} | 0.73465 | 0.39708 (↓ 46%) | 0.28943 (↓ 61%) |
| 3 | {1250, 2500, 4000} | 0.66480 | 0.36467 (↓ 45%) | 0.34433 (↓ 48%) |

Table 6.1: Comparison of $3\sigma$ values of PES

## 6.7 Chapter Summary

This chapter has presented a frequency shaping method for the sliding surface based on $H_\infty$ synthesis for performance enhancement of sliding mode control. The sliding surface dynamics has been augmented as a 'feedback' system; the shaping filter has been considered as the feedback controller, which assures the stability of the sliding surface and desired frequency responses. This method minimizes the weighted $H_\infty$-norm of the sliding surface dynamics, and provides design flexibilities in incorporating standard loop shaping techniques into sliding mode control. This approach has been further advanced to be the weighting filter dependent FSSMC to gain greater efficiency and more flexibilities. Detailed evaluations have been performed on a simulated hard disk drive, which is subject to serious external vibrations with multiple peak frequencies. The effectiveness of the suppression of vibrations has been demonstrated.

# Chapter 7

# Advanced Frequency-shaped Sliding Mode Control

This chapter presents frequency-shaped sliding mode control (FSSMC) techniques when the state variables are not directly measurable and/or the vibration information is not available through vibration sensors and need to be obtained online.

## 7.1 ESO-based Frequency-shaped SMC

This section presents FSSMC algorithm based on the extended state observer (ESO) with the phase compensator presented in Chapter 4. The ESO estimates both the states and the disturbances. Based on these estimates, the FSSMC is implemented to further suppress large peaks in the disturbances. The control scheme is provided in Figure 7.1. To illustrate the effectiveness of both the ESO and the FSSMC, simulation study is performed on the hard disk drive (HDD) Benchmark model, and four systems with different control schemes (listed in Table 7.1) are compared and analyzed. The comparisons of the position error signal (PES) are provided in Figures 7.2 to 7.4. The accumulative $3\sigma$ value of PES is calculated and provided in each figure.

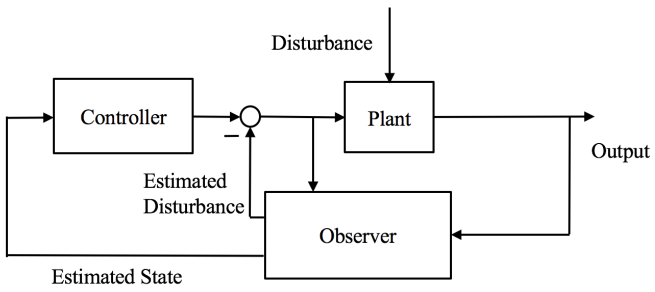


Figure 7.1: Control scheme

| System index | System |
|---|---|
| a | Standard SMC with the conventional state observer |
| b | Standard SMC with the standard ESO |
| c | FSSMC with the standard ESO |
| d | FSSMC with the compensated ESO |

Table 7.1: Different systems studied in simulation

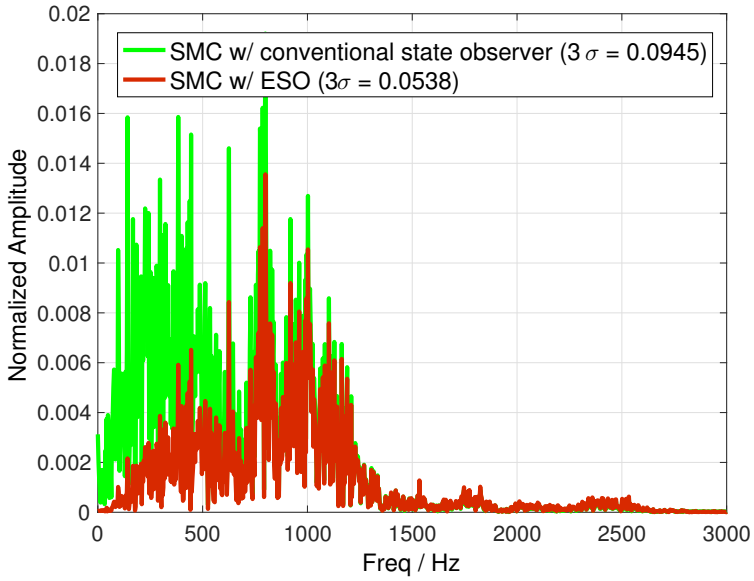


Figure 7.2: PES spectrum comparison: systems (a) and (b)

Figure 7.2 compares (a) and (b), and the PES below 500 Hz is reduced by introducing the standard ESO instead of the conventional state observer. Figure 7.3 compares (b) and (c), and the PES around 1000 Hz is reduced by the frequency shaping technique in FSSMC. Figure 7.4 compares (c) and (d), and the PES around 500 Hz is reduced by the phase compensator in the compensated ESO. Overall, the $3\sigma$ value of the PES has been reduced from 9.45% to 2.01%. The sensitivity from the disturbances to the PES is a key criterion to evaluate the servo performance in HDDs. Figure 7.5 provides both the calculated and the fitted frequency responses of the sensitivity functions in systems (a) to (d). It is shown that system (d) has better vibration suppression than systems (a) (b) and (c), with insignificant sacrifice at other frequencies. The effectiveness of high-frequency vibration suppression is demonstrated.

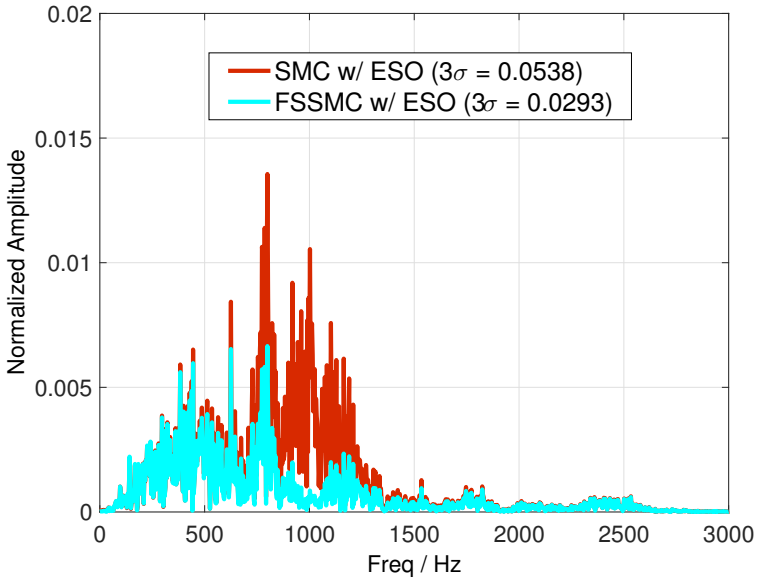


Figure 7.3: PES spectrum comparison: systems (b) and (c)

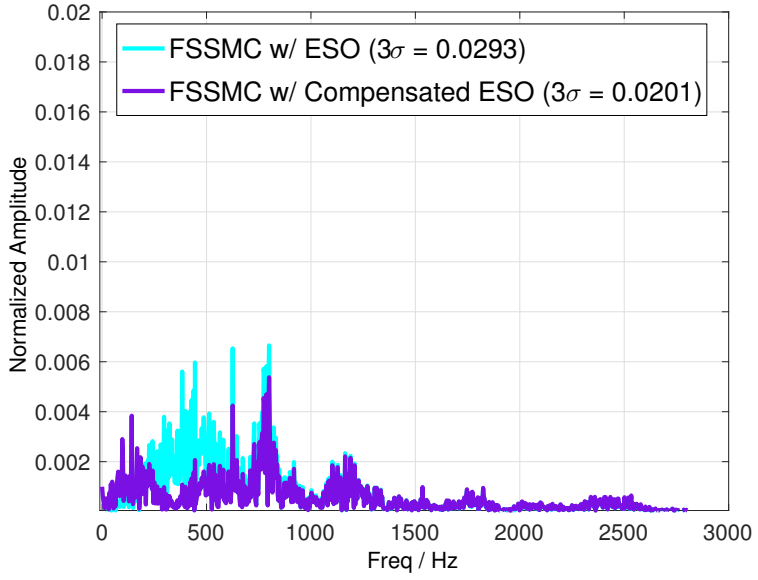


Figure 7.4: PES spectrum comparison: systems (c) and (d)

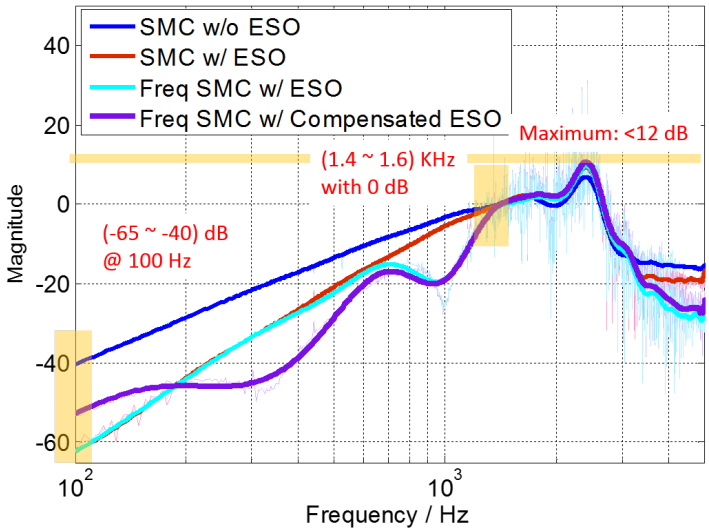


Figure 7.5: Calculated and fitted sensitivities

## 7.2 Multi-rate Frequency-shaped SMC

There usually exist resonance modes near and beyond the Nyquist frequency in HDDs. Such resonance modes, if excited, will generate vibrations beyond the Nyquist frequency which would seriously degrade the servo performance. To capture such vibrations, a multi-rate extended observer is designed based on the nominal dynamic model of the excitation process in Chapter 4. This observer estimates both the states and the vibrations at a fast rate based on the sampled PES at a slow rate.

This section presents the frequency-shaping beyond the Nyquist frequency in SMC based on the multi-rate observer presented in Chapter 4. The whole control scheme is shown in Figure 7.6, where $T_s$ is the PES sampling rate, and $T_f$=$T_s/N$ is the plant's and the disturbances' updating rate. The vibration estimate is incorporated into the control signal to compensate the actual vibrations. The controller is designed based on the state estimates by the observer. To enhance the servo performance which is seriously degraded by the vibration beyond the Nyquist frequency, in FSSMC, a peak filter $Q_f$ with the peak frequency beyond the Nyquist frequency (as shown in Figure 7.7) is designed to shape the sliding surface. More details are available in [101]. Three control algorithms are implemented into the simulation and the spectrums of the PES are compared: single-rate SMC, multi-rate SMC, and multi-rate frequency-shaped SMC. In this simulation study, $T_s = 3.7879 \times 10^{-5}$ sec, and $N = 4$.

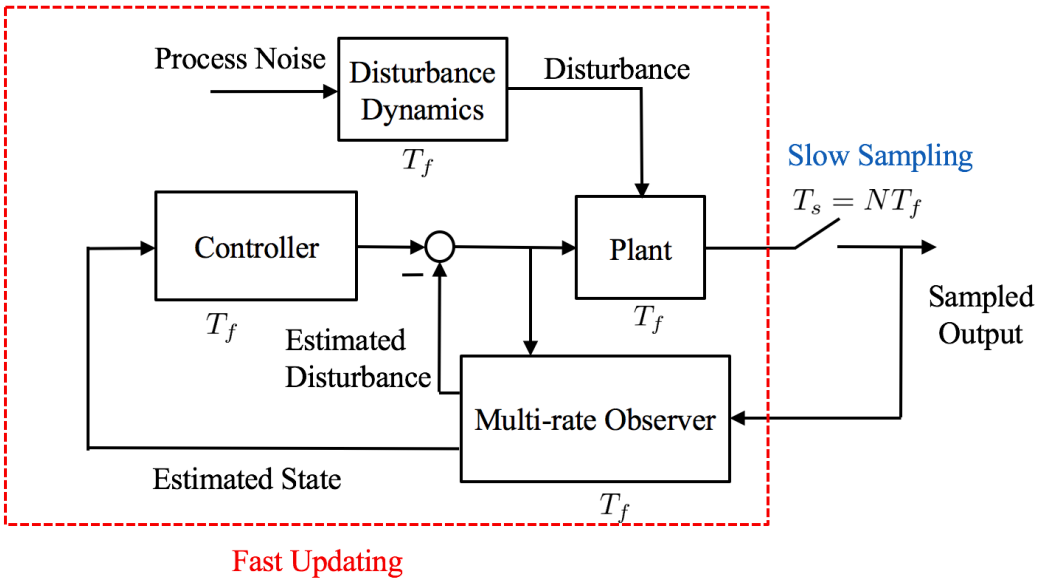


Figure 7.6: Multi-rate control system for HDD

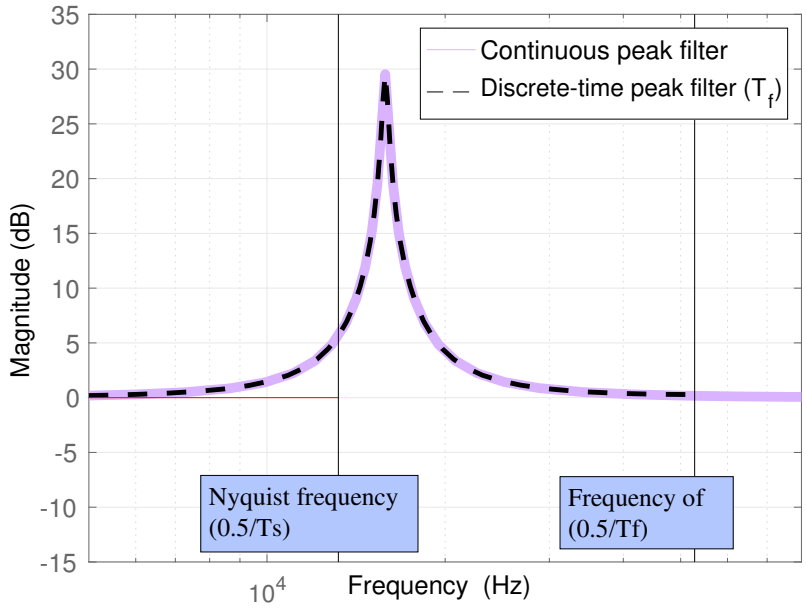


Figure 7.7: Peak filter in frequency-shaped SMC

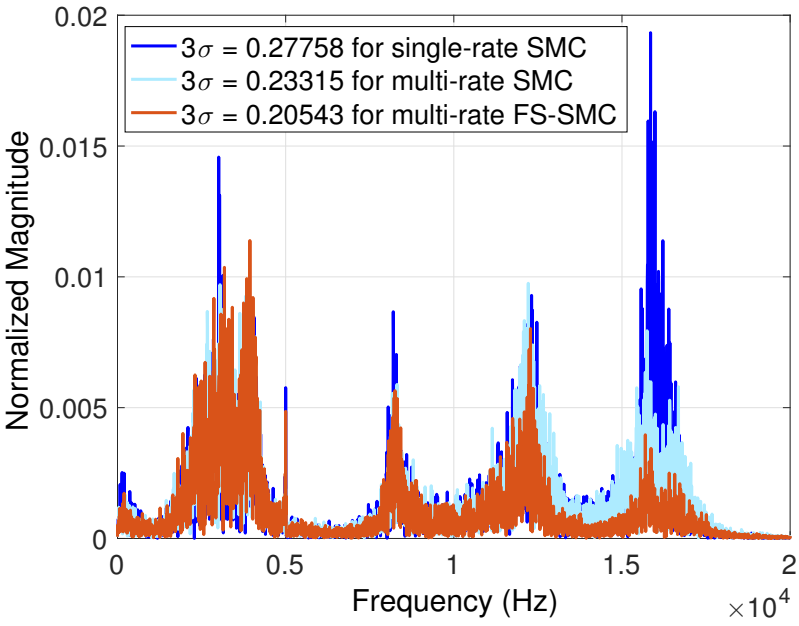


Figure 7.8: PES comparison in frequency domain

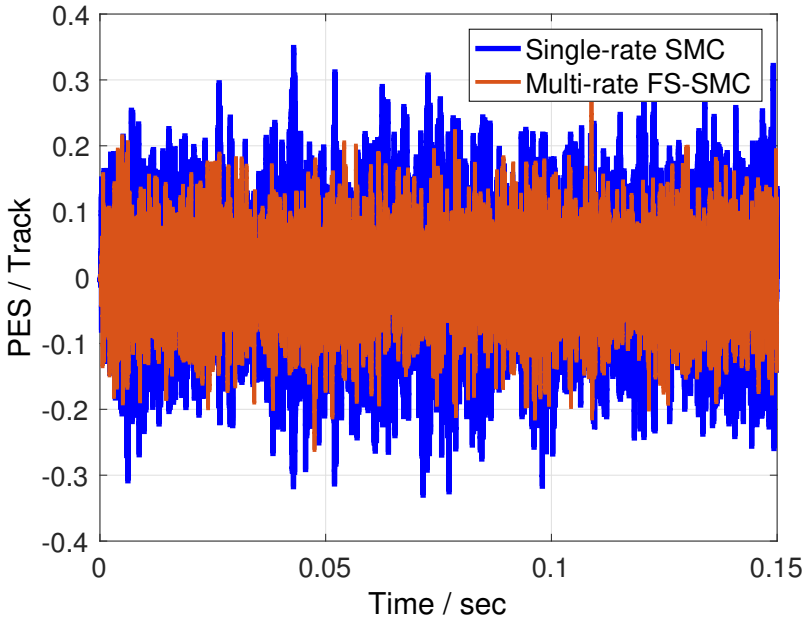


Figure 7.9: PES comparison in time domain

Figures 7.8 and 7.9 compare the PES among the above three algorithms. The parameters in the single-rate SMC and multi-rate SMC are set such that they have the same equivalent continuous-

time system. As shown in Figure 7.8, the PES spectrums of the system with single-rate SMC and the one with multi-rate SMC are close to each other below the Nyquist frequency. Comparatively, the PES beyond the Nyquist frequency in the multi-rate SMC system has been reduced compared to the one in the single-rate SMC system. Such reduction is contributed by the compensation of actual vibration using the fast vibration estimate. Moreover, through comparing the PES spectrums of the one with multi-rate SMC and the one with multi-rate FSSMC, it shows the PES beyond the Nyquist frequency has been further reduced by introducing the frequency shaping beyond the Nyquist frequency in FSSMC. Figure 7.9 compares the time-domain PES of the two systems with single-rate SMC and multi-rate FSSMC. It is shown that the peak to peak value of the PES has been reduced.

Multi-rate technique with nominal dynamic model of the disturbance allows frequency shaping and vibration suppression beyond the Nyquist frequency.

## 7.3 Adaptive Frequency-shaped SMC

In modern high-precision motion systems, narrow-band disturbance rejection is always a challenging topic [133–135]. Such disturbances, if not handled properly, may cause significant performance degradation to the servomechanism. It becomes even worse when there exist multiple large unknown peaks in the disturbances. Fortunately, in HDDs, the narrow-band disturbances are usually caused by the non-repetitive run-out (NRRO), and the frequency range for each peak can be known in advance [30, 136]. Based on such priorly known frequency ranges, band-pass filters can be utilized to separate the vibrations into several frequency segments, and these central frequencies can be easily identified online.

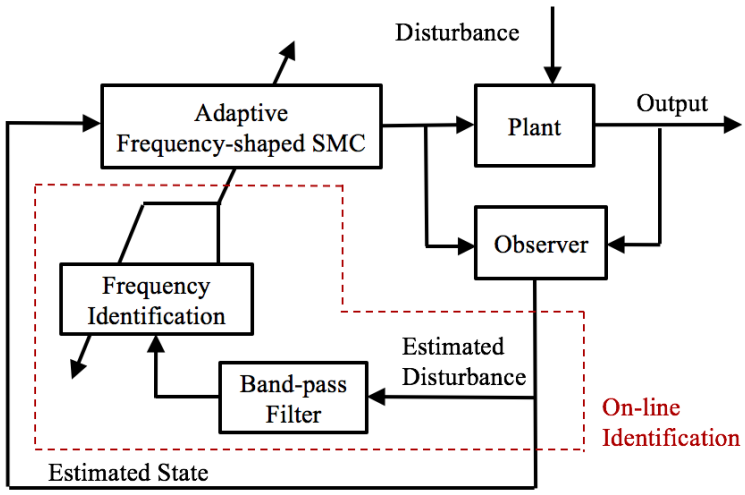


Figure 7.10: Control scheme

This section provides an adaptive frequency-shaped sliding mode control (AFSSMC) algorithm to deal with such disturbances. The AFSSMC incorporates a peak filter with varying central

frequencies to shape the sliding surface and thus provides on-line frequency-dependent control allocation. The ESO presented in Chapter 4 is utilized here to estimate both the states and the disturbances. The disturbance estimate is utilized to take place of the disturbance sensor, identify the peak frequencies of the disturbance and adaptively tune the peak filter in AFSSMC; the state estimate is utilized to generate the control signal. The whole control scheme is shown in Figure 7.10. Assume the disturbance $d$ contains multiple peak frequencies at $w_{di}$'s ($i$=1, 2, ..., $N$), where $w_{di}$'s are not exactly known and need to be identified online. Band-pass filters (denoted as $B_i$'s, $i$=1, 2, ..., $N$) are utilized to separate the disturbances into several frequency ranges. Examples of the band-pass filters are shown in Figure 7.11 ($N$=2). The stability issue of the AFSSMC was briefly discussed in [137]. For such time-varying systems, an alternative method to analyze the stability is the numerical technique based on Lyapunov stability theory which has been recently applied to some other areas [138–141].

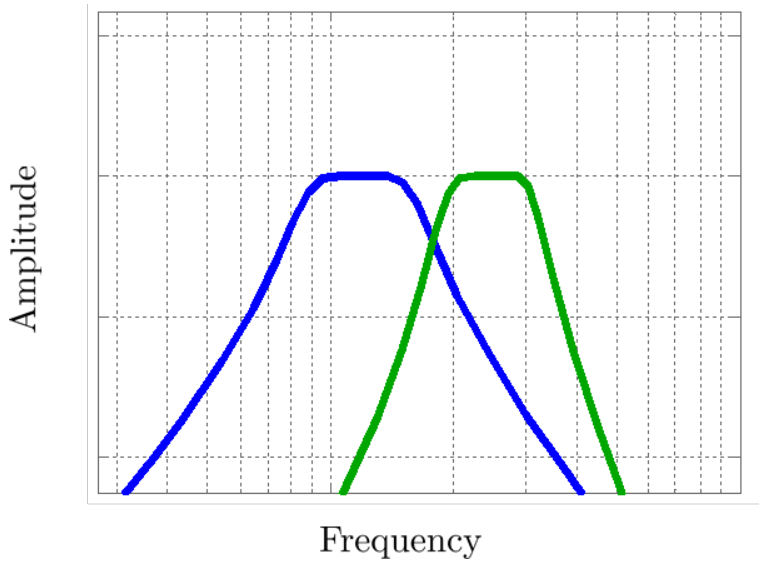


Figure 7.11: Band-pass filters

## Peak Frequency Estimation

Define $d_i$=$B_i\{d\}$, which represents the dominant component of $d$ around $w_{di}$. It is reasonable to assume that $d_i(k)$ is a sinusoidal signal [30, 136, 142], i.e.,

$$d_i(k) = A_i \sin(\Omega_{di} k + \phi_i) + n_i(k) \quad i = 1, 2, 3... \tag{7.1}$$

where $\Omega_{di}$=$2\pi T_s w_{di}$, $A_i$ represents the amplitude, $\phi_i$ represents the phase shift, and $n_i$ is reasonably assumed as zero-mean white noise. Then we have

$$d_i(k) + d_i(k-2) = 2\cos(\Omega_{di}) d_i(k-1) + n_i(k) + n_i(k-2) \tag{7.2}$$

which can be further written as

$$d_i(k) + d_i(k-2) = \theta_i \phi_i(k) + \bar{n}_i(k) \tag{7.3}$$

with $\theta_i$=$2\cos(\Omega_{di})$, $\phi_i(k)$=$d_i(k-1)$ and $\bar{n}_i(k)$=$n_i(k)+n_i(k-2)$. To identify $\theta_i$, the following standard adaptive identification algorithm is implemented,

$$\begin{aligned} e_i^o(k+1) &= d_i(k)+d_i(k-2)-\hat{\theta}_i(k)\phi_i(k) \\ \hat{\theta}_i(k+1) &= \hat{\theta}_i(k)+\frac{F(k)\phi_i(k)e_i^o(k+1)}{\lambda_1(k)+\phi_i^T(k)F(k)\phi_i(k)} \\ F_i(k+1) &= \frac{1}{\lambda_1(k)}[F_i(k)-\frac{\lambda_2(k)[F_i(k)\phi_i(k)]^2}{\lambda_1(k)+\lambda_2(k)F_i(k)\phi_i(k)^2}] \end{aligned} \tag{7.4}$$

where $d_i(k)$ is assumed to be available, $\lambda_1(k)$ is usually selected as a constant close to (and less than) 1, and $\lambda_2(k)$ is usually selected as constant 1. With persistence of excitation, $\hat{\theta}_i(k)$ converges to $\theta_i$. And

$$\hat{w}_{di} = \frac{\cos^{-1}(\hat{\theta}_i/2)}{2\pi T_s} \tag{7.5}$$

When $d(k)$ is not directly measurable, it is replaced by its estimate $\hat{d}(k)$ which is obtained through the ESO presented in Chapter 4.

The AFSSMC is evaluated through the simulation on the full-order HDD Benchmark model. Two control algorithms are compared: traditional SMC and the proposed AFSSMC. Two cases are simulated: narrow-band disturbances with single and multiple peak frequencies. More details are available in [137]

## (a) Single-peak Case

Figures 7.13 to 7.15 provide the simulation results when there is one peak frequency ($w_d$=2500 Hz) in the disturbances, as shown in Figure 7.12. Figure 7.13 shows the identification of the peak frequency. Figure 7.14 compares the PES spectrums with the AFSSMC and the traditional SMC: the $3\sigma$ value of the PES has been reduced from 8.53% to 3.20%; the peak in the PES has been suppressed significantly. Figure 7.15 compares the PES in time domain: the peak-to-peak value of the PES has been reduced by the AFSSMC.

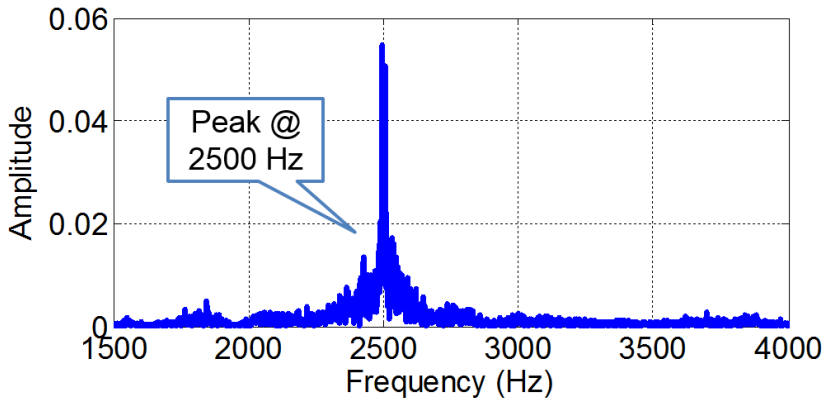


Figure 7.12: Narrow-band disturbances with single peak

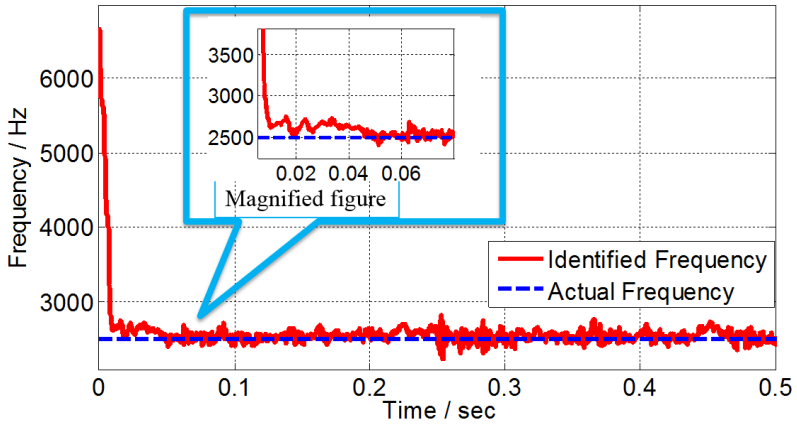


Figure 7.13: Frequency identification

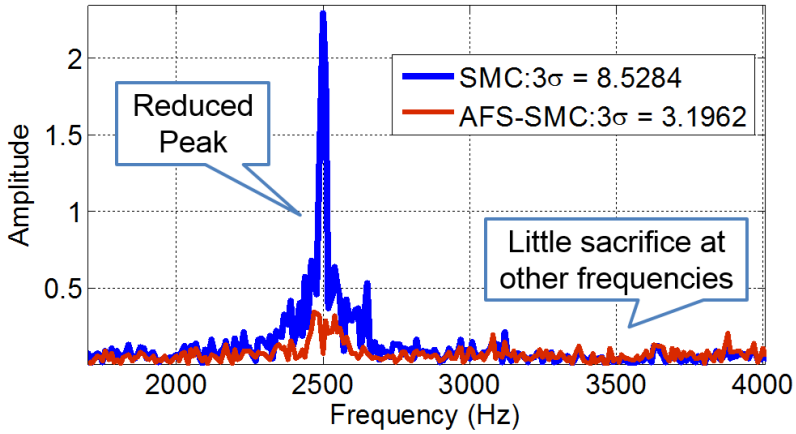


Figure 7.14: PES spectrum comparison

## (b) Multiple-peak Case

Figures 7.18 to 7.20 provide the simulation results when the disturbance contains three peak frequencies ($w_{d1}$=1200 Hz, $w_{d2}$=2500 Hz and $w_{d3}$=4000Hz), as shown in Figure 7.16. Prior information of these frequency ranges for $w_{di}$'s is known as: 1000-1500 Hz, 2000-3000 Hz, and 3800-4800 Hz, respectively. Figure 7.18 shows the identification of the peak frequencies $w_{di}$'s. Figure 7.19 compares the PES spectrums with the proposed AFSSMC and the traditional SMC: the $3\sigma$ value of the PES has been reduced from 55.17% to 23.72% and the peaks in the PES spectrum have been suppressed. Figure 7.20 compares the PES in time domain, and the peak-to-peak value of the PES has been reduced via AFSSMC.

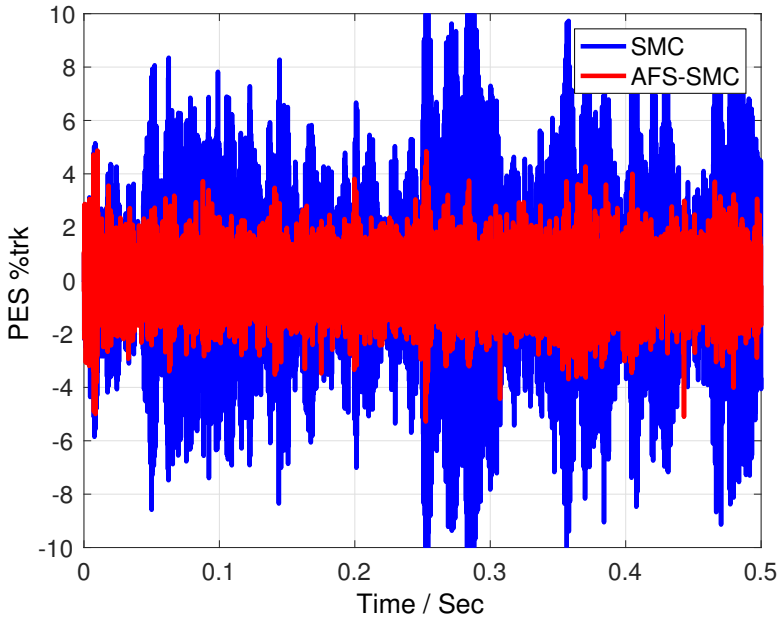


Figure 7.15: PES comparison in time domain

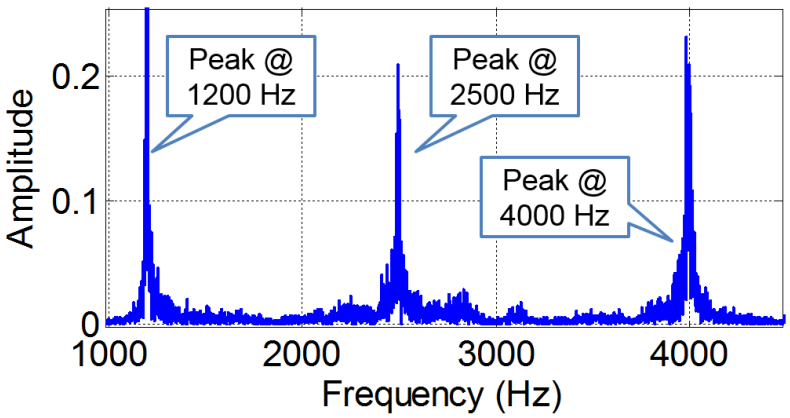


Figure 7.16: Narrow-band disturbances with multiple peak frequencies

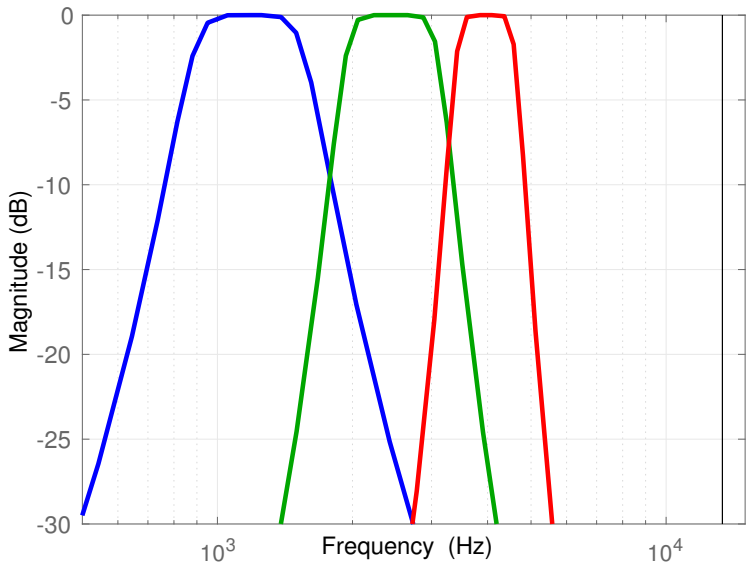


Figure 7.17: Band-pass filters

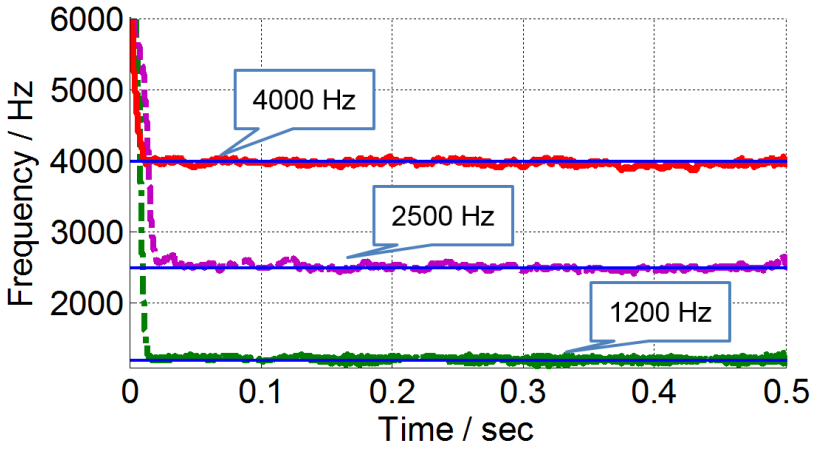


Figure 7.18: Frequency identification

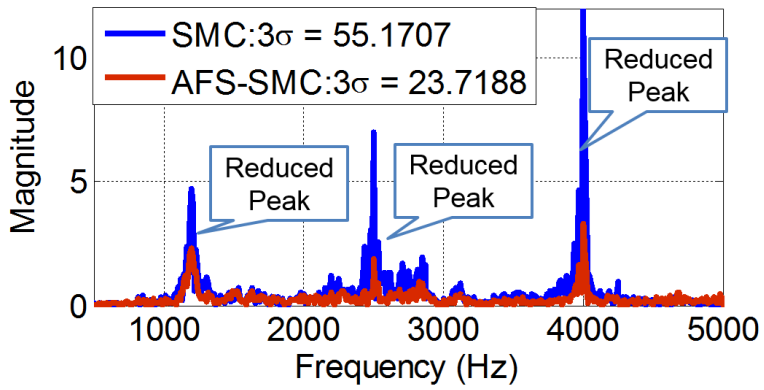


Figure 7.19: PES spectrum comparison

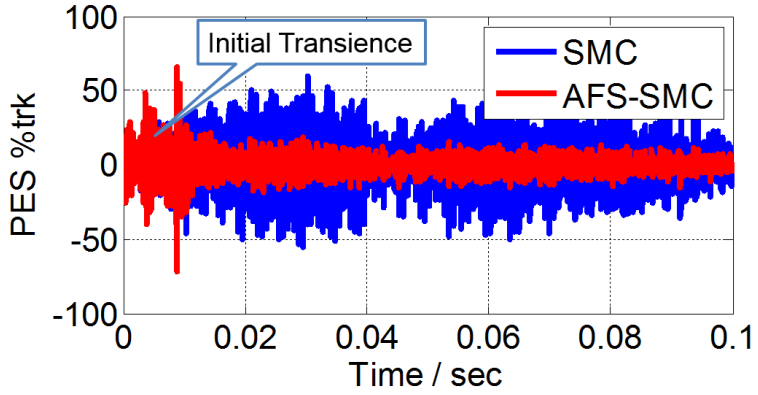


Figure 7.20: PES comparison in time domain

## 7.4 Chapter Summary

This chapter validates the effectiveness of the FSSMC algorithms when the states as well as the external disturbances are neither available nor directly measurable. The ESO is implemented to estimate both the states and the disturbances. The disturbance estimate is utilized to identify the peak frequencies of the disturbances; the state estimate is utilized to generate the control signal based on the control law. Multi-rate ESO allows the frequency shaping beyond the Nyquist frequency. The online identification for the peak frequencies allows adaptive frequency shaping when the vibration peak frequencies are not exactly known. Simulation study is performed on the HDD Benchmark system, and the effectiveness of the FSSMCs based on ESO, multi-rate ESO, and the adaptive frequency shaping techniques have been demonstrated.

# Chapter 8

# Conclusions and Future Work

## 8.1 Concluding Remarks

This dissertation has explored several learning, estimation, and control algorithms to achieve greater autonomy and accuracy in high-precision systems. The main contributions and conclusions are summarized as follows.

- A systematic framework for the design of arbitrary-order iterative learning control (ILC) has been proposed with guaranteed convergence and ease of tuning. The learning filters are obtained through minimizing the H-infinity norm of a constructed feedback system. In this framework, the period of each cycle in iterations is extended to infinity, and the systems are represented by infinite impulse response (IIR) filters for easy implementation and efficient computation. This approach has been further advanced to explicitly consider system variations. Both simulations and experiments validate these properties.

- A generalized design procedure for the disturbance observer (DOB) has been proposed for multi-input multi-output (MIMO) systems. The procedure releases the DOB design from the inverse of the plant, which is difficult to obtain especially for non-minimum phase systems and MIMO systems. The procedure is performed through solving an H-infinity optimization problem from the disturbance to its estimation error, which can be easily solved through robust control toolbox. This technique has been applied to a dual-stage hard disk drive (HDD) and the effectiveness of the proposed DOB has been demonstrated.

- Two techniques have been explored to increase the estimation bandwidth of the extended state observer (ESO): phase compensator and multi-rate ESO. The former one recovers the phase loss introduced by the system and provides better estimates for high-frequency disturbances within specific frequency range. The latter one utilizes the nominal dynamics of the disturbance, and shows the capability of capturing the hidden large off-track behaviors and the vibrations beyond the Nyquist frequency in HDDs.

- Two frequency-shaped sliding mode control (FSSMC) algorithms have been proposed for vibration suppression in high-precision systems. The first one is based on the root locus technique, which is easy to design and shows effectiveness especially for the vibration with

single large peak. The second one treats the sliding surface as a feedback system, and the shaping filter is designed using the H-infinity robust control theory. This systematic design framework guarantees the stability of the sliding surface, and shows great effectiveness and advantages when the vibrations have multiple large peaks. Furthermore, this dissertation has proposed a sub-optimal shaping filter which is explicitly dependent on the weighting filters and holds the potential for the adaptive frequency shaping with efficient computation.

A promising use of the methodological frameworks presented in this dissertation is the development of learning, estimation and control algorithms for advanced systems including manufacturing, information storage systems and autonomous robotics. These systems with self-learning abilities and high precision hold the potential to further increase the capacity of automation in the tremendous areas such as intelligent manufacturing.

## 8.2 Future Topics

### Iterative Learning Control

A systematic approach of designing an arbitrary-order ILC has been presented in this dissertation. Two follow-up directions will be explored in the future. (1) The proposed framework will be applied to a MIMO system and extended to a more generic formulation where an $N$th-order ILC uses the information from both the preceding iterations and the current iteration, which is an optimization procedure that involves both the feedforward and feedback controllers. (2) The proposed framework will be extended to more generic cases that including both the causal and non-causal learning filters, which is challenging and significant for the frequency-domain design of ILC that assumes infinite horizon for each iteration.

### Vibration Estimation

Vibration estimation without vibration sensors is a lastingly challenging topic in high-precision systems. To achieve better vibration estimation at higher frequencies, several techniques have been presented in this dissertation: DOB, ESO with phase compensation, and multi-rate ESO for the estimation beyond the Nyquist frequency. These techniques are based on certain assumptions, such as an accurate plant model and rich disturbance information. The future directions will explore the possibilities of maintaining the performance of the proposed estimation techniques with less strict assumptions: (1) the generalized DOB design procedure that explicitly considers system variations as well as the saturations (nonlinear constraints) in the PZT loop in dual-stage HDDs; (2) the phase compensation that can be implemented online without the prior information of vibration's peak frequencies; and (3) multi-rate estimation algorithm that utilizes less information of the vibrations beyond the Nyquist frequency.

### Nonlinear Vibration Suppression

Nonlinear control techniques for vibration suppression have several advantages compared to linear control techniques. Take HDD as an example; there are two main challenges of linear control in

HDDs: (1) the switch of different control algorithms between the track seeking and the track following; and (2) the 'waterbed' effect in linear time invariant (LTI) systems that limits the servo performance. Nonlinear control provides some possibilities to address these challenges. However, most of the nonlinear control techniques lack a systematic framework to quantitatively guarantee the closed-loop performance in frequency domain, which is essential for high-precision systems. This dissertation took a step towards this knowledge gap and proposed an H-infinity synthesis for the FSSMC. Tow future directions will be explored for the completeness of the design framework: (1) extension to MIMO systems which involves more complex mathematic considerations and derivations; and (2) achieving theoretical limitation in SMC systems which is similar to the Bode's Integral Theorem in LTI systems.

# Bibliography


[1] IEEJ. "IEEJ Technical Commitee for Novel Nanoscale Servo Control, NSS benchmark problem of hard disk drive systems". In: *http://mizugaki.iis.u-tokyo.ac.jp/nss/* (2007).

[2] Minghui Zheng, Shiying Zhou, and Masayoshi Tomizuka. "Identification of Resonance Frequencies in Dual-stage Hard Disk Drives: A Practical Strategy". In: *ASME 2017 Dynamic Systems and Control Conference*. American Society of Mechanical Engineers. 2017, (submitted).

[3] Xu Chen and Masayoshi Tomizuka. "Optimal Decoupled Disturbance Observers for Dual-Input Single-Output Systems". In: *Journal of Dynamic Systems, Measurement, and Control* 136.5 (2014), p. 051018.

[4] Minghui Zheng, Shiying Zhou, and Masayoshi Tomizuka. "'A Design Methodology for Disturbance Observer with Application to Precision Motion Control: An H-infinity based Approach". In: *Proceedings of the American Control Conference (ACC)*. Seattle, USA, 2017.

[5] Minghui Zheng et al. *Data storage device comprising slew rate anti-windup compensation for microactuator*. US Patent 9,007,714. 2015.

[6] S. Zhou and M. Tomizuka. "Enhanced anti-windup compensation for the dual stage hard disk drive systems with amplitude saturation". In: *2016 IEEE International Conference on Advanced Intelligent Mechatronics (AIM)*. 2016, pp. 822–827. DOI: 10.1109/AIM.2016.7576870.

[7] Shiying Zhou, Minghui Zheng, and Masayoshi Tomizuka. "A Generalized Anti-Windup Scheme Considering Amplitude and Rate Saturations". In: *ASME 2016 Dynamic Systems and Control Conference*. American Society of Mechanical Engineers. 2016, V002T22A007–V002T22A007.

[8] Hoday Margaret Stearns. *Iterative Methods for High Precision Motion Control with Application to a Wafer Scanner System*. Ph.D. dissertation, Mechanical Engineering, University of California, Berkeley, 2011.

[9] Yi Min Zhao et al. "Calibration-Based Iterative Learning Control for Path Tracking of Industrial Robots". In: *Industrial Electronics, IEEE Transactions on* 62.5 (May 2015), pp. 2921–2929. ISSN: 0278-0046. DOI: 10.1109/TIE.2014.2364800.

[10] C. Wang et al. "Robust two-degree-of-freedom iterative learning control for flexibility compensation of industrial robot manipulators". In: *2016 IEEE International Conference on Robotics and Automation (ICRA)*. 2016, pp. 2381–2386. DOI: 10.1109/ICRA.2016.7487388.

[11] Wenjie Chen and M. Tomizuka. "Dual-Stage Iterative Learning Control for MIMO Mismatched System With Application to Robots With Joint Elasticity". In: *Control Systems Technology, IEEE Transactions on* 22.4 (July 2014), pp. 1350–1361. ISSN: 1063-6536. DOI: 10.1109/TCST.2013.2279652.

[12] A. Visioli, G. Ziliani, and G. Legnani. "Iterative-Learning Hybrid Force/Velocity Control for Contour Tracking". In: *Robotics, IEEE Transactions on* 26.2 (Apr. 2010), pp. 388–393. ISSN: 1552-3098. DOI: 10.1109/TRO.2010.2041265.

[13] Jian-Xin Xu et al. "Extreme Precise Motion Tracking of Piezoelectric Positioning Stage Using Sampled-Data Iterative Learning Control". In: *Control Systems Technology, IEEE Transactions on* 21.4 (July 2013), pp. 1432–1439. ISSN: 1063-6536. DOI: 10.1109/TCST.2012.2201718.

[14] D. Huang et al. "High-Performance Tracking of Piezoelectric Positioning Stage Using Current-Cycle Iterative Learning Control With Gain Scheduling". In: *IEEE Transactions on Industrial Electronics* 61.2 (2014), pp. 1085–1098. ISSN: 0278-0046.

[15] M.R. Graham and R.A. de Callafon. "An iterative learning design for repeatable runout cancellation in disk drives". In: *Control Systems Technology, IEEE Transactions on* 14.3 (June 2006), pp. 474–482. ISSN: 1063-6536. DOI: 10.1109/TCST.2006.872531.

[16] Y. Chen et al. "Iterative Learning Control and Repetitive Control in Hard Disk Drive Industry - A Tutorial". In: *Proceedings of the 45th IEEE Conference on Decision and Control (CDC)*. San Diego, CA, 2006, pp. 2338–2351.

[17] S. Mishra and M. Tomizuka. "Projection-Based Iterative Learning Control for Wafer Scanner Systems". In: *Mechatronics, IEEE/ASME Transactions on* 14.3 (June 2009), pp. 388–393. ISSN: 1083-4435. DOI: 10.1109/TMECH.2008.2007302.

[18] Chung-Yen Lin, Liting Sun, and M. Tomizuka. "Robust principal component analysis for iterative learning control of precision motion systems with non-repetitive disturbances". In: *Proceedings of the American Control Conference (ACC)*. Chicago, IL, USA, 2015, pp. 2819–2824. DOI: 10.1109/ACC.2015.7171162.

[19] Sanjib K. Panda Jian-Xin Xu and Tong Heng Lee. *Real-time Iterative Learning Control: Design and Applications*. Springer, 2009.

[20] Shang-Chen Wu and Masayoshi Tomizuka. "Repeatable runout compensation for hard disk drives using adaptive feedforward cancellation". In: *American Control Conference, 2006*. IEEE. 2006, pp. 382–387.

[21] Shiying Zhou and Masayoshi Tomizuka. "Vibration Suppression Based on Adaptive Feedforward Control With Infinite Impulse Response Filter". In: *ASME 2015 Dynamic Systems and Control Conference*. American Society of Mechanical Engineers. 2015, V003T52A001–V003T52A001.

[22] Behrooz Shahsavari et al. "Adaptive repetitive control using a modified filtered-X LMS algorithm". In: *ASME 2014 Dynamic Systems and Control Conference*. American Society of Mechanical Engineers. 2014, V001T13A006–V001T13A006.

[23] Qing Wei Jia. "Disturbance rejection through disturbance observer with adaptive frequency estimation". In: *Magnetics, IEEE Transactions on* 45.6 (2009), pp. 2675–2678.

[24] Xu Chen and Masayoshi Tomizuka. "Unknown Multiple Narrow-Band Disturbance Rejection in Hard Disk Drives: An Adaptive Notch Filter and Perfect Disturbance Observer Approach". In: *ASME 2010 Dynamic Systems and Control Conference*. American Society of Mechanical Engineers. 2010, pp. 963–970.

[25] Jinchuan Zheng, Guoxiao Guo, and Youyi Wang. "Nonlinear PID control of linear plants for improved disturbance rejection". In: *16th IFAC world congress (IFAC 2005)*. 2005.

[26] Xu Chen and Masayoshi Tomizuka. "Control methodologies for precision positioning systems". In: *American Control Conference (ACC), 2013*. IEEE. 2013, pp. 3704–3711.

[27] Jianbin Nie and Roberto Horowitz. "Control design of concentric self-servo track writing systems for hard disk drives". In: *American Control Conference (ACC), 2010*. IEEE. 2010, pp. 2631–2640.

[28] Xu Chen and Masayoshi Tomizuka. "Overview and new results in disturbance observer based adaptive vibration rejection with application to advanced manufacturing". In: vol. 29. 11. Wiley Online Library, 2015, pp. 1459–1474.

[29] Li Yi and M. Tomizuka. "Two-degree-of-freedom control with robust feedback control for hard disk servo systems". In: *IEEE/ASME Transactions on Mechatronics* 4.1 (1999), pp. 17–24. ISSN: 1083-4435. DOI: 10.1109/3516.752080.

[30] Q. W. Jia. "Disturbance Rejection Through Disturbance Observer With Adaptive Frequency Estimation". In: *IEEE Transactions on Magnetics* 45.6 (2009), pp. 2675–2678. ISSN: 0018-9464. DOI: 10.1109/TMAG.2009.2018605.

[31] X. Fan and M. Tomizuka. "Robust disturbance observer design for a power-assist electric bicycle". In: *Proceedings of the 2010 American Control Conference*. 2010, pp. 1166–1171. DOI: 10.1109/ACC.2010.5530998.

[32] S. Yu and M. Tomizuka. "Performance enhancement of iterative learning control system using disturbance observer". In: *2009 IEEE/ASME International Conference on Advanced Intelligent Mechatronics*. 2009, pp. 987–992. DOI: 10.1109/AIM.2009.5229715.

[33] Jong Nam Yun and Jian-Bo Su. "Design of a disturbance observer for a two-link manipulator with flexible joints". In: *IEEE Transactions on Control Systems Technology* 22.2 (2014), pp. 809–815.

[34] Christian Rathgeber et al. "Disturbance Observer for Lateral Trajectory Tracking Control for Autonomous and Cooperative Driving". In: *World Academy of Science, Engineering and Technology, International Journal of Mechanical, Aerospace, Industrial, Mechatronic and Manufacturing Engineering* 9.6 (2015), pp. 905–912.

[35] Jingqing Han. "From PID to Active Disturbance Rejection Control". In: *Industrial Electronics, IEEE Transactions on* 56.3 (2009), pp. 900–906. ISSN: 0278-0046. DOI: 10.1109/TIE.2008.2011621.

[36] R. Miklosovic, A. Radke, and Z. Gao. "Discrete implementation and generalization of the extended state observer". In: *Procedings of the American Control Conference*. June 2006, pp. 2209–2214. DOI: 10.1109/ACC.2006.1656547.

[37] Weiwen Wang and Zhiqiang Gao. "A comparison study of advanced state observer design techniques". In: *American Control Conference, 2003. Proceedings of the 2003*. Vol. 6. June 2003, 4754–4759 vol.6. DOI: 10.1109/ACC.2003.1242474.

[38] A. Radke and Zhiqiang Gao. "A survey of state and disturbance observers for practitioners". In: *Procedings of the American Control Conference*. June 2006, pp. 5183–5188. DOI: 10.1109/ACC.2006.1657545.

[39] Xiaoxia Yang and Yi Huang. "Capabilities of extended state observer for estimating uncertainties". In: *Procedings of the American Control Conference*. June 2009, pp. 3700–3705. DOI: 10.1109/ACC.2009.5160642.

[40] Qing Zheng, L.Q. Gao, and Zhiqiang Gao. "On Validation of Extended State Observer Through Analysis and Experimentation". In: *Journal of Dynamic Systems, Measurement, and Control* 134 (2012), pp. 024505,1–5.

[41] Qing Zheng and Zhiqiang Gao. "On practical applications of active disturbance rejection control". In: *2010 29th Chinese Control Conference (CCC)*. July 2010, pp. 6095–6100.

[42] Jinwen Pan and Yong Wang. "Stabilization and Tracking Control Of X-Z Inverted Pendulum Using Flatness Based Active Disturbance Rejection Control". In: *Asian Journal of Control* (2015).

[43] Jinwen Pan, Shimin Qi, and Yong Wang. "Flatness based active disturbance rejection control for cart inverted pendulum and experimental study". In: *American Control Conference (ACC), 2015*. IEEE. 2015, pp. 4868–4873.

[44] T. Atsumi, A. Okuyama, and M. Kobayashi. "Track-Following Control Using Resonant Filter in Hard Disk Drives". In: *Mechatronics, IEEE/ASME Transactions on* 12.4 (2007), pp. 472–479. ISSN: 1083-4435.

[45] Siri Weerasooriya and D.T. Phan. "Discrete-time LQG/LTR design and modeling of a disk drive actuator tracking servo system". In: *Industrial Electronics, IEEE Transactions on* 42.3 (1995), pp. 240–247. ISSN: 0278-0046.

[46] Xiaoping Hu et al. "Discrete-time LQG/LTR dual-stage controller design and implementation for high track density HDDs". In: *Proceedings of American Control Conference (ACC)*. Vol. 6. San Diego, USA, 1999, pp. 4111–4115.

[47] Xinghui Huang and R. Horowitz. "Robust Controller Design of a Dual-Stage Disk Drive Servo System With an Instrumented Suspension". In: *Magnetics, IEEE Transactions on* 41.8 (2005), pp. 2406–2413. ISSN: 0018-9464.

[48] Moon-Noh Lee et al. "Robust H-infintity control with multiple constraints for the track-following system of an optical disk drive". In: *Industrial Electronics, IEEE Transactions on* 45.4 (1998), pp. 638–645. ISSN: 0278-0046.

[49] G. Stein. "Respect the unstable". In: *IEEE Control Systems* 23.4 (2003), pp. 12–25. ISSN: 1066-033X.

[50] Minghui Zheng, Xu Chen, and Masayoshi Tomizuka. "A Nonlinear Feedback Control Scheme for Transient Performance Enhancement in Hard Disk Drives". In: *ASME 2014 Conference on Information Storage and Processing Systems*. American Society of Mechanical Engineers. 2014, V001T03A003–V001T03A003.

[51] Seung-Hi Lee, Sang-Eun Baek, and Young-Hoon Kim. "Design of a dual-stage actuator control system with discrete-time sliding mode for hard disk drives". In: *Proceedings of the 39th IEEE Conference on Decision and Control (CDC)*. Vol. 4. Sydney, Australia, 2000, pp. 3120–3125.

[52] D. Q. Zhang and G.X. Guo. "Discrete-time sliding mode proximate time optimal seek control of hard disk drives". In: *Control Theory and Applications, IEE Proceedings* 147.4 (2000), pp. 440–446. ISSN: 1350-2379.

[53] J. Zhou et al. "Improved proximate time-optimal sliding-mode control of hard disk drives". In: *Control Theory and Applications, IEEE Proceedings* 148.6 (2001), pp. 516–522. ISSN: 1350-2379.

[54] Qinglei Hu et al. "Discrete-Time Sliding Mode Control With Time-Varying Surface for Hard Disk Drives". In: *Control Systems Technology, IEEE Transactions on* 17.1 (2009), pp. 175–183. ISSN: 1063-6536.

[55] J. Ghosh and B. Paden. "Pseudo-inverse based iterative learning control for plants with unmodelled dynamics". In: *Proceedings of the American Control Conference (ACC)*. Vol. 1. 6. Chicago, Illinois, 2000, pp. 472–476. DOI: 10.1109/ACC.2000.878945.

[56] D. de Roover. "Synthesis of a robust iterative learning controller using an $H_\infty$ approach". In: *Proceedings of the 35th IEEE Conference on Decision and Control (CDC)*. Kobe, Japan, 1996, pp. 3044–3049.

[57] B. E. Helfrich et al. "Combined $H_\infty$-Feedback Control and Iterative Learning Control Design With Application to Nanopositioning Systems". In: *IEEE Transactions on Control Systems Technology* 18.2 (2010), pp. 336–351. ISSN: 1063-6536.

[58] Tae-Yong Doh Jung-Ho Moon and Myung Jin Chung. "A Robust Approach to Iterative Learning Control Design for Uncertain Systems". In: *Automatica* 34.8 (1998), 1001–1004.

[59] Dick De Roover and Okko H. Bosgra. "Synthesis of robust multivariable iterative learning controllers with application to a wafer stage motion system". In: *International Journal of Control* 73.10 (2000), pp. 968–979. DOI: 10.1080/002071700405923.

[60] Son Tong Duy, Goele Pipeleers, and Jan Swevers. "Robust Monotonic Convergent Iterative Learning Control". In: *IEEE Transactions on Automatic Control* 61.4 ().

[61] Tong Duy Son, Goele Pipeleers, and Jan Swevers. "Robust Monotonic Convergent Iterative Learning Control". In: *IEEE Transactions on Automatic Control* 61.4 (2016), pp. 1063–1068.

[62] D.A. Bristow, M. Tharayil, and A.G. Alleyne. "A survey of iterative learning control". In: *Control Systems, IEEE* 26.3 (June 2006), pp. 96–114. ISSN: 1066-033X. DOI: 10.1109/MCS.2006.1636313.

[63] Hyo-Sung Ahn, Yang Quan Chen, and K.L. Moore. "Iterative Learning Control: Brief Survey and Categorization". In: *Systems, Man, and Cybernetics, Part C: Applications and Reviews, IEEE Transactions on* 37.6 (2007), pp. 1099–1121. ISSN: 1094-6977. DOI: 10.1109/TSMCC.2007.905759.

[64] David H Owens and Jari Hätönen. "Iterative learning controlAn optimization paradigm". In: *Annual reviews in control* 29.1 (2005), pp. 57–70.

[65] David H. Owens. *Iterative learning controlAn optimization paradigm*. Springer, 2015.

[66] M. Norrlof. "Comparative study on first and second order ILC-frequency domain analysis and experiments". In: *Proceedings of the 39th IEEE Conference on Decision and Control (CDC)*. Sydney, NSW, 2000, pp. 3415–3420.

[67] Mikael Norrlf and Svante Gunnarsson. "Time and frequency domain convergence properties in iterative learning control". In: *International Journal of Control* 75.14 (2002), pp. 1114–1126. DOI: 10.1080/00207170210159122.

[68] K.L. Moore and YangQuan Chen. "A separative high-order framework for monotonic convergent iterative learning controller design". In: *Proceedings of the American Control Conference (ACC)*. Vol. 4. 2003, 3644–3649 vol.4.

[69] Chenkun Yin, Jian-Xin Xu, and Zhongsheng Hou. "A High-Order Internal Model Based Iterative Learning Control Scheme for Nonlinear Systems With Time-Iteration-Varying Parameters". In: *Automatic Control, IEEE Transactions on* 55.11 (2010), pp. 2665–2670. ISSN: 0018-9286. DOI: 10.1109/TAC.2010.2069372.

[70] X. Ruan, Z.Z. Bien, and Q. Wang. "Convergence characteristics of proportional-type iterative learning control in the sense of Lebesgue-p norm". In: *Control Theory Applications, IET* 6.5 (2012), pp. 707–714. ISSN: 1751-8644. DOI: 10.1049/iet-cta.2010.0388.

[71] K.L. Moore, Yang Quan Chen, and Hyo-Sung Ahn. "Algebraic $H_\infty$ Design of Higher-Order Iterative Learning Controllers". In: *Proceedings of the 2005 IEEE International Symposium on intelligent control*. Limassol, Cyprus.

[72] Kevin L Moore, Hyo-Sung Ahn, and Yang Quan Chen. "Iteration domain H∞-optimal iterative learning controller design". In: *International Journal of Robust and Nonlinear Control* 18.10 (2008), pp. 1001–1017.

[73] Minghui Zheng et al. "Arbitrary-Order Iterative Learning Control Considering H Synthesis". In: *The ASME 2016 Dynamic Systems and Control Conference (DSCC)*. Minneapolis, Minnesota, 2016.

[74] Pascal Gahinet and Pierre Apkarian. "A linear matrix inequality approach to H-infinity control". In: *International journal of robust and nonlinear control* 4.4 (1994), pp. 421–448.

[75] John Doyle. "Synthesis of robust controllers and filters". In: *Proceedings of the 22nd IEEE Conference on Decision and Control (CDC)*. 22. San Antonio, TX, USA, pp. 109–114.

[76] Gary J Balas et al. "$\mu$-analysis and synthesis toolbox". In: *MUSYN Inc. and The MathWorks, Natick MA* (1993).

[77] Sigurd Skogestad and Ian Postlethwaite. *Multivariable feedback control: analysis and design*. 2nd ed. Wiley New York, 2007.

[78] Z. Bien and K. M. Huh. "Higher-order iterative learning control algorithm". In: *IEE Proceedings D - Control Theory and Applications* 136.3 (1989), pp. 105–112. ISSN: 0143-7054. DOI: 10.1049/ip-d.1989.0016.

[79] Chun-Chih Wang and Masayoshi Tomizuka. "Design of robustly stable disturbance observers based on closed loop consideration using H-infinity optimization and its applications to motion control systems". In: *American Control Conference, 2004. Proceedings of the 2004*. Vol. 4. IEEE. 2004, pp. 3764–3769.

[80] CK Thum et al. "H $\alpha$ disturbance observer design for high precision track following in hard disk drives". In: *IET control theory & applications* 3.12 (2009), pp. 1591–1598.

[81] J Su, L Wang, and JN Yun. "A design of disturbance observer in standard H control framework". In: *International Journal of Robust and Nonlinear Control* 25.16 (2015), pp. 2894–2910.

[82] C. Du et al. "Simple disturbance observer for disturbance compensation". In: *IET Control Theory Applications* 4.9 (2010), pp. 1748–1755. ISSN: 1751-8644. DOI: 10.1049/iet-cta.2009.0178.

[83] Jianbin Nie and Roberto Horowitz. "Design and implementation of dual-stage track-following control for hard disk drives". In: *ASME 2009 Dynamic Systems and Control Conference*. American Society of Mechanical Engineers. 2009, pp. 565–572.

[84] Kouhei Ohnishi. "Robust motion control by disturbance observer". In: *Journal of the Robotics Society of Japan* 11.4 (1993), pp. 486–493.

[85] K Mori et al. "A dual-stage magnetic disk drive actuator using a piezoelectric device for a high track density". In: *Magnetics, IEEE Transactions on* 27.6 (1991), pp. 5298–5300.

[86] Shang-Chen Wu. *Precision control for high-density and cost-effective hard disk drives*. ProQuest, 2008.

[87] Abdullah Al Mamun, GuoXiao Guo, and Chao Bi. *Hard disk drive: mechatronics and control*. Vol. 23. CRC press, 2006.

[88] W. Gao, Yufu Wang, and A. Homaifa. "Discrete-time variable structure control systems". In: *Industrial Electronics, IEEE Transactions on* 42.2 (1995), pp. 117–122. ISSN: 0278-0046.

[89] Minghui Zheng, Xu Chen, and Masayoshi Tomizuka. "Extended State Observer with Phase Compensation to Estimate and Suppress High-frequency Disturbances". In: *Proceedings of the American Control Conference (ACC)*. Boston, USA, 2016.

[90] Dan Simon. "Chapter 5 The discrete-time Kalman filter, Optimal State Estimation: Kalman, H Infinity, and Nonlinear Approaches". In: *John Wiley & Sons, Inc.* (2006).

[91] M. L. J. Hautus. "Controllability and observability condition of linear autonomous systems". In: *Ned. Akad. Wetenschappen, Proc. Ser. A,* 72 (1969), pp. 445–455.

[92] H.K. Khalil. "High-gain observers in nonlinear feedback control". In: *Control, Automation and Systems, 2008. ICCAS 2008. International Conference on*. 2008.

[93] H.K. Khalil and L. Praly. "High-gain observers in nonlinear feedback control". In: *Int. J. Robust Nonlinear Control*. Vol. 24. 2014, 9931015.

[94] Philip A Weaver and Richard M Ehrlich. "The use of multirate notch filters in embedded-servo disk drives". In: *American Control Conference, Proceedings of the 1995*. Vol. 6. IEEE. 1995, pp. 4156–4160.

[95] T. Atsumi, A. Okuyama, and M. Kobayashi. "Vibration suppression beyond Nyquist frequency in hard disk drives". In: *2006 IEEE International Symposium on Intelligent Control*. 2006, pp. 1109–1114. DOI: 10.1109/CACSD-CCA-ISIC.2006.4776799.

[96] T. Atsumi, A. Okuyama, and S. Nakagawa. "Vibration Control Above the Nyquist Frequency in Hard Disk Drives". In: *Industrial Electronics, IEEE Transactions on* 55.10 (2008), pp. 3751–3757. ISSN: 0278-0046. DOI: 10.1109/TIE.2008.928153.

[97] T. Atsumi. "Disturbance suppression beyond Nyquist frequency in hard disk drives". In: *Mechatronics* 20.1 (2010), pp. 67–73.

[98] Y. Yamamoto, K. Yamamoto, and M. Nagahara. "Tracking of signals beyond the Nyquist frequency". In: *2016 IEEE 55th Conference on Decision and Control (CDC)*. 2016, pp. 4003–4008. DOI: 10.1109/CDC.2016.7798875.

[99] T. Atsumi and W.C. Messner. "Analysis of Unobservable Oscillations in Sampled-Data Positioning Systems". In: *Industrial Electronics, IEEE Transactions on* 59.10 (2012), pp. 3951–3960. ISSN: 0278-0046. DOI: 10.1109/TIE.2011.2159355.

[100] Takenori Atsumi. "Minimization of unobservable oscillation in repeatable run-out for magnetic-head positioning system of hard disk drives". In: *Mechatronics* 44 (2017), pp. 24–31.

[101] Minghui Zheng, Liting Sun, and Masayoshi Tomizuka. "Multi-rate Observer Based Sliding Mode Control with Frequency Shaping for Vibration Suppression Beyond Nyquist Frequency". In: *IFAC-PapersOnLine* 49.21 (2016), pp. 13–18.

[102] Andrew Smyth and Meiliang Wu. "Multi-rate Kalman filtering for the data fusion of displacement and acceleration response measurements in dynamic system monitoring". In: *Mechanical Systems and Signal Processing* 21.2 (2007), pp. 706–723.

[103] J. Yang, S. Li, and X. Yu. "Sliding-Mode Control for Systems With Mismatched Uncertainties via a Disturbance Observer". In: *IEEE Transactions on Industrial Electronics* 60.1 (2013), pp. 160–169. ISSN: 0278-0046.

[104] S. Y. Chen and F. J. Lin. "Robust Nonsingular Terminal Sliding-Mode Control for Nonlinear Magnetic Bearing System". In: *IEEE Transactions on Control Systems Technology* 19.3 (2011), pp. 636–643. ISSN: 1063-6536.

[105] F. Chen et al. "Robust Backstepping Sliding-Mode Control and Observer-Based Fault Estimation for a Quadrotor UAV". In: *IEEE Transactions on Industrial Electronics* 63.8 (2016), pp. 5044–5056. ISSN: 0278-0046.

[106] H. Li et al. "Adaptive Sliding-Mode Control for Nonlinear Active Suspension Vehicle Systems Using T-S Fuzzy Approach". In: *IEEE Transactions on Industrial Electronics* 60.8 (2013), pp. 3328–3338. ISSN: 0278-0046.

[107] L. Wang, T. Chai, and L. Zhai. "Neural-Network-Based Terminal Sliding-Mode Control of Robotic Manipulators Including Actuator Dynamics". In: *IEEE Transactions on Industrial Electronics* 56.9 (2009), pp. 3296–3304. ISSN: 0278-0046.

[108] Minghui Zheng et al. "Control of a spherical robot: Path following based on nonholonomic kinematics and dynamics". In: *Chinese Journal of Aeronautics* 24.3 (2011), pp. 337–345.

[109] A. Sabanovic. "Variable Structure Systems With Sliding Modes in Motion Control - A Survey". In: *IEEE Transactions on Industrial Informatics* 7.2 (2011), pp. 212–223. ISSN: 1551-3203.

[110] X. Yu, B. Wang, and X. Li. "Computer-Controlled Variable Structure Systems: The State-of-the-Art". In: *IEEE Transactions on Industrial Informatics* 8.2 (2012), pp. 197–205. ISSN: 1551-3203.

[111] X. Yu and O. Kaynak. "Sliding-Mode Control With Soft Computing: A Survey". In: *IEEE Transactions on Industrial Electronics* 56.9 (2009), pp. 3275–3285. ISSN: 0278-0046.

[112] K. David Young and Umiy Ozguner. "Frequency shaping compensator design for sliding mode". In: *International Journal of Control* 57.5 (1993), pp. 1005–1019.

[113] K. Nonami et al. "Frequency-shaped sliding mode control using $H_\infty$ control and $\mu$ synthesis theory". In: *Proceedings of IEEE International Workshop on Variable Structure Systems (VSS'96)*. Tokyo, Japan, 1996, pp. 175–180.

[114] J.T. Moura, R.G. Roy, and N. Olgac. "Frequency-shaped sliding modes: analysis and experiments". In: *Control Systems Technology, IEEE Transactions on* 5.4 (1997), pp. 394–401. ISSN: 1063-6536.

[115] H Yanada and H Ohnishi. "Frequency-shaped sliding mode control of an electrohydraulic servo-motor". In: *Proceedings of the Institution of Mechanical Engineers, Part I: Journal of Systems and Control Engineering* (1999), pp. 441–448.

[116] A.J. Koshkouei and A. S I Zinober. "Robust frequency shaping sliding mode control". In: *Control Theory and Applications, IEE Proceedings* 147.3 (2000), pp. 312–320. ISSN: 1350-2379.

[117] W. C. Wu and T.S. Liu. "Frequency-shaped sliding mode control for flying height of pickup head in near-field optical disk drives". In: *Magnetics, IEEE Transactions on* 41.2 (2005), pp. 1061–1063. ISSN: 0018-9464.

[118] A.J. Mehta and B. Bandyopadhyay. "Frequency-Shaped Sliding Mode Control Using Output Sampled Measurements". In: *Industrial Electronics, IEEE Transactions on* 56.1 (2009), pp. 28–35. ISSN: 0278-0046.

[119] Minghui Zheng et al. *Data storage devices and methods with frequency-shaped sliding mode control*. US Patent 9,542,966. 2017.

[120] R. Pupadubsin et al. "Adaptive Integral Sliding-Mode Position Control of a Coupled-Phase Linear Variable Reluctance Motor for High-Precision Applications". In: *IEEE Transactions on Industry Applications* 48.4 (2012), pp. 1353–1363. ISSN: 0093-9994.

[121] K. Abidi and A. Sabanovic. "Sliding-Mode Control for High-Precision Motion of a Piezostage". In: *IEEE Transactions on Industrial Electronics* 54.1 (2007), pp. 629–637. ISSN: 0278-0046.

[122] Minghui Zheng and Masayoshi Tomizuka. "Discrete-Time H-Infinity Synthesis of Frequency-Shaped Sliding Mode Control for Suppression of Vibration With Multiple Peak Frequencies". In: *ASME 2016 Dynamic Systems and Control Conference*. American Society of Mechanical Engineers. 2016, V002T22A006–V002T22A006.

[123] Yuske Konno and Hideki Hashimoto. "Design of sliding mode dynamics in the frequency domain". In: *Advanced Robotics* 7.6 (1992 (on-line available: 2012)), pp. 587–598.

[124] MLJ Hautus. "Stabilization controllability and observability of linear autonomous systems". In: *Indagationes mathematicae (proceedings)*. Vol. 73. Elsevier. 1970, pp. 448–455.

[125] Khalid Abidi and Jian-Xin Xu. *Chapter 2: Discrete-Time Sliding Mode Control, Advanced Discrete-Time Control*. Springer, 2015.

[126] M. Yan and Y. Shi. "Robust discrete-time sliding mode control for uncertain systems with time-varying state delay". In: *Control Theory Applications, IET* 2.8 (2008), pp. 662–674. ISSN: 1751-8644.

[127] Minghui Zheng, Xu Chen, and Masayoshi Tomizuka. "Discrete-time Frequency-shaped Sliding Mode Control for Audio-vibration Rejection in Hard Disk Drives". In: *Proceedings of the 19th World Congress of the International Federation of Automatic Control (IFAC)*. Vol. 47. 3. Cape Town, South Africa, 2014, pp. 6843–6848.

[128] S. Sarpturk, Y. Istefanopulos, and O. Kaynak. "On the stability of discrete-time sliding mode control systems". In: *Automatic Control, IEEE Transactions on* 32.10 (1987), pp. 930–932. ISSN: 0018-9286.

[129] Goran Golo and Čedomir Milosavljević. "Robust discrete-time chattering free sliding mode control". In: *Systems & Control Letters* 41.1 (2000), pp. 19–28.

[130] Pierre Apkarian, Pascal Gahinet, and Greg Becker. "Self-scheduled H control of linear parameter-varying systems: a design example". In: *Automatica* 31.9 (1995), pp. 1251–1261.

[131] Pierre Apkarian and Richard J Adams. "Advanced gain-scheduling techniques for uncertain systems". In: *Control Systems Technology, IEEE Transactions on* 6.1 (1998), pp. 21–32.

[132] Xu Chen and Masayoshi Tomizuka. "Overview and New Results in Disturbance Observer based Adaptive Vibration Rejection With Application to Advanced Manufacturing". In: *International Journal of Adaptive Control and Signal Processing* 29 (2015), pp. 1459–1474.

[133] Jinchuan Zheng et al. "Optimal narrow-band disturbance filter for PZT-actuated head positioning control on a spinstand". In: *Magnetics, IEEE Transactions on* 42.11 (2006), pp. 3745–3751.

[134] Qixing Zheng and M. Tomizuka. "A disturbance observer approach to detecting and rejecting narrow-band disturbances in hard disk drives". In: *Advanced Motion Control, 2008. AMC '08. 10th IEEE International Workshop on*. 2008, pp. 254–259. DOI: 10.1109/AMC.2008.4516075.

[135] Xu Chen and Masayoshi Tomizuka. "A minimum parameter adaptive approach for rejecting multiple narrow-band disturbances with application to hard disk drives". In: *Control Systems Technology, IEEE Transactions on* 20.2 (2012), pp. 408–415.

[136] Qingwei Jia and ZhongFeng Wang. "A New Adaptive Method for Identification of Multiple Unknown Disturbance Frequencies in HDDs". In: *Magnetics, IEEE Transactions on* 44.11 (2008), pp. 3746–3749. ISSN: 0018-9464. DOI: 10.1109/TMAG.2008.2002624.

[137] Minghui Zheng and Masayoshi Tomizuka. "Adaptive Frequency-shaped Sliding Mode Control for Narrow-band Disturbance Rejection". In: *Proceedings of the IEEE International Conference on Advanced Intelligent Mechatronics (AIM)*. Banff, Alberta, Canada, 2016.

[138] X. Liang and K. Mosalam. "Lyapunov stability and accuracy of direct integration algorithms applied to nonlinear dynamic problems". In: *Journal of Engineering Mechanics* 142.5 (2016), p. 04016022.

[139] X. Liang and K. Mosalam. "Lyapunov stability analysis of explicit direct integration algorithms considering strictly positive real lemma". In: *Journal of Engineering Mechanics* 142.10 (2016), p. 04016079.

[140] X. Liang and K. Mosalam. "Lyapunov stability analysis of explicit direct integration algorithms applied to multi-degree-of-freedom nonlinear dynamic problems". In: *Journal of Engineering Mechanics* 142.12 (2016), p. 04016098.

[141] Frank Permenter, Charles Wampler, and Russ Tedrake. "A numerical algebraic geometry approach to regional stability analysis of polynomial systems". In: *American Control Conference (ACC), Washington, DC, USA, 2013*. 2013, pp. 2127–2132.

[142] Xu Chen and Masayoshi Tomizuka. "A Minimum Parameter Adaptive Approach for Rejecting Multiple Narrow-Band Disturbances With Application to Hard Disk Drives". In: *Control Systems Technology, IEEE Transactions on* 20.2 (2012), pp. 408–415. ISSN: 1063-6536.